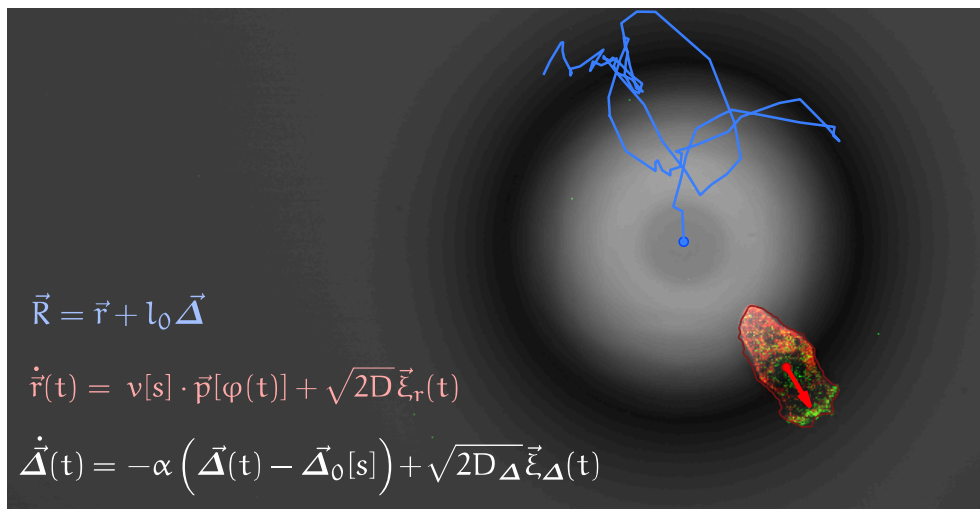


EXPERIMENTAL AND THEORETICAL STUDY ON AMOEBOID CELL-CARGO ACTIVE MOTION

VALENTINO LEPRO



A PHYSICAL ANALYSIS OF CELL-MEDIATED PARTICLE TRANSPORT

Doctoral Thesis
Ph.D. in Physics (Dr. rer. nat., Physik)
Department of Physics and Astronomy
Biological Physics Group
Potsdam Universität

*International Max Planck Research School (IMPRS)
on Multiscale Bio-Systems*

October 2016 - August 2020

This work is licensed under a Creative Commons License:
Attribution 4.0 International.
This does not apply to quoted content from other authors.
To view a copy of this license visit
<https://creativecommons.org/licenses/by/4.0/>

Valentino Lepro: *Experimental and Theoretical study on amoeboid cell-cargo active motion*,
A physical analysis of cell-mediated particle transport, Ph.D. in Physics (Dr. rer. nat.,
Physik), © October 2016 - August 2020

Supervisors:
Carsten Beta
Stefan Klumpp

Location:
Potsdam, Germany

Time frame:
October 2016 - August 2020

Published online on the
Publication Server of the University of Potsdam:
<https://doi.org/10.25932/publishup-49089>
<https://nbn-resolving.org/urn:nbn:de:kobv:517-opus4-490890>

*Happiness
only real when shared.*

— **Christopher J. McCandless (Alexander Supertramp), *travel journal* (summer
1992)**

I dedicate this work to those who, driven only by the most sincere love,
have supported and inspired me in ways they may not be aware of,
in a venture through seas they knew not either. . .
To you I owe much.

ABSTRACT

As society paves its way towards device miniaturization and precision medicine, micro-scale actuation and guided transport become increasingly prominent research fields, with high potential impact in both technological and clinical contexts. In order to accomplish directed motion of micron-sized objects, as biosensors and drug-releasing microparticles, towards specific target sites, a promising strategy is the use of living cells as smart biochemically-powered carriers, building the so-called bio-hybrid systems. Inspired by leukocytes, native cells of living organisms efficiently migrating to critical targets as tumor tissue, an emerging concept is to exploit the amoeboid crawling motility of such cells as mean of transport for drug delivery applications.

In the research work described in this thesis, I synergistically applied experimental, computational and theoretical modeling approaches to investigate the behaviour and transport mechanism of a novel kind of bio-hybrid system for active transport at the micro-scale, referred to as cellular truck. This system consists of an amoeboid crawling cell, the carrier, attached to a microparticle, the cargo, which may ideally be drug-loaded for specific therapeutic treatments.

For the purposes of experimental investigation, I employed the amoeba *Dictyostelium discoideum* as crawling cellular carrier, being a renowned model organism for leukocyte migration and, in general, for eukaryotic cell motility. The performed experiments revealed a complex recurrent cell-cargo relative motion, together with an intermittent motility of the cellular truck as a whole. The evidence suggests the presence of cargoes on amoeboid cells to act as mechanical stimulus leading cell polarization, thus promoting cell motility and giving rise to the observed intermittent dynamics of the truck. Particularly, bursts in cytoskeletal polarity along the cell-cargo axis have been found to occur in time with a rate dependent on cargo geometrical features, as particle diameter. Overall, the collected experimental evidence pointed out a pivotal role of cell-cargo interactions in the emergent cellular truck motion dynamics. Especially, they can determine the transport capabilities of amoeboid cells, as the cargo size significantly impacts the cytoskeletal activity and repolarization dynamics along the cell-cargo axis, the latter responsible for truck displacement and reorientation.

Furthermore, I developed a modeling framework, built upon the experimental evidence on cellular truck behaviour, that connects the relative dynamics and interactions arising at the truck scale with the actual particle transport dynamics. In fact, numerical simulations of the proposed model successfully reproduced the phenomenology of the cell-cargo system, while enabling the prediction of the transport properties of cellular trucks over larger spatial and temporal scales. The theoretical analysis provided a deeper understanding of the role of cell-cargo interaction on mass transport, unveiling in particular how the long-time transport efficiency is governed by the interplay between the persistence time of cell polarity and time scales of the relative dynamics stemming from cell-cargo interaction. Interestingly, the model predicts the existence of an optimal cargo size, enhancing the diffusivity of cellular trucks; this is in line with previous independent experimental data, which appeared rather counterintuitive and had no explanation prior to this study.

In conclusion, my research work shed light on the importance of cargo-carrier interactions in the context of crawling cell-mediated particle transport, and provides a prototypical, multifaceted framework for the analysis and modelling of such complex bio-hybrid systems and their perspective optimization.

ZUSAMMENFASSUNG

Im Zuge der fortschreitenden gesellschaftlichen Entwicklung hin zur Miniaturisierung und Präzisionsmedizin, gewinnen Fragen zu Antrieb und zielgerichtetem Transport auf der Mikrometerskala zunehmend an Bedeutung, nicht zuletzt wegen ihres kaum zu unterschätzendem Potentials für Medizin und Technik.

Eine vielversprechende Strategie, um den zielgerichteten Transport von Objekten auf der Mikrometerskala, wie zum Beispiel Biosensoren oder mit Medikamenten beladene Mikropartikel, zu bewerkstelligen, ist die Verwendung von lebenden Zellen als intelligenten, biochemisch angetriebenen Transportern. Zellen und Mikroobjekte bilden dabei gemeinsam sogenannte Bio-Hybridsysteme.

Inspiziert von Leukozyten - nativen Zellen lebender Organismen, welche sich effizient zu kritischen Zielen, wie Tumorgewebe, bewegen - besteht ein neues Konzept darin, die amöboide Fortbewegung solcher Zellen für den Medikamententransport zu nutzen.

Im Rahmen dieser Doktorarbeit kamen experimentelle, numerische und theoretische Modellierungsansätze zum Einsatz, um die Eigenschaften und Transportmechanismen eines neuen Bio-Hybridsystems für den aktiven Transport von Objekten auf der Mikrometerskala zu untersuchen. Dieses Bio-Hybridsystem wird im Folgenden als Zelltransporter bezeichnet. Ein Zelltransporter besteht aus einer sich amöboid fortbewegenden Zelle, dem Transporter, und einem Mikropartikel, der Fracht, welche idealerweise mit Medikamenten für therapeutische Zwecke beladen sein kann.

Für die experimentellen Untersuchungen wurde die Amöbe *Dictyostelium discoideum* als Transporter verwendet. Sie ist ein bekannter Modellorganismus für die Leukozytenmigration und für die Motilität eukaryotischer Zellen im Allgemeinen. Die durchgeführten Experimente zeigten eine komplexe, periodische Zell-Fracht-Relativbewegung, zusammen mit einer intermittierenden Motilität des gesamten Zelltransporters.

Die experimentellen Beobachtungen weisen darauf hin, dass die Anwesenheit der Fracht als mechanischer Stimulus auf die amöboide Zelle wirkt und zur Zellpolarisation führt, was wiederum die Zellmotilität fördert und die intermittierende Dynamik des Zelltransportes begründet. So wurde festgestellt, dass das Auftreten der Polarisation des Zytoskeletts entlang der Zell-Fracht-Achse von den geometrischen Merkmalen der Fracht, wie zum Beispiel des Partikeldurchmessers, abhängt. Insgesamt wiesen die gesammelten experimentellen Daten auf eine zentrale Rolle der Zell-Fracht-Wechselwirkungen in der Bewegungsdynamik von Zelltransportern hin. Insbesondere kann die Zell-Fracht-Wechselwirkung die Transportfähigkeiten von amöboiden Zellen erheblich beeinflussen, da die Größe der Fracht die Aktivität des Zytoskeletts und die Repolarisationsdynamik entlang der Zell-Fracht-Achse modelliert, wobei letzteres für die Verlagerung und Neuorientierung des Zelltransportes verantwortlich ist.

Darüber hinaus wurde eine Modellierung entwickelt, welche auf den experimentellen Erkenntnissen zum Verhalten der Zelltransporter aufbaut und die relative Dynamik auf Zelltransporterebene, mit der tatsächlichen Partikeltransportdynamik verbindet. Tatsächlich reproduzierten numerische Simulationen des vorgeschlagenen Modells erfolgreich die Phänomenologie des Zell-Fracht-Systems und ermöglichten gleichzeitig die Vorhersage der Transporteigenschaften von Zelltransportern über größere räumliche und zeitliche Skalen. Des Weiteren liefert die theoretische Analyse ein tieferes Verständnis der Rolle der Zell-Fracht-Wechselwirkung beim Massentransport und zeigte insbesondere, wie die Langzeittransporteffizienz durch das Zusammenspiel von Persistenzzeit der Zellpolarität und den Zeitskalen der relativen Dynamik, welche sich aus der Zell-Fracht-Interaktion ergeben, bestimmt wird. Interessanterweise sagt das Modell die Existenz einer optimalen Frachtgröße voraus, wodurch die Diffusivität von Zelltransportern maximiert wird. Dies steht im Einklang mit früheren, unabhängigen experimentellen Daten, für die es vor dieser Studie keine Erklärung gab.

Zusammenfassend lässt sich sagen, dass die vorliegende Forschungsarbeit Licht auf die Bedeutung von Transporter-Fracht-Wechselwirkungen, beim Partikeltransport mittels amöboider Zellen, wirft und eine breite Grundlage für die Analyse und Modellierung komplexer Bio-Hybridssysteme und deren perspektivische Optimierung schafft.

*The most beautiful experience we can have
is the mysterious.*

*It is the fundamental emotion that stands
at the cradle of true art and true science.*

— **Albert Einstein**, *The World as I see it* (1931)

ACKNOWLEDGMENTS

As I approach the completion of this PhD, I ponder retrospectively over the whole remarkable journey that led me here, from primary school to this very moment. And I cannot help but be astonished. All those great moments, all those very tough days... All of it ultimately appears as more than just the sum of each experience. Like a synergistic growth path towards a better me. And now more than ever, it appears clear to me that such successes are not just mine, but *ours* to share, with the many people who made the difference along the way. For this reason It is much important for me to express my gratitude, to at least some of all those amazing human beings I had the luck of stumbling across.

Firstly I want to thank my parents, Edoardo and Betty, for all their sacrifices, all the trust, and all the love they put on me. I cannot really express in words how thankful I am... I would have not gone far without your support.

Thanks Stefano. You believed in me, and persuaded me to do the same and follow my dreams.

Thank you Tamara. Your love was for me like a guiding light, in the darkest moments.

Thanks Nino and Ledia. For being such wonderful friends. No matter the distance, we are never alone.

These years of doctoral studies have been such an enriching experience for me, both personally and professionally; for this, I must thank all the people I worked with. Particularly, I want to mention those who contributed the most to my professional growth.

First of all, a big thank to Prof. Carsten Beta, who has been such a great leader for me. Thank you for your kindness, trust and support. I could not have asked for a better boss!

Heartfelt thanks to all the friends and professors at the Max Planck Institute for Colloids and Interfaces, and in particular to the leading members of the IMPRS who selected me for this PhD position. You gave me an invaluable opportunity that changed my life.

A very special thank goes to Robert Grossmann. Thank you so much Robert, not only for the superb scientific support, but for all I learnt from you. Probably I would not be so proud of my work, if it weren't for you. You are a truly gifted scientist, and I wish you all the best.

Thanks to Oliver, Sven, Maike and Kirsten. You welcomed me among you, introduced me to the wonders of cell biology, and supported me during my first experiments.

Thanks to Ted and Setareh, for being great office mates, and good friends too. I want to further thank Ted, for helping me with the writing of my Abstract in German language.

CONTENTS

I INTRODUCTION

1	ACTIVE TRANSPORT AT THE MICRO-SCALE	3
1.1	A rising need for guided micro-scale transport	3
1.2	Towards a <i>bio-hybrid</i> solution	4
1.3	Crawling cells as carrier entity	8
2	THE “LANGUAGE” OF STOCHASTIC MOTION	15
2.1	Newton laws for drunken: Langevin equations	15
2.2	Deterministic description of mass transport: Fokker-Planck equations	19
2.3	Beyond Brownian diffusion	22

II MATERIALS & METHODS

3	EXPERIMENTAL STRATEGIES AND PROTOCOLS	25
3.1	Cell culturing and biological sample preparation	25
3.2	Particles and microfabrication protocols	26
3.3	Optics and experimental protocols	31
4	COMPUTATIONAL STRATEGIES AND PROTOCOLS	35
4.1	Image Processing	35
4.2	Analysis of cell-cargo dynamics and interaction	45
4.3	Numerical stochastic simulations	52

III RESULTS & DISCUSSIONS

5	PHENOMENOLOGY OF AN AMOEBOID CELL-CARGO SYSTEM	59
5.1	A detailed look at the cellular truck behaviour	59
5.2	Shedding light on cell-cargo relative dynamics	65
5.3	Characterization of cell-cargo interaction	68
6	<i>coarse-grained</i> MODELING OF CELL-CARGO SYSTEMS	71
6.1	Concept and structure of the model	71
6.2	Model predictions	73
7	<i>full-scale</i> MODELING OF CELL-CARGO SYSTEMS	79
7.1	Anatomy of the model	79
7.2	<i>in-silico</i> model testing	82
8	FINAL CONCLUSIONS AND FUTURE PERSPECTIVES	89

IV APPENDIX

A	MAXIMUM LIKELIHOOD-BASED ESTIMATION OF POISSONIAN RATES	95
B	DERIVATION OF A FOKKER-PLANCK EQUATION FOR CELLULAR TRUCKS	97

BIBLIOGRAPHY	103
--------------	-----

LIST OF FIGURES

- Figure 1.1 Visionary design of a biomedical micro-bot, made up by several functional elements for diagnostics and therapy, a targeting unit based on antibodies and a bio-inspired autonomous propelling unit. From [148]. 5
- Figure 1.2 Some design concepts for micro-scale actuation and active transport. From [148]. 6
- Figure 1.3 Examples of the four main strategies used for the assembly of the cell-cargo couple, constituting a bio-hybrid system: **(a)** noncovalent interactions, **(b)** covalent interactions, **(c)** physical entrapment, and **(d)** internalization. From [3]. 7
- Figure 1.4 Schematic representation of Actin-based cell propulsion, from [3]. At the cell's leading edge, cytosolic Actin polymerizes into helical-shaped polar filaments (F-Actin), where Actin monomers actively assemble at one hand while spontaneously disassembling at the other; different auxiliary proteins regulate both dynamics, allowing the cell to control filament size. Bundles of several cross-linked F-Actin filaments actively push the membrane outwards as they grow, forming cell protrusions that will adhere and pull the cell body forward. 9
- Figure 1.5 Schematic representation of Actin filaments distribution within the cell, and their interaction with several different Myosin proteins and F-Actin crosslinking proteins. From [6]. 10
- Figure 1.6 **A-B** In blue, *Dictyostelium discoideum* cell trajectory prior to contact with the cargo (polystyrene microparticle, 20 μm in diameter); in red, trajectory of the cargo as it gets carried along by the cell upon spontaneous adhesion. From [108]. **C** This frame, acquired by fluorescence microscopy, shows an appealing example of multicellular chemotactic transport. In such unpublished experiment, performed by my colleague Setareh Sharifi, starved *Dictyostelium discoideum* cells (fluorescent, shown in green) migrate through an IBIDI μ -Slide chemotaxis chamber following a gradient of chemoattractant ($10 \mu\text{mol l}^{-1}$ cAMP), while forming multicellular aggregates as part of the development process; as they encounter a cargo (polystyrene microparticle, 46 μm in diameter), these motile aggregates adhere and pull it forward, thus performing chemotactic directed transport (from left to right, in around 1h). **D-E** This other example of amoeboid chemotactic cargo transport shows the directional transport of 4.5 μm polystyrene particles into the narrow side channel of a microfluidic chamber, where cAMP is released by photouncaging of BCMCM-caged cAMP (source localized at the bright spot in the channel). Time in h:min. From [108]. 13

- Figure 1.7 (a) Cumulative plot of 27 trajectories of unloaded cell (in red) and 27 trajectories of amoeboid-carried cargoes (in blue, 45 μm polystyrene particles), all starting from the origin and with time duration of 20 min. Kindly provided by Dr. Nagel. (b) Comparison between the spreading dynamics of cell-cargo systems (blue) and the one of unloaded cells (red) using the ensemble-averaged Mean Square Displacement (MSD) $\langle |\Delta r|^2 \rangle$ as metrics. MSD data kindly provided by Dr. Nagel. (c) Estimates of diffusivities \mathcal{D} for amoeboid bio-hybrids loaded with particles of various sizes, obtained from linear fitting $\langle |\Delta r(t)|^2 \rangle \sim 4\mathcal{D}t$ of MSD curves. Bars refer to standard deviation of the fitting parameter \mathcal{D} ; translucent red horizontal band refers to estimate of diffusivity for unloaded cells. The MSD curves used for this estimates have been kindly provided by Dr. Nagel. 14
- Figure 3.1 Picture of the photolithographic mask. 27
- Figure 3.2 Close-up of a microstructure patterned on the master wafer. 29
- Figure 3.3 Schematics of master wafer realization and PDMS moulding. Modified from [165]. 30
- Figure 3.4 Picture of one newly assembled microfluidic chip. 30
- Figure 3.5 Schematic view of the optical path in a confocal microscope. From [106]. 31
- Figure 3.6 (a) Optical Diagram of the LSM 780. From ZEISS operating manual. (b) Visualization of the excitation spectral line and the (detected) spectrum of fluorescence emission for the two fluorophores used. On horizontal axis, the wavelength λ in nm. 32
- Figure 3.7 View of the microfluidic chip, filled and located in the experimental setup. It is possible to visualize some of the 561 nm electromagnetic radiation from the DPSS laser, scattered away from the optical path by the device. 34
- Figure 4.1 **top-left** Typical appearance of a frame from time-lapse recording of cellular trucks, using the optical setup described in Section 3.3. The imaging channel 3 (here in grey scale) allows particle visualization, while channel 1 (in green), barely visible, encodes for the distribution of the fluorescently labeled F-actin. **top-right** Colour-scale visualization of channel 1 from the same frame. **bottom** Histogram of intensities for the channel 1 frame shown above. Intensity is resolved with 16-bit precision; vertical axis refers to pixel count. To make the distribution visible, the sharp peak has been cut (it reaches counts in the order of 10^4); the insert shows a close-up on the peak decay. 37
- Figure 4.2 Close-up on a cell **left** before and **right** after median filtering (mask size $7\text{px} \times 7\text{px}$, $1\text{px} = 0.26 \mu\text{m}$). 37

- Figure 4.3 Schematic view on the two-step histogram transformation. The first transformation (**top to center**) “stretches” the peak while saturating higher intensities. The second one (**center to bottom**) performs a two-sided saturation, non-linearly remapping the pixel intensities in between the two thresholds to optimize contrast among intensities of interest. The non-linearity of the remapping function for the second step (grey line on central figure) has been overemphasized in figure. To make the distributions visible, the sharp peaks have been cut. 38
- Figure 4.4 Glance view of the contrast enhancement occurring during the two-step histogram transformation. 39
- Figure 4.5 Close-up on a binarized cell **left** before any morphological transformations, **center** after *dilation* and **right** after a *dilation-erosion* cycle followed by genus reduction. 40
- Figure 4.6 **a** Frame from a time-lapse recording of a mouse neuroblastoma cell (cell line N1E-115-1), performed by Annie Voigt via Differential Interference Contrast imaging. **b** Artificial image $I_{\text{fictitious}}$ created from image a. **c** Image $I_{\text{fictitious}}$ after median filtering and the previously described two-step contrast enhancement. **d** Image $I_{\text{fictitious}}$ after segmentation (objects too small, or in contact with image edges, have been automatically removed). 41
- Figure 4.7 Accumulating plot of a cell’s boundary, plotted every minute. The colour scale encodes time, from blue ($t = 0$) to red ($t = 7$ min), so to visualize cell shape and position evolving in time. The labeling of boundaries, detected through consecutive frames, as belonging to the same cell is executed by the tracking algorithm. 43
- Figure 4.8 **a** Close-up on a cell, with colour scale encoding the absolute value of the image functional $|E_{\text{image}}(x, y)| = \|\nabla I_{\text{image}}(x, y)\|^2$. The image I_{image} underwent a fine-grain median filtering (impulsive noise removal) and contrast enhancement, prior to calculation of the image functional. **b** Vector map of the resulting GVF force field, with **c** showing a close-up on a protrusion. **d** Visualization of the process of mechanical deformation of a cell boundary, under the effect of the force field. From red to blue, the approximate boundary (in red, here on purpose overly inaccurate) gradually deforms (in green, intermediate state) to converge into a more accurate cell shape (blue). 46

- Figure 4.9 Overview on the type of information, regarding cell-cargo relative motion, extracted from simultaneous tracking of cell and particle. **a** Evolution of the cell relative position $\vec{r}_{\text{rel}}(t)$ around the particle position. Time is colour-coded, from blue to red. **b** Plot of the corresponding time series of relative distance $\|\vec{r}_{\text{rel}}(t)\|$. **c** and **d** are the corresponding Recurrence Plots, respectively, for $\vec{r}_{\text{rel}}(t)$ and $\|\vec{r}_{\text{rel}}(t)\|$. The measure of similarity $I(t_i, t_j)$, properly rescaled, is colour-coded from dark blue ($I = 0$, high similarity) to light yellow ($I = 1$, low similarity). 48
- Figure 4.10 Schematics of the cell-cargo interaction analysis workflow. The time series of relative distance $\|\vec{r}_{\text{rel}}(t)\|$ (**top** figure) is binned into an histogram of frequencies (in the **center**), counting the total time (in frames) spent by the cell within given ranges (the bins) of relative distance from the cargo. Being such counts (properly normalized) an estimate for probability, an effective interaction potential (**bottom** plot) can be calculated from the distribution of frequency by generalizing the canonical distribution. 51
- Figure 5.1 Dual-channel confocal imaging of a *cellular truck*, loaded with a $20\ \mu\text{m}$ spherical polystyrene particle. In green, fluorescent cytoskeletal Actin. In grey-scale, the signal from the transmitted light channel, mapping inhomogeneities in refractive index along the optical path. The spherical particle creates a characteristic refraction pattern, visible in transmitted light as a brighter central area (roughly corresponding to the particle's optical section at the focal plane) surrounded by a dark corona, which fades gradually within the projected area of the particle (here highlighted as a dashed azure circle). Overlaid in solid blue and red, respectively, cargo trajectory (time duration $\Delta t = 27\ \text{min}$) and detected cell boundary and speed vector. 59
- Figure 5.2 **a-b** Multi-channel confocal microscopy images of *cellular trucks*, loaded with **a** $10\ \mu\text{m}$ and **b** $45\ \mu\text{m}$ spherical polystyrene particles. Here, the double-mutant cell strain LimE-mRFP MyoII-GFP AX2 has been employed as carrier, allowing visualization of Myosin II (in red) and F-Actin (in green) proteins distributions. Overlaid in solid blue and red, respectively, cargo trajectory and detected cell boundary and speed vector. **c** Three-dimensional sketch of a cellular truck moving over a flat substrate; cell polarity is represented by color gradient within the cell body, as red and green encode for Myosin-rich and F Actin-rich regions, respectively. 60

- Figure 5.3 **a-c** Multi-channel confocal microscopy images of two cellular trucks, as they go through the three behavioural phases. Particles with diameter of $10\ \mu\text{m}$ and $75\ \mu\text{m}$ have been used as cargoes, respectively for the example on top and the one on bottom images. For the latter, additional close-ups on cell cytoskeletal polarity are provided. **d** Directed graph illustrating the connectivity among behavioural phases. 61
- Figure 5.4 Time series of the relative distance $r_{\text{rel}}(t) = \|\vec{r}(t) - \vec{R}(t)\|$, for a cellular truck loaded with a $45\ \mu\text{m}$ particle. 62
- Figure 5.5 **a** Bottom view and **b** bottom-side view of a cellular truck three-dimensional geometry, reconstructed by z-stacking optical sections. In green, the Actin cytoskeleton; in grey scale, lower spherical cap of the particle, together with a circular halo the particle creates at optical sections above its equatorial plane, as its shape and refractive index mismatch cause lensing. 63
- Figure 5.6 **a** Schematic representation of the broken cytoskeletal symmetry of a cell interacting with a particle. Here, small green circles on the cell membrane correspond to adhesion sites (Actin foci [161]), while vectors represent motor-generated contractile forces exerted on adhesion sites through the Actin network [139]. The same imaginary cell-cargo system is depicted in **b** during the consequent reorientation event (cell advancing towards the cargo while pulling the latter backwards); cytoskeletal polarity is represented by color gradient, as red and green encode for MyosinII-rich (trailing edge) and F Actin-rich (emerging protrusions at leading edge) regions. 63
- Figure 5.7 Microfluidic circuit geometries, here shown from the corresponding master wafers used for soft lithography, imaged in reflected light. Microchannels height and width at constriction are both $5\ \mu\text{m}$ **a** Apolar design, with **b** close-up on a symmetric constriction. **c** Polar design, with **d** close-up on the asymmetric constriction it features. 64
- Figure 5.8 Analysis of the relative cell-cargo motion for three cellular trucks, loaded with particles of different size. **a** Time series of relative distance. **b** Relative cell trajectories with respect to particle position (colour-coded time, from blue to red). **c** Recurrence Plots of the time evolution of cell-cargo relative position $\vec{r}_{\text{rel}}(t)$. **d** Recurrence Plots of the time evolution of cell-cargo relative distance $r_{\text{rel}}(t) = \|\vec{r}_{\text{rel}}(t)\|$. Recurrence plots colour scale: dark blue for $I = 0$, light yellow for maximum I . 66
- Figure 5.9 Statistics on occurrence rate and time duration of reorientation events, for the three tested particle sizes ($10\ \mu\text{m}$, $45\ \mu\text{m}$ and $75\ \mu\text{m}$). Each data point represents an estimate of expected value over a population of 10 cellular trucks, recorded for 45 to 60 min. Bars refer to standard deviation. 67

- Figure 5.10 Estimates of probability density function for the cell-cargo relative distance, along with the inferred effective pair interaction potentials, for three cellular trucks loaded with particles of different size. 68
- Figure 5.11 **a-b** Population-wide estimates of probability density function for the cell-cargo relative distance, along with the inferred effective pair interaction potentials. Each histogram has been obtained from a collection of 10 cellular trucks, recorded for 45 to 60 min, loaded with particles of a given size. In **c**, harmonic fit of the effective potential well for the three distinct populations. Here, the potential shape near the origin (left of the wells) is not being shown: it stems from the left tail of skewed distributions, reflecting the crossing dynamics during reorientation rather than motion around resting position (the energy well); hence, it is not considered in the fitting as the two parts have different physical meanings. 69
- Figure 5.12 Harmonic fit parameters as function of cargo size, obtained from the fitting in figure 5.11c. 70
- Figure 6.1 Markov chain for the coarse-grained physical model of a cellular truck, built upon the experimentally observed behavioural phases (see Section 5.1). 71
- Figure 6.2 A cellular truck trajectory I simulated according to the coarse-grained model (time duration 120 min). In red, truck orientation vector \vec{p} . Parameters set values: $\lambda = (5 \text{ min})^{-1}$, $\alpha = (2 \text{ min})^{-1}$, $\tilde{\sigma} = (6 \text{ min})^{-1}$, $v_{\text{run}} = 6 \mu\text{m min}^{-1}$, $D_{\text{int}} = 1 \mu\text{m}^2 \text{ min}^{-1}$, $\delta\phi \sim \text{Unif}(-\pi, \pi)$, time integration step $\Delta t = 0.1 \text{ min}$. 73
- Figure 6.3 **a** linear and **b** logarithmic plot of the Mean Squared Displacement time evolution $\text{MSD}(t)$ of coarse-grained modelled cellular trucks, for three different values of reorientation rate λ . All the other parameters are set as in figure 6.2. Each curve stems from an ensemble average over 2500 simulated trucks. Simulations have been initialized with the trucks being in state \mathcal{S} . 74
- Figure 6.4 Logarithmic plot of the Mean Squared Displacement time evolution $\text{MSD}(t)$ of coarse-grained modelled cellular trucks, for three distinct cases: **a** simulations initialized in state \mathcal{S} ; **b** simulations initialized in state \mathcal{S} , but run with no noise ($D_{\text{int}} = 0$); **c** simulations initialized in state \mathcal{M} , no noise. All model parameters (except for D_{int} in panels b-c) are set as in figure 6.2. Each curve stems from an ensemble average over 2500 simulated trucks. 76

- Figure 6.5 Curves of predicted long-time diffusivity $\mathcal{D}(\lambda)$ for a range of repolarization rates λ . Each curve refers to a different location in the parameter subspace $v_{\text{run}}\text{-}\tau_{\text{run}}$, pointing out the impact of cell biophysical properties on long-time transport. Solid lines represent analytical solutions (eqn. (6.3)), while markers numerical estimates. Values adopted for the remaining parameters are as in figure 6.2. 77
- Figure 7.1 Schematic illustration of the full-scale model's key elements: the particle (cargo), the cell (active carrier) and the Markov chain governing the motile behaviour of the latter. The **top** three panels depict the configuration of the cell-cargo couple, together with related geometric quantities (see main text), during the three distinct behavioural phases (from left to right, phases \mathcal{S} , \mathcal{R} and \mathcal{M}) manifested by the cellular truck as a whole. **Below**, the Markov chain encoding for the alternation between non-polar and polar biophysical states of the cell, which dictates its intermittent motion. Brackets evidence the link between the truck's behavioural phases and the correspondent state attained by the cell. 79
- Figure 7.2 An example of cellular truck dynamics I simulated according to the full scale model, for a time duration of 100 min. Here, the virtual cell (in light red, with polarity vector \vec{p} in red) is loaded with a virtual particle (gray, trajectory in blue) of $45\ \mu\text{m}$ diameter, hence a repolarization rate $\lambda = 0.1422\ \text{min}^{-1}$ and a resting distance $l_0 = 16\ \mu\text{m}$ are used, conforming to experimental observations (Section 5.2). The values adopted for the other parameters are: $v_{\text{run}} = 6\ \mu\text{m}\ \text{min}^{-1}$, $D = 1\ \mu\text{m}^2\ \text{min}^{-1}$, $\sigma = 0.1\ \text{min}^{-1}$, $D_\varphi = 0.1\ \text{min}^{-1}$, $\alpha = 2\ \text{min}^{-1}$, $D_\Delta = 0.04\ \text{min}^{-1}$, $\eta \sim N(0, 0.2)$, time integration step $\Delta t = 0.1\ \text{min}$. 83
- Figure 7.3 Emergence of the three experimentally observed behavioural phases within full-scale numerical simulations. From top to bottom panel: phase \mathcal{S} (time t , cell in a non-polar low motility state, randomly displacing the cargo), phase \mathcal{R} (time $t + 1\ \text{min}$, cell polarizes and moves persistently towards the current location of the cargo, while pulling the latter towards its rear), phase \mathcal{M} (time $t + 5\ \text{min}$, cell still polarized, carrying the cargo by acting as a puller). The time instants shown here belong to the same simulation as in figure 7.2. 84

- Figure 7.4 Visual comparison between the relative cell-cargo dynamics extracted from a full-scale numerical simulation (same simulation as in figures 7.2 and 7.3) and one extracted from an experimental recording (particle diameter 45 μm). **a** and **e** time series of relative distance; **b** and **f** histograms of relative distance; **c** and **g** relative trajectory of the cell ($\vec{r} - \vec{R}$, frame of reference centred with particle), with colour-coded time (from blue to red); **d** and **h** recurrence plots of the cell relative position $\vec{r}_{\text{rel}} = \vec{r} - \vec{R}$, where the similarity index $I(t_i, t_j) = \|\vec{r}_{\text{rel}}(t_i) - \vec{r}_{\text{rel}}(t_j)\|$ is colour-coded (dark blue for $I = 0$, light yellow for maximum I). 86
- Figure 7.5 **a** Logarithmic plot of the MSD(t) for three different values of repolarization rates λ . All the other parameters are set as in figure 7.2. Each curve stems from an ensemble average over 2500 simulated trucks. Simulations have been initialized with the cell being in isotropic (non-polar) state $s = 1$. **b** Curves of predicted long-time diffusivity $\mathcal{D}(\lambda)$ for a range of repolarization rates λ . Each curve refers to a different value of the parameter v_{run} , to account for variability in cell velocity. Solid lines represent analytical solutions (eqn. (7.3)), while markers estimates from numerical simulations. Values adopted for the remaining parameters are as in figure 7.2. 87
- Figure 8.1 On the **left**, three cells pull a particle in a cooperative fashion, providing cargo transport (in blue, ~ 13 min recording of cargo trajectory). Conversely, in the example on the **right**, two cells pull the particle in roughly opposite directions, thus competing for the cargo; the latter is then stalled in a cellular tug-of-war, fluctuating around its position with no net displacement over time (in blue, ~ 20 min recording of cargo trajectory), as long as tug-of-war symmetry does not break. 91
- Figure 8.2 In the **left** panel, a cell is shown performing active cargo transport, as it pulls on a particle and provides motion (in blue, 27 min recording of cargo trajectory; in red, cell speed direction and boundary). Upon encountering a second cell, the carrying cell reorients away from it; however, the second cell had the chance to adhere onto the cargo, and its pull is now hindering the first cell from moving away with it (**central** panel, 10 min after left panel). It can be noticed how the first cell stretches under the internal reaction within the emerged tug-of-war, with one visible adhesion focus keeping hold onto the particle. Eventually, the tug-of-war resolves, in this case with the previous cargo carrier losing hold and crawling away (**right** panel, ~ 3 min after central panel). 91

Figure 8.3

The illustration on the **left** depicts the spatial configuration of the proposed force measurement experiment, based on the use of an Atomic Force Microscope (AFM). The cell (in green) is put in contact with the particle, the latter fixed onto a cantilever controlled by an AFM: such instrument can work both as actuator (brings the cargo to the cell, and can impose forces/displacements) and as sensing device (can keep the cargo in a fix position by feedback loop control, while recording the reaction forces exerted). The panels on the **right** are pictures of an AFM cantilever functionalized with a $45\ \mu\text{m}$ diameter particle, that I realized as test of feasibility at Max Planck Institute of Colloids and Interfaces, hosted by the Mechano(bio)chemistry group (Dr. Kerstin Blank), upon suggestion of Prof. Dr. Reinhard Lipowsky. The cantilever has been imaged by reflected white light through a stereo microscope, while lying upside-down clamped to a support. Of the three visible cantilevers, the central is the only functionalized, being $350 \pm 5\ \mu\text{m}$ long and $35 \pm 3\ \mu\text{m}$ wide, $2 \pm 0.5\ \mu\text{m}$ thick. The lower panel is a higher magnified side view, with close-up on the particle. 92

LIST OF TABLES

LISTINGS

Part I

INTRODUCTION

ACTIVE TRANSPORT AT THE MICRO-SCALE

1.1 A RISING NEED FOR GUIDED MICRO-SCALE TRANSPORT

As we witness significant growth in the world human population and concurrent increase in life expectancy [169], outcomes of the better life quality and medical assistance modern society can provide, the limited regenerative and homeostatic capabilities of our bodies are put into the foreground. Consequently, the urge to effectively treat pathological tissue conditions as severe traumas, rheumatic and neurodegenerative disorders, and neoplastic diseases (e. g. malignant tumors), is becoming increasingly prominent, with profound impact on our lives, health systems and economies [24, 94, 137, 175].

Conventional pharmacological treatments consist in temporally localized administrations of the therapeutic, the latter free to spread over several districts and tissues of the body (particularly, but not exclusively, in case of systemic administration), reaching only in part the target site. This may be cause of severe side effects, as the drug accumulates in, and interacts with, cells and tissues distinct from the ones it has been designed for [15, 155, 159]. Moreover, to balance out the only partial delivery to target site, higher drug dosages may be used, further aggravating the systemic side effects. A well known example of systemic drug toxicity is represented by the disruptive, potentially lethal, systemic effects of chemotherapeutic drugs, administered as cancer treatment [81, 97, 101].

The groundbreaking, fast-pacing, progresses of the last decades in the field of materials science, particularly polymer science, nano and microtechnology and biomaterials, have enabled the development of innovative strategies for drug delivery, which drew much focus from the scientific community and led to a massive, ever increasing amount of research on advanced drug delivery systems [66, 67, 85, 86, 135, 158, 159].

In fact, new “smart” materials and devices are being developed, able to release a therapeutic with a dynamic, programmable and *stimuli-responsive* kinetics, for longer time and with specific affinity to the target site, paving the way towards safer and more effective therapies [66, 85, 118, 127, 135]. Among others, much enthusiasm is currently devoted to polymers, often of biological origin, engineered to modulate their degradation and/or interaction with drug molecules according to environmental parameters, such as pH, temperature, presence of specific enzymes [49, 79, 85, 127, 138, 174]. In addition, micro and nanoparticle-based administration of genetic material, as plasmid DNA or mRNA, has proven its therapeutic potential, already reaching clinical settings in numerous cases [19, 96, 115]; an example, particularly relevant for society at this current date, is the SARS-CoV-2 (COVID-19) nanoparticle-based vaccine developed by BioNTech (Mainz, Germany), currently undergoing clinical trials [104].

New frontiers in materials science and micro/nanotechnology are not just reshaping drug delivery, but the biomedical ecosystem as a whole; particularly, we are witnessing a variety of new diagnostic tools, from cancer-labeling nanoparticle to microscopic biosensors for bio-analytic measurements [32, 117, 145, 149, 163]. Some of the most

advanced nanoelectronics-based sensors are even capable of processing and storing the collected information, all on micron-sized particles potentially able to reach narrow districts as within human tissues [80].

As society leans towards devices miniaturization and precision medicine, however, the manipulation, transport and control capabilities at the micro-scale gradually become major limiting factors in the development and use of such new technologies.

Indeed, when it comes to nanoparticle-based delivery of drugs and genetic material, relying only on their passive diffusion and advective transport through blood and interstitial fluids (i. e. blood circulation and extravasation) has been proven poorly effective for several applications: administered drug-delivering particles tend to accumulate in numerous tissues and organs, particularly liver, spleen and lungs, which may not be the intended targets; as a consequence, delivery of the therapeutic agent to the target site occurs only to a limited extent, in amounts as low as 5% [15]. Functionalization of the nanoparticles to provide specific target affinity (e. g. specific ligand–receptor interactions), albeit it promotes targeted delivery, has been shown to be often insufficient to grant increased accumulation of the nanoparticles in target sites as tumours [77, 100, 123]: such specific interactions tend to be short-ranged (< 0.5 nm) [15], and most nanoparticles would still accumulate in other body districts before casually encountering their target.

As we consider bigger systems, as microparticles and other microscopic devices, their targeted delivery gets even more challenging. Such objects, crossing the edges of the colloidal scale, may not exhibit significant diffusive transport and may be prone to sedimentation, which could limit their access into tissues [7], restricting their use to high-flow environments, airways and digestive tract, or to delivery routes as local injection/surgical insertion (routes that assume specific knowledge on e. g. tumour cells location and physical access to it).

In an effort to address such issues, the novel, highly multidisciplinary research fields of micro-scale actuation and *guided transport* are quickly gaining momentum, thanks to the many technological challenges yet to be overcome and their potential impact on paramount applications [148].

1.2 TOWARDS A *bio-hybrid* SOLUTION

The targeted delivery of micron-sized objects, from drug-releasing microparticles to nanoelectronics-based biosensors, could ideally make use of self-propulsion to perform active locomotion, thereby enabling effective transport.

According to such concept of *active guided transport*, the therapeutic particle/device, representing the *cargo*, would rely on an out-of-equilibrium propelling entity, or *carrier*, which exploits some kind of energy source to produce displacement. In order to accomplish *autonomous* steered motion, an ideal propelling system would need to be “smart”, i. e. performing a closed-loop locomotion which allows micron-sized cargoes to be displaced toward a specific site, through complex and crowded environments such as human tissues [148].

In the last years, a diverse multitude of systems has been proposed and tested for the execution of micro-scale active transport, broadly classified into synthetic micro-propellers, bio-inspired micro-bots and bio-hybrid systems [147].

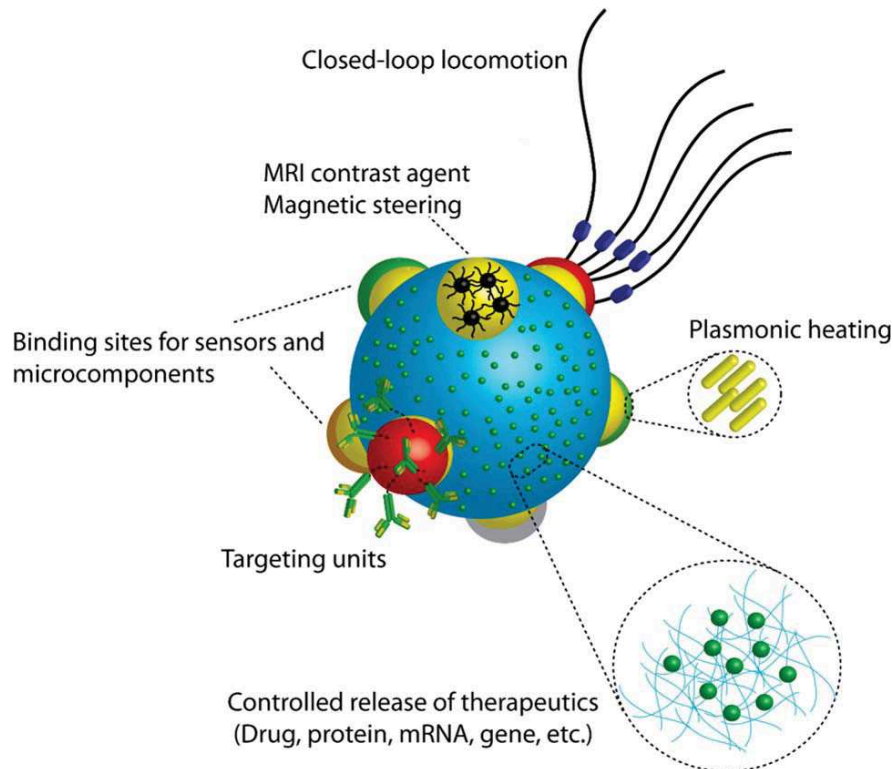


Figure 1.1: Visionary design of a biomedical micro-bot, made up by several functional elements for diagnostics and therapy, a targeting unit based on antibodies and a bio-inspired autonomous propelling unit. From [148].

Synthetic micro-propellers usually rely on an asymmetric surface chemistry, reactive to chemicals in the surrounding fluids, to generate thrust (e. g. [151]), or alternatively on a magnetic body to exert pull as they interact with external magnetic fields (e. g. [82]): they can be attached to the diagnostic/therapeutic microscopic device, thus acting exclusively as carrier, or constitute themselves the biomedical device if properly functionalized (e. g. fabricating them with drug releasing materials [30]).

Bio-inspired micro-bots represent, so to say, an evolution of synthetic propellers: their design being optimised using motile living cells as inspiration, they usually consist of synthetic micro-swimmers of elaborated shape, in an effort to improve carrier motility; they are typically powered and controlled by external magnetic fields [113, 120].

Despite much progress in the design of microscopic synthetic propellers and bio-inspired robots, several well-documented technological challenges are still unaddressed, greatly limiting their effective use in a biomedical context. In fact, being relatively primitive carrier designs, these systems are currently unable to achieve autonomously steered locomotion through the body, and their guidance, when possible, usually requires sophisticated and bulky external units for magnetic driving; moreover, their energy efficiency is relatively low, especially when compared to biological motile entities (orders of magnitude more efficient), and even finding a harmless and reliable energy source may be challenging [1, 28, 71, 130, 146, 148, 164]. Last but not least, the often overlooked interaction with the immune system may severely constrain their design and efficiency [173].

With a shift of paradigm, *bio-hybrid systems* make use of autonomous micro-actuation solutions already provided by Nature, rather than striving to, so to say, “reinvent the wheel”: by employing motile living cells as carrier/actuation elements, a cell’s intrinsic sensing mechanisms can be exploited to achieve autonomous guided transport. In fact, such biological entities are endowed with a built-in closed-loop locomotion machinery, assembled from highly efficient molecular motors into multiscale ensembles with integrated control systems, responsive to local environmental stimuli and self-powered by a metabolism feeding on physiologically available nutrients [3, 28, 130, 148].

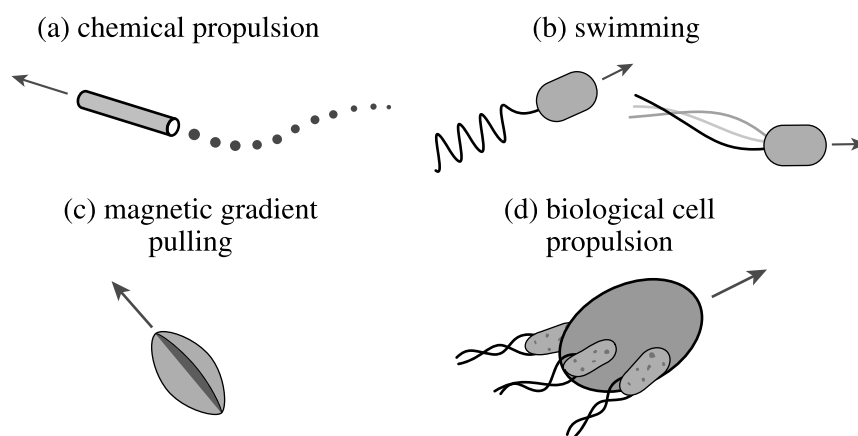


Figure 1.2: Some design concepts for micro-scale actuation and active transport. From [148].

The effective and robust self-guiding of motile cells is, indeed, what makes several paramount and highly complex physiological processes possible, among others the morphogenesis of multicellular organisms (e. g. animal embryogenesis), wound healing, and the fast migration of leukocytes towards a site of inflammation/infection; further, it governs the progression of some pathological conditions (e. g. tumor metastatization), and the survival of microorganisms as bacteria searching for nutrient-rich environments [56, 76, 131, 136]. Motile cells direct themselves towards a target by means of a variety of mechanisms, usually relying on sensing external gradients of specific chemicals, e. g. cytokines, eventually released by target cells/tissue; these signaling molecules can then act as attractant and lead the way to the site of interest, in a robust migratory process named *chemotaxis* [13, 41, 56] (or *aerotaxis*, when the attractant is molecular oxygen [70]). In addition, some prokaryotes can further orient according to the local magnetic field, as for *magnetotaxis*, thanks to intracellular biomineral ferromagnetic structures [16].

The exploitation of these very same strategies of directed migration is in fact a major focus of bio-hybrid systems research, particularly when it comes to targeted delivery, as documented by the numerous papers and reviews addressing the topic [3, 27, 31, 50, 52, 69, 172].

Among others, much attention is being devoted to the development of bio-hybrids based on swimming cells, such as bacteria chemotactically navigating and/or magnetically steered to target sites [27, 177], or eukaryotic alternatives as sperm cells [31, 171]. Such studies have made use of a diverse range of strategies for the assembly of the bio-hybrid system, where the cargo is either fixed onto the exterior of the cell (covalent or non-covalent bonding, physical entrapment) or internalized in the cell body (see Figure 1.3).

Crawling cells as neutrophils, monocytes/macrophages or other immune cells have also been investigated, as they are native (thus non immunogenic and optimized for migration through our tissues) and chemotactically recruited to critical targets as tumor tissue [34, 64, 143, 172]. Here, fabrication of the bio-hybrid system has mostly been based on internalization, making use of the phagocytic response of these cells as they interact with therapeutic nano/microparticles.

Upon successful targeting, a bio-hybrid unit may exploit distinct local microenvironmental conditions, intrinsically associated to certain diseases or artificially induced, as a trigger to selectively release the loaded cargo/therapeutic molecules. Stimuli-responsive materials and/or cell-cargo linkings have in fact been adopted for such purpose, providing release mechanisms based, among others, on local pH, temperature or chemical reactions [34, 116, 152, 154, 166].

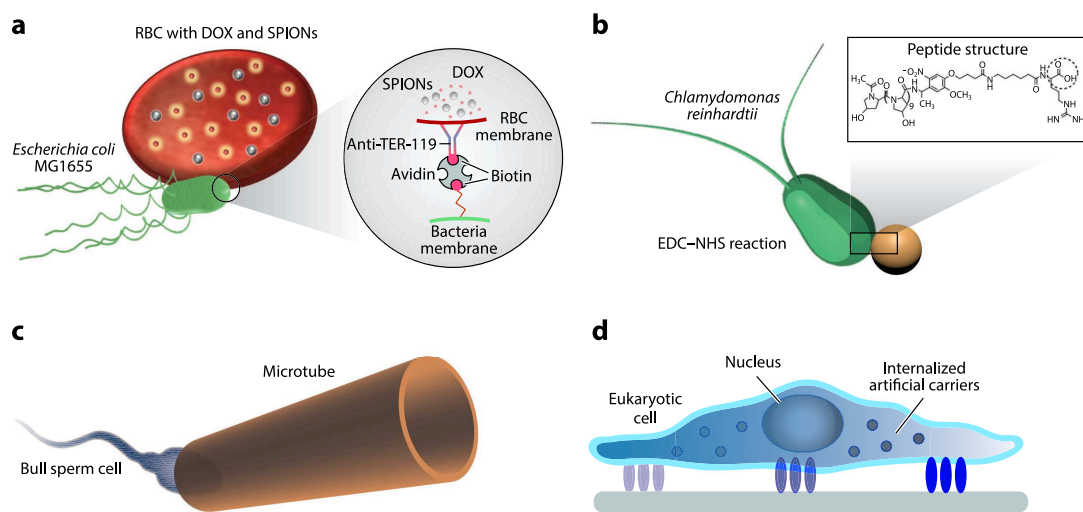


Figure 1.3: Examples of the four main strategies used for the assembly of the cell-cargo couple, constituting a bio-hybrid system: **(a)** noncovalent interactions, **(b)** covalent interactions, **(c)** physical entrapment, and **(d)** internalization. From [3].

Despite their proven transport capabilities and potential applications for minimally invasive therapies, the medical use of bio-hybrid systems still holds at an early stage of development, hampered largely by complications inherent to immunogenicity and overall safety of this new technology. As a matter of fact, most of the microorganisms adopted in current bio-hybrid solutions would trigger host immune responses, compromising delivery effectiveness, and may even represent a direct threat themselves, if able to proliferate and carry out pathogenic activity [3, 48, 156].

The already mentioned use of endogenous cells, as leukocytes, is consequently getting increasing attention, being biocompatible, non-immunogenic, and potentially the most effective in terms of targeted delivery. However, existing leukocyte-based bio-hybrids normally rely on internalization of the therapeutic cargo, which raises concerns on the impact of internalized molecules/particles on viability, behaviour, and genetic material of the cells [3]. Moreover, internalized drugs may undergo significant degradation within the cell body, and show reduced release rate[43]; efficient and localized cargo release may require intentional induction of cell death (e. g. via externally induced hyperthermia), not quite a desired fate for in-vivo leukocytes [34].

To date mostly unexplored [108], bio-hybrid systems harnessing crawling native cells like leukocytes, without internalization, represent a promising solution to achieve safe and effective cargo transport, with more flexibility in terms of delivery mechanisms. Such idea, being foundational for the content of this Doctoral Thesis, is discussed in the next section.

1.3 CRAWLING CELLS AS CARRIER ENTITY

As mentioned in the previous section, an emerging trend in fields such as targeted delivery and medical micro-robotics is the use of leukocytes as smart carriers of micro/nano-cargoes, creating a functional and autonomous bio-hybrid entity from native cells of the organism (which may be named *immunobot*, a term of recent introduction [173]). This fact may not seem very surprising, as leukocytes are well known for their meritorious migrational capabilities, granting them access through dense extracellular matrices and across a multitude of biological and physical barriers, deep into most, if not all, tissues of the body: here stems their unique potential as delivery agent into hard-to-access districts for numerous pathologies [11, 54, 56, 105].

A leukocyte's ability to migrate, and in turn the potential performances of a leukocyte-based bio-hybrid, are tightly bound to the specific biophysics governing the motion of such cell type. Considered by many the most effective type of cell migration [56], the motility mechanism adopted (among many other mammalian cells) by leukocytes goes under the name of *amoeboid motion*.

THE AMOEBOID MOTION

Cell crawling refers to the locomotion mechanisms adhering motile cells rely on, in order to displace themselves with respect to the substrate they interact, and ultimately migrate [9, 18]. It is therefore performed by most eukaryotic cells, and plays a central role in several physiological and pathological processes [162]. Given its importance, the crawling motility of cells had received much attention in the last decades, from biologist and biochemists to physicists, mathematicians and engineers alike, resulting in a substantial and multidisciplinary amount of research of both experimental and theoretical/computational nature. Several recent textbooks, reviews and research articles cover the topic from different standpoints, describing its biochemistry and biophysics and addressing the still numerous open questions (e. g. [9, 12, 18, 139]).

Among other identified cell crawling modes, the amoeboid motion is a fairly widespread crawling mechanism, adopted by a number of mammalian cell types as leukocytes, many stem cell lines, allegedly some tumour cells, and (as the name suggests) microorganisms belonging to the genus *Amoeba* [56, 89, 112]. Compared to the other crawling modes, as mesenchymal or keratocyte-like crawlings, amoeboid crawling stands out for its speed (reaching between 10 and 30 $\mu\text{m min}^{-1}$, in contrast with $\sim 1 \mu\text{m min}^{-1}$ for mesenchymal mode), the lack of strong adhesive interactions with surrounding tissue (it relies on non-specific, weak interactions with the substrate), and the ability to move through tissues while preserving their integrity (rather than degrading it by proteolytic activity). In fact, this fast low-affinity crawling, featuring major dynamical changes in cell shape, enables versatile and efficient interstitial migration, even across biophysical barriers as during the process of diapedesis (extravasation). [56, 157, 168]

Despite the reported diversity in cell crawling modes, they all share the same underlying concept of Actin-based cell propulsion. First identified in the late 70s [2], the Actin-driven motility manifested by eukaryotic cells relies on cyclic cell shape changes, where membrane protrusions (commonly referred to as pseudopodia) extend from the cell body to adhere further, thus defining a leading edge which pulls the cell forward (Figure 1.4).

A globular protein called Actin, a main component of the cell cytoskeleton, plays a fundamental role in this process: Actin molecules dispersed within the cytosol can actively assemble into a filamentous structure called F-Actin (filamentous Actin), where they act as monomeric units; the concurrent polymerization of several Actin filaments, activated by energy-rich ATP molecules, nucleating at the cell's leading edge forms rigid bundles of F-Actin, which are in fact responsible for protrusion growth as they push the membrane outwards. Taken alone, the growth of F-Actin bundles at the cell front would only produce relative motion between cell membrane and Actin superstructures, since such internal forces would not perturb the momentum of the whole cell¹. Net displacement happens as these Actin structures are physically connected to the rest of the cytoskeleton, which in turn anchors to the substrate by means of transmembrane proteins; the latter adhere and transmit forces onto the substrate, thus granting the cell center of mass to move with respect to it. [18, 68, 124]

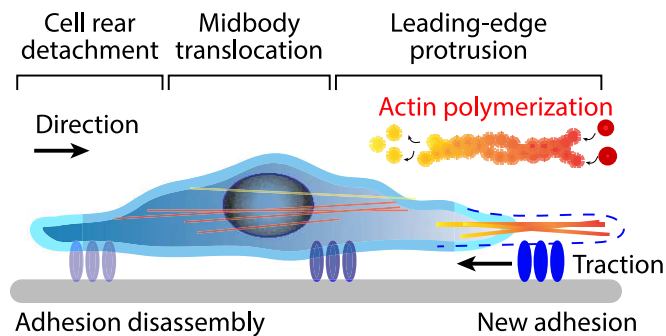


Figure 1.4: Schematic representation of Actin-based cell propulsion, from [3]. At the cell's leading edge, cytosolic Actin polymerizes into helical-shaped polar filaments (F-Actin), where Actin monomers actively assemble at one hand while spontaneously disassembling at the other; different auxiliary proteins regulate both dynamics, allowing the cell to control filament size. Bundles of several cross-linked F-Actin filaments actively push the membrane outwards as they grow, forming cell protrusions that will adhere and pull the cell body forward.

In its entirety, the cell cytoskeleton represents a very complex molecular machinery, an ever-restructuring active biopolymer network, maintained in a tightly regulated out-of-equilibrium state. It consists of a complex assembly of three main structural components, the cytoskeletal filaments Actin, Microtubules, and intermediate filaments, interacting with each other and with several auxiliary proteins and molecular motors, e. g. Myosin proteins. The resulting active network is highly structured and dynamic, responding to external and internal stimuli by means of complex and

¹ Being in overdamped regime, reciprocal deformations of a body (as extensions and retractions) cannot produce any displacement of its center of mass.

not fully understood pathways of biochemical reactions; once triggered, cytoskeletal restructuring resolves on the time scale of minutes. [6, 68, 139]

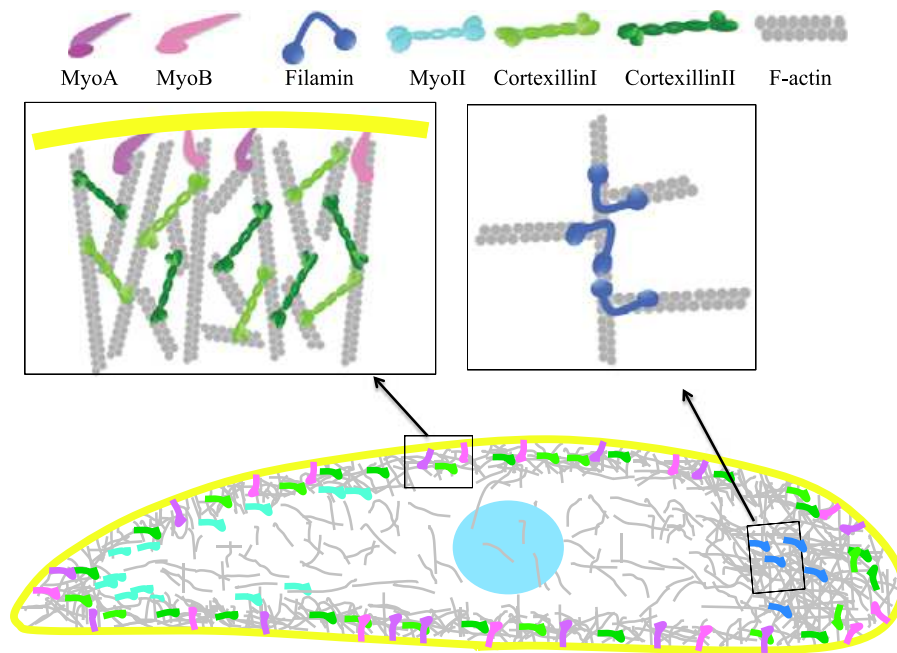


Figure 1.5: Schematic representation of Actin filaments distribution within the cell, and their interaction with several different Myosin proteins and F-Actin crosslinking proteins. From [6].

Cell crawling ultimately manifests as a 3-step cyclic process, markedly defined in the case of amoeboid crawling: Actin-driven *protruding* of the cell towards the direction of motion; *adhesion* of the newly formed protrusions onto the substrate; *retraction* of the rear part of the cell body, which loses adhesion and is consequently pulled forward [9].

Upon protrusion maturation and adhering, a contractile force is created at the cell rear as Actin filaments within the whole cytoskeleton interact with motor proteins, particularly Myosin II. In fact, by means of a three-step ATP-powered process (Myosin binding, power stroke, and unbinding from Actin filaments [4]), Myosin proteins exert force to pull/slide Actin filaments relatively to each other. Actin filaments, other than protruding bundles, build up several different superstructures within the cell, particularly the Actin cortex (a contractile actin structure at the boarder to the plasma membrane), Actin foci (dense regions of Actin cortex at substrate-adhering sites), and extended cytosolic bundles (e. g. stress fibers) connecting distal sites of adhesion and other Actin structures to allow force transmission [68, 161]; as Myosin motors contract such cytoskeletal networks, rear-most adhesions disrupt and the cell body is pulled towards the remaining adhesions, i. e. in the direction of migration [9, 75, 129].

As a consequence, during the cyclic process of cell crawling the cell shows a polarized configuration of its cytoskeleton, with a leading edge (where protrusions are formed) rich of newly polymerized Actin structures, and a rear rich in acto-myosin complexes (which pull the cell body) [129]. For this propulsion mechanism to be carried out, the cell must periodically change its shape, overcoming the cortical tension (generated by the interaction of Actin cortex and Myosin proteins) by means of its cytoskeletal machinery [6].

In the absence of external stimuli, protrusion formation arises at random, hence cell migration manifests as an unbiased random motion. This, for example, allows cells to probe the surroundings, sensing and integrating signaling inputs that may be scattered within the extracellular environment, as during the scanning of cellular networks and tissue antigens, or the search for pathogens within the body [55, 56]. Conversely, external stimuli as chemoattractant gradients can break cytoskeletal symmetry in a consistent manner, favouring protrusion formation/survival towards a certain direction thus biasing a cell's random walk [10, 51, 129].

A considerable amount of mathematical modelling, experimental and theoretical analysis has been performed in the last few decades, in an effort to achieve a better understanding of the random motion performed by crawling cells in different conditions (e. g. [5, 8, 12, 26, 33, 90, 102, 140]).

FROM EARLY STUDIES TO THE SCOPE OF MY WORK

As discussed previously (Section 1.2), the use of crawling cells like leukocytes as carrier entity is a relatively new concept, typically limited by a paradigm of internalization of the therapeutic cargo as bio-hybrid fabrication technique: though with some promising results, research pointed out unwanted side-effects associated with particle and drug internalization.

In order to address such matter and possibly harness the full potential of immune cell-based bio-hybrids, a USA-based team of researchers led by Prof. Dr. Samir Mitragotri and Prof. Dr. Michael F. Rubner first proposed, in a publication from 2011, a paradigm shift where phagocytosis-resistant drug-releasing microparticles are carried like "backpacks" by leukocytes, without internalization [43]. Here, the cargo is fixed onto the exterior of a macrophage by means of non-covalent interaction, and the bio-hybrid system self-assembles spontaneously as these leukocytes establish contact with such particles.

Prof. Mitragotri and collaborators went further, publishing in 2014 a study on the *in vitro* and *in vivo* transport of such drug-releasing backpacks, using monocytes as carriers to target sites of tissue inflammation [11]. The team of scientists proved here the ability of this kind of bio-hybrid system to penetrate tissues, crossing barriers as endothelial cell layers, while retaining their cargo and preserving key cellular functions as the ability to differentiate into macrophages at a site of inflammation. Moreover, they reported targeted transport and selective delivery of the cargo to inflamed tissue in mice, for two distinct inflammation models (skin and lungs).

Despite such promising results, the research on amoeboid-moving cells carrying therapeutic microparticles onto their external surface is rather recent. To the best of my knowledge, the mentioned authors are the only ones, other than the research group I belong, to ever publish on this concept; their application-oriented studies give credit to this transport strategy, yet provide little knowledge on the underlying mechanisms governing it and no physical characterization of the motile behaviour and dynamics.

In the Biological Physics research group at the University of Potsdam, led by Prof. Dr. Carsten Beta, we investigate this innovative approach of active transport at the micro-scale from a physical perspective, relying on quantitative approaches as analysis and modelling of trajectories, micro-manipulation and force measurements. For this purpose, we employ the amoeba *Dictyostelium discoideum* as model of cellular carrier,

being a renowned model organism for leukocyte migration and, in general, for eukaryotic cell motility [13, 54]. As a matter of fact, this easy-to-handle unicellular organism shares with leukocytes the motility strategy of amoeboid crawling, and manifests a remarkably similar chemotactic behaviour. For *Dictyostelium discoideum* cells, the latter triggers in a condition of starvation, guiding them towards each other in order to form multicellular aggregates; following aggregation, a morphogenetic process (referred to as development) causes cells to differentiate and ultimately produce the so-called fruiting body, which releases *Dictyostelium discoideum* spores possibly spreading in more favorable nutrient-rich environments [167]. This innate chemotactic response can be exploited to purposely guide their otherwise unbiased vegetative migration, so to simulate leukocyte chemotaxis in various conditions of interest: once properly starved, *Dictyostelium discoideum* cells become responsive to their chemoattractant, the cyclic nucleotide cAMP, and follow any external gradient of it; one can then drive their migration towards a specific location by means of an external controlled release of cAMP on-site, or simply direct them along a cAMP gradient established with microfluidic tools [108].

The first studies conducted by Prof. Beta and his team, prior to my doctoral work, culminated in the publication of a research article, reporting novel experimental evidence on amoeboid crawling cells achieving various tasks of micro-cargo transport and manipulation [108]. Particularly, *Dictyostelium discoideum* cells spontaneously carried micron-sized objects along, as they got in contact with them while freely crawling (Figure 1.6A-B); in presence of a chemoattractant gradient, such cells established a net flow of microparticles along its direction, and a localized chemoattractant source successfully led to accumulation of cargoes at its location, even through constraining geometries (Figure 1.6D-E).

Multicellular transport, emerging as several cells interact with the same cargo, proved to be a robust transport strategy especially suited for bigger objects: moving aggregates of starved cells (spontaneously forming as part of the development process) were able to transport cargoes in a directed fashion (Figure 1.6C), cooperatively moving objects up to more than one order of magnitude bigger than individual cells; when collected towards a localized cAMP source, objects initially scattered over the substrate clustered together, with the tendency, to some extent, of aligning side by side. This latter fact suggested cell-driven self-assembly of microstructures as possibly achievable task, a rather advanced application which still needs to be further investigated. More research is currently being performed on multicellular transport by my colleagues, together with studies on amoeboid-mediated cargo transport in *in vivo*-like experimental conditions, as chemotactic cargo transport through tissue-like hydrogel media like collagen and gelatin.

Such growing amount of experimental evidence on amoeboid transport made increasingly manifest the complexity of this process, and pointed out a lack of understanding of the underlying mechanisms leading to the observed dynamics of cargo transport. In an effort to shed some more light on this bio-hybrid transport, Dr. Oliver Nagel performed force measurements and quantitative analysis on trajectories as part of his doctoral thesis [107], focusing on the cell-cargo couple i. e. the simplest, minimal unit of amoeboid transport. Surprisingly, by comparing the unbiased (not chemotactic) motion of unloaded *Dictyostelium discoideum* cells with cargo-loaded ones (the actual bio-hybrids), Dr. Nagel found out a generally faster spreading of the latter,

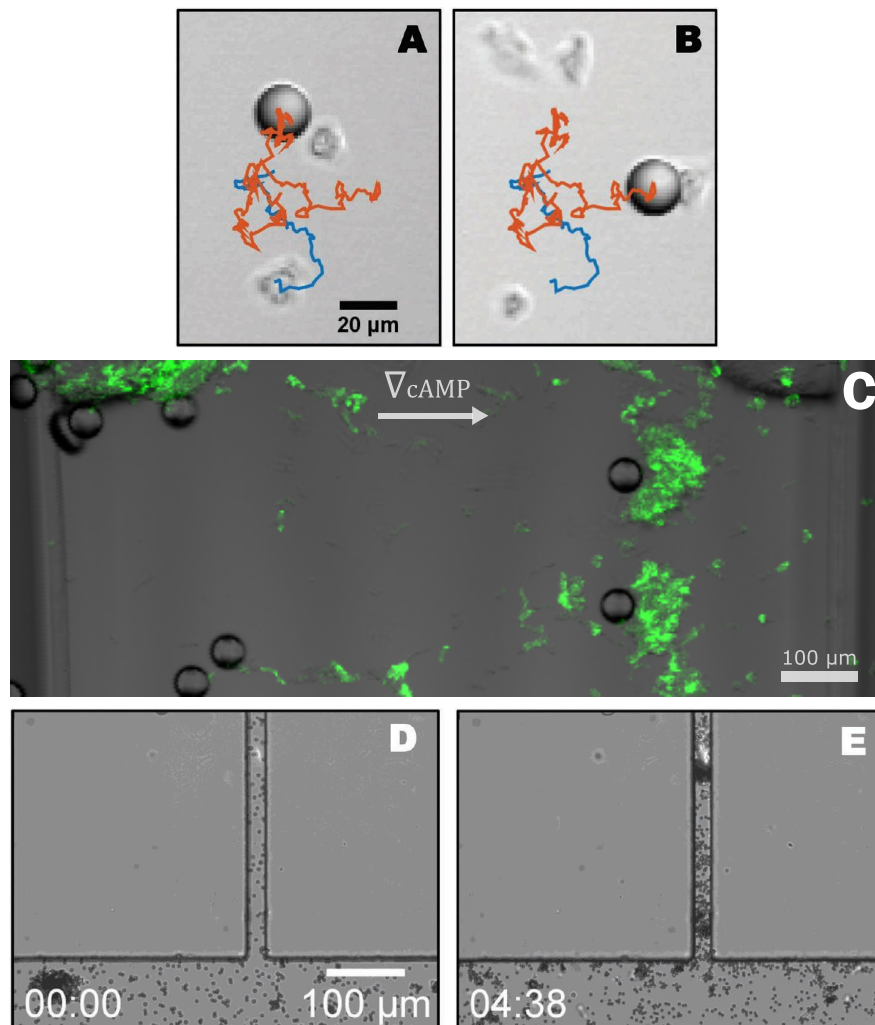


Figure 1.6: **A-B** In blue, *Dictyostelium discoideum* cell trajectory prior to contact with the cargo (polystyrene microparticle, 20 μm in diameter); in red, trajectory of the cargo as it gets carried along by the cell upon spontaneous adhesion. From [108]. **C** This frame, acquired by fluorescence microscopy, shows an appealing example of multicellular chemotactic transport. In such unpublished experiment, performed by my colleague Setareh Sharifi, starved *Dictyostelium discoideum* cells (fluorescent, shown in green) migrate through an μSlide chemotaxis chamber following a gradient of chemoattractant ($10 \mu\text{mol l}^{-1}$ cAMP), while forming multicellular aggregates as part of the development process; as they encounter a cargo (polystyrene microparticle, 46 μm in diameter), these motile aggregates adhere and pull it forward, thus performing chemotactic directed transport (from left to right, in around 1h). **D-E** This other example of amoeboid chemotactic cargo transport shows the directional transport of 4.5 μm polystyrene particles into the narrow side channel of a microfluidic chamber, where cAMP is released by photouncaging of BCMCM-caged cAMP (source localized at the bright spot in the channel). Time in h:min. From [108].

as the presence of the cargo would somehow affect positively the migrational abilities of the cell (Figure 1.7a-b). In addition, by comparing amoeboid bio-hybrids loaded with particles of different sizes, he reported a rather counterintuitive non-monotonic dependence on cargo size for the bio-hybrid estimated diffusivity (Figure 1.7c).

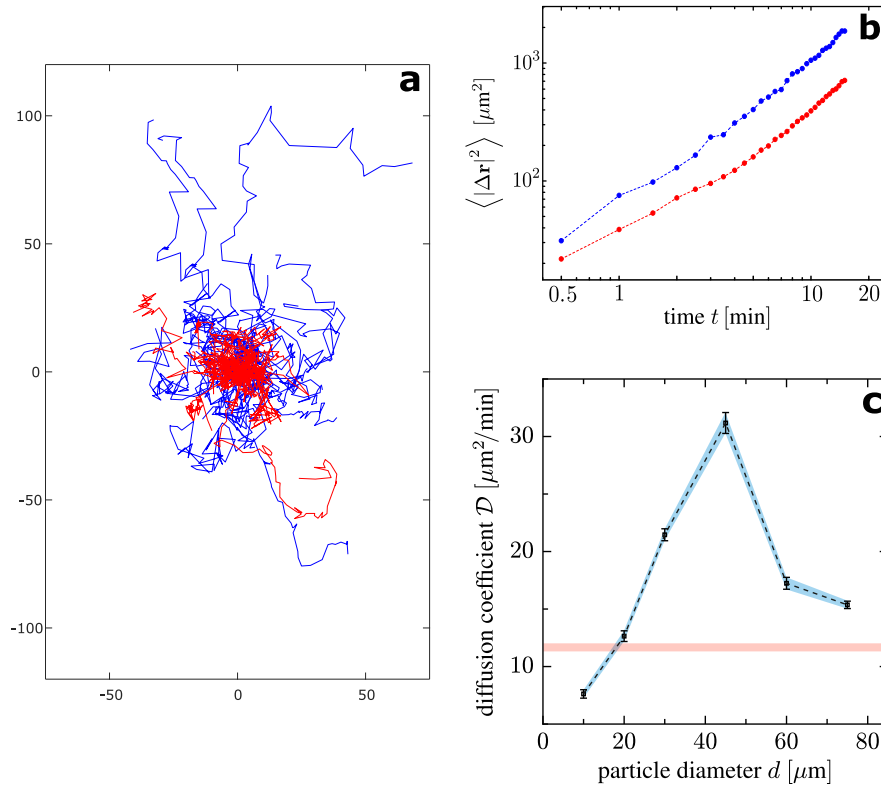


Figure 1.7: **(a)** Cumulative plot of 27 trajectories of unloaded cell (in red) and 27 trajectories of amoeboid-carried cargoes (in blue, 45 μm polystyrene particles), all starting from the origin and with time duration of 20 min. Kindly provided by Dr. Nagel. **(b)** Comparison between the spreading dynamics of cell-cargo systems (blue) and the one of unloaded cells (red) using the ensemble-averaged Mean Square Displacement (MSD) $\langle |\Delta r|^2 \rangle$ as metrics. MSD data kindly provided by Dr. Nagel. **(c)** Estimates of diffusivities \mathcal{D} for amoeboid bio-hybrids loaded with particles of various sizes, obtained from linear fitting $\langle |\Delta r(t)|^2 \rangle \sim 4\mathcal{D}t$ of MSD curves. Bars refer to standard deviation of the fitting parameter \mathcal{D} ; translucent red horizontal band refers to estimate of diffusivity for unloaded cells. The MSD curves used for this estimates have been kindly provided by Dr. Nagel.

Overall, his work highlighted once more the intriguing yet puzzling behaviour of this novel kind of bio-hybrid system, raising more open questions even at the foundational level of unbiased single-celled transport.

The purpose of my doctoral research has been so to *unveil the fundamental mechanisms* governing the random motion of an amoeboid bio-hybrid system, and *build a physical model* able to describe its complex behaviour and transport capabilities.

This Chapter is intended to be an *essential* introduction to the mathematical description and theoretical study of random motion: it is aimed at providing the reader with a handful of physical and mathematical concepts and theoretical tools, believed to be necessary for a full understanding of the results discussed in this thesis (especially Chapters 6 and 7, and Appendix B). For a more exhaustive treatise, a curious reader can refer to several excellent textbooks and review articles, for example [99, 133, 134] which have been inspirational for the writing of this Chapter.

2.1 NEWTON LAWS FOR DRUNKEN: LANGEVIN EQUATIONS

The intrinsically unpredictable nature of random motion impedes the scientist from describe such type of processes using deterministic laws of motion. To address such issues, French physicist Paul Langevin (1872 - 1946) conceived the idea of accounting for such erratic component of motion, by introducing additional forces of stochastic nature into much-familiar equations of Newtonian mechanics, giving birth to the so-called *Langevin equations*.

For example, one may describe the motion of a small¹ entity, such as a molecule or a colloidal particle or even a microorganism, through a fluid medium, by means of a second-order stochastic differential equation of the type:

$$\frac{d^2 \vec{r}}{dt^2} = -\frac{\eta}{m} \frac{d\vec{r}}{dt} - \frac{1}{m} \nabla U(\vec{r}) + \frac{1}{m} \vec{\mathcal{R}}(t) \quad (2.1)$$

(η Stokes friction coefficient, m particle mass) which consists of a dissipative Newtonian dynamics (friction term $-\frac{\eta}{m} \frac{d\vec{r}}{dt}$) where $\nabla U(\vec{r})$ accounts for external (conservative) force fields, and $\vec{\mathcal{R}}(t)$ represents a random force, here assumed homogeneous in space, acting as a noise perturbing the particle trajectory. This random force will then be generated by a proper stochastic process, designed to describe a certain unpredictable behaviour of the system of interest.

Clearly eqn. (2.1) is a linear differential equation, as all Langevin equations involved in this thesis. Nonetheless, for the sake of completeness, it should be mentioned that this may not always be the case, as for more complex phenomena where one must include non-linear effects for dissipative and/or random forces. In a more general case, a Langevin equation would then assume a form of the type:

$$\frac{d^2 \vec{r}}{dt^2} = \frac{1}{m} \left[-\vec{\mathcal{F}}\left(\frac{d\vec{r}}{dt}, t\right) - \nabla U(\vec{r}) + \vec{\mathcal{R}}\left(\frac{d\vec{r}}{dt}, t\right) \right]$$

with $\vec{\mathcal{F}}$ and $\vec{\mathcal{R}}$ respectively friction and random forces with potentially non-linear dependence from the particle velocity $\frac{d\vec{r}}{dt}$.

As happens often in the microscopic and colloidal world, objects move in over-damped conditions, i. e. $\frac{\eta}{m}$ “large” $\implies m \frac{d^2 \vec{r}}{dt^2} \ll \eta \frac{d\vec{r}}{dt}$, thus inertial effects (the

¹ but not *too* small, so to rightfully neglect its quantum nature.

acceleration term $\frac{d^2 \vec{r}}{dt^2}$) may be neglected, meaning that the forces acting on such objects get balanced (or, in other words, the energy objects receive gets dissipated) by the dissipative forces (friction term) in a very short time. Consequently, it is not uncommon to find first-order Langevin equations, namely first-order stochastic differential equations for the description of a particle's position time evolution².

A CASE STUDY: BROWNIAN MOTION

As didactic example of Langevin dynamics, let's consider a particle with mass little enough so that velocity perturbations, due to thermal fluctuations, are significant in determining the actual motion of it. The thermal agitation manifested by such entity goes under the name of *Brownian motion*, the quintessential random motion.

For the sake of simplicity, let's consider its Langevin dynamics in the absence of external force fields and, for the moment, along just one of the spatial dimensions. From eqn. (2.1) we get ($\frac{dx}{dt} = v_x$):

$$\frac{dv_x}{dt} = -\gamma v_x + \frac{1}{m} \mathcal{R}(t) \quad (2.2)$$

where $\gamma^{-1} = \frac{m}{\eta}$ is dimensionally a time. In order to account for the empirical evidence on thermal agitation, we may idealize $\mathcal{R}(t)$ as a *white noise*, or Wiener process [46], i. e. a stochastic process δ -correlated in time and with zero mean:

$$\langle \mathcal{R}(t) \mathcal{R}(t + \Delta t) \rangle = \langle \mathcal{R}^2 \rangle \delta(\Delta t), \quad \langle \mathcal{R}(t) \rangle = 0$$

with $\delta(t)$ being the Dirac delta³.

Time integration of eqn. (2.2) leads to the following solution for the particle's velocity:

$$v_x(t) = v_x(0) e^{-\gamma t} + \int_0^t e^{-\gamma(t-\tilde{t})} \frac{\mathcal{R}(\tilde{t})}{m} d\tilde{t} \quad (2.3)$$

which in turn gives the following formula for the velocity time-correlation ($\langle \mathcal{R}(t) \rangle = 0$):

$$\begin{aligned} \langle v_x(t) v_x(t + \Delta t) \rangle &= v_x^2(0) e^{-\gamma(2t+\Delta t)} \\ &+ \left\langle \int_0^t e^{-\gamma(t-t_1)} \frac{\mathcal{R}(t_1)}{m} dt_1 \int_0^{t+\Delta t} e^{-\gamma(t+\Delta t-t_2)} \frac{\mathcal{R}(t_2)}{m} dt_2 \right\rangle \\ &= v_x^2(0) e^{-\gamma(2t+\Delta t)} \\ &+ \frac{1}{m^2} \int_0^t \int_0^{t+\Delta t} e^{-\gamma(2t+\Delta t-t_1-t_2)} \langle \mathcal{R}(t_1) \mathcal{R}(t_2) \rangle dt_1 dt_2 \end{aligned}$$

Given the aforementioned δ -correlation in time of \mathcal{R} , the latter integral returns:

$$\begin{aligned} &\int_0^t \int_0^{t+\Delta t} e^{-\gamma(2t+\Delta t-t_1-t_2)} \langle \mathcal{R}^2 \rangle \delta(t_1 - t_2) dt_1 dt_2 \\ &= \langle \mathcal{R}^2 \rangle \int_0^{\min(t, t+\Delta t)} e^{-\gamma(2t+\Delta t-2t_1)} dt_1 = \frac{\langle \mathcal{R}^2 \rangle}{2\gamma} \left[e^{-\gamma|\Delta t|} - e^{-\gamma(2t+\Delta t)} \right] \end{aligned}$$

² This will be the case for the Langevin equations proposed in Results Chapters 6 and 7, for the description of the amoeboid bio-hybrid system.

³ $\delta(t) \stackrel{\text{def}}{=} \lim_{\epsilon \rightarrow 0} I_\epsilon(t)$, with I_ϵ unit pulse in the interval $(-\epsilon, \epsilon)$.

where the first integration made use of the Mean Value theorem⁴. Therefore, one gets the following velocity time-correlation function:

$$\langle v_x(t) v_x(t + \Delta t) \rangle = v_x^2(0) e^{-\gamma(2t+\Delta t)} + \frac{\langle \mathcal{R}^2 \rangle}{2m^2\gamma} \left[e^{-\gamma|\Delta t|} - e^{-\gamma(2t+\Delta t)} \right] \quad (2.4)$$

that in the long time limit ($t \gg \gamma^{-1}$) becomes a simple exponential decay, independent from the initial condition $v_x(0)$:

$$t \gg \gamma^{-1} \implies \langle v_x(t) v_x(t + \Delta t) \rangle \simeq \frac{\langle \mathcal{R}^2 \rangle}{2m^2\gamma} e^{-\gamma|\Delta t|} \quad (2.5)$$

By setting $\Delta t = 0$, this last result allows to determine the (steady-state) mean square velocity of the particle:

$$\langle v_x^2 \rangle = \frac{\langle \mathcal{R}^2 \rangle}{2m^2\gamma} \quad (2.6)$$

which results to be strictly dependent, with a simple proportionality, to the mean square of the random force.

Let us now assume the system to be thermalized, i. e. in thermodynamic equilibrium with the environment. By virtue of the *Equipartition theorem*⁵, it must be:

$$\langle v_x^2 \rangle = \frac{k_B T}{m}$$

Consequently, eqn. (2.6) implies that:

$$\langle \mathcal{R}^2 \rangle = 2m\gamma k_B T = 2\eta k_B T \quad (2.7)$$

which is a simple form of the more general *Fluctuation-Dissipation theorem*, connecting the intensity of the random forces (fluctuations) with the dissipation coefficients (in this case η).

At this point, knowing the velocity time-correlation function, one can finally get information on the dynamics of particle displacement, by integrating in time once more. In fact, being by definition $x(t) - x(0) = \int_0^t d\tau v_x(\tau)$, one may write:

$$\langle (x(t) - x(0))^2 \rangle = \left\langle \int_0^t v_x(t_1) dt_1 \int_0^t v_x(t_2) dt_2 \right\rangle = \int_0^t \int_0^t \langle v_x(t_1) v_x(t_2) \rangle dt_1 dt_2$$

⁴ In general, for the scalar product between the Dirac delta δ and any function f one gets $\int_{\mathbb{R}} \delta(t) f(t) dt = \lim_{\epsilon \rightarrow 0} \int_{\mathbb{R}} I_{\epsilon}(t) f(t) dt = \lim_{\epsilon \rightarrow 0} \int_{-\epsilon}^{\epsilon} \frac{1}{2\epsilon} f(t) dt = f(0)$, where the last step is a direct consequence of the Mean Value theorem. This result goes under the name of *Sampling theorem* since δ acts on f as a sampling tool, returning the value of it in a specific point.

⁵ In (classical) statistical physics, the Equipartition theorem states that for a system in thermal equilibrium, all momenta p_j and all coordinates q_j contributing to its hamiltonian \mathcal{H} with additive quadratic terms, “store” each on average an equal amount of energy, corresponding to $\frac{1}{2}k_B T$. The demonstration is rather straightforward. In fact, if we consider for example any momentum p_j with an energy contribution $\alpha(q_i, p_{i \neq j}) p_j^2$, we can calculate the average value of the latter by weighing the associated microstates using the canonical distribution (valid if thermal equilibrium): $\langle \alpha p_j^2 \rangle = \frac{\int \alpha p_j^2 e^{-\mathcal{H}/(k_B T)} dq_i dp_i}{\int e^{-\mathcal{H}/(k_B T)} dq_i dp_i}$. By factorizing the Boltzmann terms of both numerator and denominator, and integrating first in p_j , one easily gets to the relation $\langle \alpha p_j^2 \rangle = \frac{k_B T}{2}$, as expected. The same reasoning can be extended to any other coordinate or momentum (as long as it enters quadratically in \mathcal{H}).

Now, using eqn. (2.4) and noticing that:

$$\int_0^t \int_0^t e^{-\gamma(t_1+t_2)} dt_1 dt_2 = \left(\frac{1-e^{-\gamma t}}{\gamma} \right)^2$$

$$\int_0^t \int_0^t e^{-\gamma|t_1-t_2|} dt_1 dt_2 = 2 \int_0^t dt_1 \int_0^{t_1} e^{-\gamma(t_1-t_2)} dt_2 = \frac{2}{\gamma} \left(t - \frac{1-e^{-\gamma t}}{\gamma} \right)$$

one finally obtains:

$$\langle (x(t) - x(0))^2 \rangle = \left(v_x^2(0) - \frac{\langle \mathcal{R}^2 \rangle}{2m^2\gamma} \right) \frac{(1-e^{-\gamma t})^2}{\gamma^2} + \frac{\langle \mathcal{R}^2 \rangle}{m^2\gamma^2} \left(t - \frac{1-e^{-\gamma t}}{\gamma} \right)$$

Ultimately, one can make use of eqn. (2.7) and, by defining the *diffusion constant* \mathcal{D} as (*Einstein relation*):

$$\mathcal{D} \stackrel{\text{def}}{=} \frac{k_B T}{\eta} = \frac{k_B T}{m\gamma}, \quad (2.8)$$

the particle's *mean square displacement* dynamics, for one dimension, assumes the form:

$$\langle (x(t) - x(0))^2 \rangle = \left(\frac{v_x^2(0)}{\gamma^2} - \frac{\mathcal{D}}{\gamma} \right) (1-e^{-\gamma t})^2 + 2\mathcal{D}t - \frac{2\mathcal{D}}{\gamma} (1-e^{-\gamma t}) \quad (2.9)$$

In isotropic conditions, the three Langevin equations describing the particle dynamics along the three spatial dimensions are to be identical, which implies analogous solutions. Further, the Cartesian description of space (based on an orthogonal basis of such Euclidean space) translates into $\langle \vec{v}^2(t) \rangle = \langle v_x^2(t) + v_y^2(t) + v_z^2(t) \rangle = \langle v_x^2(t) \rangle + \langle v_y^2(t) \rangle + \langle v_z^2(t) \rangle$ and $\langle \vec{r}^2(t) \rangle = \langle x^2(t) + y^2(t) + z^2(t) \rangle = \langle x^2(t) \rangle + \langle y^2(t) \rangle + \langle z^2(t) \rangle$, namely, the independence of the different components for both position and momentum of the particle. Hence, for an isotropic three-dimensional Brownian motion one gets:

$$\langle (\vec{r}(t) - \vec{r}(0))^2 \rangle = \left(\frac{v^2(0)}{\gamma^2} - \frac{n\mathcal{D}}{\gamma} \right) (1-e^{-\gamma t})^2 + 2n\mathcal{D}t - \frac{2n\mathcal{D}}{\gamma} (1-e^{-\gamma t}) \quad (2.10)$$

where $n = 3$ is the dimensionality of the space, and $v^2(0) = v_x^2(0) + v_y^2(0) + v_z^2(0)$.

A fundamental result is drawn by looking at the limiting behaviours for the mean square displacement:

$$t \ll \gamma^{-1} \implies \langle (\vec{r}(t) - \vec{r}(0))^2 \rangle \simeq v^2(0) t^2$$

$$t \gg \gamma^{-1} \implies \langle (\vec{r}(t) - \vec{r}(0))^2 \rangle \simeq 2n\mathcal{D}t + \text{const.}$$

As it can be appreciated, in the long time regime ($t \gg \gamma^{-1}$) the mean square displacement grows linear in time, with rate dictated by the diffusion coefficient \mathcal{D} : this spreading dynamics is what it's called *diffusive dynamics*, or simply *Diffusion*. Differently, for short times the particle exhibits a ballistic dynamics⁶, quickly dying out as the time approaches γ^{-1} : in the short-time regime the particle is still reminiscent of its ballistic start (see eq. (2.3)); however, in a time comparable to γ^{-1} , the initial

⁶ For an object performing ballistic motion, i. e. moving with constant speed \vec{v} , the mean square displacement grows quadratically with time: $\langle (\vec{r}(t) - \vec{r}(0))^2 \rangle = \vec{v}^2 t^2$.

momentum of the particle gets randomized by effect of the random forces, leading to the long-time diffusive regime.

The process of randomization of the momentum of a random-moving object, or in other words, the loss of memory on its ballistic start, goes under the name of *relaxation*. The time scale over which it takes place is called *relaxation time*; in this specific case, it identifies with the time $\gamma^{-1} = \frac{m}{\eta}$, namely the Brownian (or hydrodynamic) relaxation time. Lastly it should be noticed, from eq. (2.5), that γ^{-1} is also the rate of the exponential decay for the long-time velocity time-correlation function, which highlights the Markovian nature of the Brownian motion.

2.2 DETERMINISTIC DESCRIPTION OF MASS TRANSPORT: FOKKER-PLANCK EQUATIONS

In the previous Section it has been shown that the integration of a Langevin equation, a *stochastic* differential equation describing a certain random motion, leads to a solution for the dynamics of average velocities and displacements. As shown for the case of Brownian motion, solutions of such equations can describe the whole dynamics of a random-moving entity, with a short-time regime, reminiscent of the initial conditions, evolving into a long-time regime in a time $\sim \gamma^{-1}$.

Yet, when the time scales of interest are larger than γ^{-1} , a solution just for the long-time dynamics is all that is needed. In this case, one may tackle the problem of random motion with a generally easier approach, by solving a *deterministic* differential equation for the probability density function $\rho(\vec{r}, t)$ of the particle position (distribution function), built as an equation of mass conservation, which goes under the name of *Fokker-Planck equation*.

Let's consider eqn. (2.1), again along one spatial dimension. As the particle is a microscopic entity, observed for $t \gg \gamma^{-1}$, one may neglect the inertial term $m \frac{d^2 \vec{r}}{dt^2} \ll \eta \frac{d \vec{r}}{dt}$, which leads to an overdamped (first-order) Langevin equation:

$$v_x = -\frac{1}{\eta} \frac{dU(x)}{dx} + \sqrt{2\mathcal{D}}\xi(t) \quad (2.11)$$

where $\xi(t) = \frac{\mathcal{R}(t)}{\sqrt{\langle \mathcal{R}^2 \rangle}}$ is the normalized random force, i. e. a stochastic process with unitary variance, and the force standard deviation $\sqrt{\langle \mathcal{R}^2 \rangle}$ has been written in the form $\eta\sqrt{2\mathcal{D}}$ in analogy with its expression for a Brownian process (eqn. (2.7), using eqn. (2.8)).

From eqn. (2.11), one gets the following equation for the local probability flow $j(x, t) dt$:

$$j(x, t) dt = \rho(x, t) v_x(x, t) dt = -\rho(x, t) \eta^{-1} \frac{dU(x)}{dx} dt + j_r(x, t) dt \quad (2.12)$$

where $j_r(x, t)$ represents the rate of probability flow caused by the stochastic process $\sqrt{2\mathcal{D}}\xi(t)$.

In order to determine the latter, let's momentarily discretize the space-time into the intervals Δx and Δt . One may look at the physical dimensions of the noise power, i. e. its variance $2\mathcal{D}$, to define such units of time and space, so to have:

$$\frac{(\Delta x)^2}{\Delta t} = 2\mathcal{D}$$

In this way, heuristically, the noise would causes all the probability $P(x, t) \simeq \rho(x, t)\Delta x$, present in $(x, x + \Delta x)$ at time t , to flow into neighbouring space intervals in a time Δt : as a matter of fact, according to what obtained in the previous Section, a diffusing particle would spread through a distance Δx in a time $\sim \Delta t = \frac{(\Delta x)^2}{2\mathcal{D}}$. Consequently, the probability flow $j_r(x, t) \Delta t$ between two neighbouring space intervals in a time Δt will result to be:

$$j_r(x, t) \Delta t \simeq l \rho(x - \Delta x, t) \Delta x - (1 - l) \rho(x, t) \Delta x$$

where $l \in [0, 1]$ is a parameter describing the asymmetry of the random force. It follows then:

$$j_r(x, t) \simeq \frac{\Delta x}{\Delta t} (l \rho(x - \Delta x, t) - (1 - l) \rho(x, t)) = \frac{2\mathcal{D}}{\Delta x} (l \rho(x - \Delta x, t) - (1 - l) \rho(x, t))$$

Assuming now a random force with no bias (i. e. zero mean, as for Brownian noise), it will be $l = 1/2$, and going back to the continuous representation of space-time ($\Delta x \rightarrow dx$, $\Delta t \rightarrow dt$) one ends up with the following constitutive law for the noise-driven flow rate $j_r(x, t)$ (*Fick's law*):

$$j_r(x, t) = -\mathcal{D} \frac{\partial \rho(x, t)}{\partial x} \quad (2.13)$$

Finally, using eqn. (2.13) into eqn. (2.12), one can write down the the local probability flow:

$$j(x, t) dt = -\left(\rho(x, t) \eta^{-1} \frac{dU(x)}{dx} + \mathcal{D} \frac{\partial \rho(x, t)}{\partial x} \right) dt$$

leading to the following Fokker-Planck equation:

$$\frac{\partial \rho(x, t)}{\partial t} = -\frac{\partial j(x, t)}{\partial x} = \frac{\partial}{\partial x} \left(\eta^{-1} \rho(x, t) \frac{dU(x)}{dx} + \mathcal{D} \frac{\partial \rho(x, t)}{\partial x} \right) \quad (2.14)$$

Analogous solution for all spatial dimensions leads to the following vectorial Fokker-Planck equation:

$$\frac{\partial \rho(\vec{r}, t)}{\partial t} = \nabla \cdot (\eta^{-1} \rho(\vec{r}, t) \nabla U(\vec{r}) + \mathcal{D} \nabla \rho(\vec{r}, t)) \quad (2.15)$$

where \mathcal{D} and η are scalar for isotropic conditions.

As an example, we can now use the Fokker-Planck equation (2.14) to solve the problem of the long-time spreading dynamics of a Brownian particle, in an easier way than what done in the previous Section. For the simple Brownian dynamics of eqn. (2.2), where no external field is taken into account, the Fokker-Planck equation (2.14) is reduced to:

$$\frac{\partial \rho(x, t)}{\partial t} = \mathcal{D} \frac{\partial^2 \rho(x, t)}{\partial x^2} \quad (2.16)$$

known as *diffusion equation*.

To solve eqn. (2.16), one can take advantage of the Fourier transform to rewrite such partial differential equation into an ordinary differential equation. In fact, derivation of

any function f with respect to a given variable x corresponds to a simple multiplication within the respective Fourier domain (variable k)⁷:

$$\int_{-\infty}^{\infty} \frac{d f(x, \dots)}{d x} e^{-i k x} d x = i k \int_{-\infty}^{\infty} f(x, \dots) e^{-i k x} d x$$

Thus, by Fourier transforming in space both members of eqn. (2.16), one gets:

$$\frac{\partial \tilde{\rho}(k, t)}{\partial t} = -\mathcal{D} k^2 \tilde{\rho}(k, t)$$

where the tilde denotes the Fourier transform. Integration in time leads to:

$$\tilde{\rho}(k, t) = \tilde{\rho}_0(k, 0) e^{-\mathcal{D} k^2 t}$$

with $\tilde{\rho}_0(k, 0)$ initial condition for the Fourier transform of the distribution ρ . The initial position of the particle can be idealized as a δ -distributed probability; this implies that $\tilde{\rho}_0$ must actually be k -independent too⁸, hence acting only as a normalization constant.

At this point, one can go back to the x -space by antitransforming with respect to k :

$$\rho(x, t) = \frac{\tilde{\rho}_0}{\sqrt{2\pi}} \int_{-\infty}^{\infty} e^{i k x - \mathcal{D} k^2 t} d k$$

The exponential can be rewritten in the form of a Gaussian, by noticing that:

$$-\mathcal{D} k^2 t + i k x = -\left(\sqrt{\mathcal{D} t} k - \frac{i x}{2\sqrt{\mathcal{D} t}} \right)^2 - \frac{x^2}{4\mathcal{D} t} = w^2 - \frac{x^2}{4\mathcal{D} t}$$

with $w(k) = \sqrt{\mathcal{D} t} k - \frac{i x}{2\sqrt{\mathcal{D} t}}$. Thus, being the integral of a Gaussian $\int_{-\infty}^{\infty} e^{-a x^2} d x = \sqrt{\frac{\pi}{a}}$ ⁹, one gets:

$$\rho(x, t) = \frac{\tilde{\rho}_0}{\sqrt{2\pi}} e^{-\frac{x^2}{4\mathcal{D} t}} \int_{-\infty}^{\infty} e^{-w^2} \frac{d w}{\sqrt{\mathcal{D} t}} = \frac{\tilde{\rho}_0}{\sqrt{2\mathcal{D} t}} e^{-\frac{x^2}{4\mathcal{D} t}}$$

and the requirement $1 = \int_{-\infty}^{\infty} \rho(x, 0) d x = \int_{-\infty}^{\infty} \rho(x, t) d x \forall t$ sets the normalization constant $\tilde{\rho}_0 = \frac{1}{\sqrt{2\pi}}$.

In conclusion, we end up with the following solution of the Fokker-Planck equation for Diffusion:

$$\rho(x, t) = \frac{1}{\sqrt{4\pi\mathcal{D} t}} e^{-\frac{x^2}{4\mathcal{D} t}} \quad (2.17)$$

which is a Gaussian distribution with a variance of $2\mathcal{D} t$, growing linear in time, in line with what obtained for the particle mean square displacement as long-time solution

⁷ The proof is immediate: it is sufficient to integrate by parts, and assume $\lim_{x \rightarrow \pm\infty} f(x, \dots) = 0$ which must be valid, for example, for functions existing in a Sobolev (or *finite-energy*) space, that is a reasonable requirement for functions with physical meaning or, as in this case, for distributions.

⁸ The Fourier transform of a Dirac delta is in fact a constant spectrum (*white noise*): $\int_{-\infty}^{\infty} \delta(x) e^{-i k x} d x = e^{-i k 0} = 1$, by virtue of the Mean Value theorem.

⁹ This is easy to prove: one can easily integrate the square of such integral in polar coordinates, namely $\left(\int_{-\infty}^{\infty} e^{-a x^2} d x \right)^2 = \int_{-\infty}^{\infty} \int_{-\infty}^{\infty} e^{-a(x^2+y^2)} d x d y = \int_0^{2\pi} d\theta \int_0^{\infty} r e^{-a(r^2)} d r = \frac{\pi}{a}$.

of the Langevin equation (previous Section). In homogeneous conditions, diffusion along different directions is independent, implying $\rho(\vec{r}, t) = \rho(x, t)\rho(y, t)\rho(z, t)$; if the process is isotropic, one ultimately gets the following n -dimensional solution for diffusion:

$$\rho(\vec{r}, t) = \frac{1}{(4\pi\mathcal{D}t)^{n/2}} e^{-\frac{r^2}{4\mathcal{D}t}} \quad (2.18)$$

with variance $\langle r^2 \rangle = \langle x^2 + y^2 + z^2 \rangle = \langle x^2 \rangle + \langle y^2 \rangle + \langle z^2 \rangle = 2n\mathcal{D}t$.

A major advantage of dealing with Fokker-Planck equations, rather than Langevin equations, lies in the capability of the former to describe in a *deterministic* fashion the *mass transport*, as it provides a deterministic solution for the dynamics of a distribution of particles. In fact, by definition of statistical probability, $\rho(\vec{r}, t)$ describes as well the local density for an ensemble of particles (as long as particle-particle interactions are negligible¹⁰); being the diffusion equation linear, one can then use the unit source solution (2.18) as convolution kernel and get the solution of any Cauchy problem.

2.3 BEYOND BROWNIAN DIFFUSION

Brownian motion is commonly recognised as prototypical random motion, this for reasons exceeding its relative simplicity. As a matter of fact, such minimal random process is representative of a wide variety of stochastic systems and phenomena, which may differ in their nature, yet share profound analogies in terms of behaviour and quantitative description. Particularly, by virtue of the *Central Limit Theorem* [25], many different processes are analogous to Brownian motion when observed at large time/spatial scales¹¹.

However, complex transport processes as the motion of out-of-equilibrium systems, or the mass transport through complex fluids, may deviate significantly from the typical dynamics of normal Brownian processes, e. g. exhibiting non-Markovian features or non-ergodicity. As a consequence, a non-linear growth of the mean square displacement may be observed, even in the long-time regime. Such a spreading process goes under the name of *anomalous diffusion*, and is spotted by writing the mean square displacement dynamics in the form of a power law $\langle r^2 \rangle \propto t^\alpha$, where α is the scaling exponent: a scaling exponent $\alpha \neq 1$ identifies an anomalous diffusion process. [98, 99]

Nonetheless, the study of any random motion lies its foundations on all those same theoretical tools, originally developed for the study of thermal agitation, particularly Langevin equations and Fokker-Planck equations, properly extended to take into account more sophisticated forms of randomness. In particular, active Brownian particle models make use of Langevin equations to describe the dynamics of active matter, as living cells, by including non-equilibrium fluctuations. [91, 134]

¹⁰ When particle-particle interactions are not negligible, the diffusion of a particle, called *self diffusion*, differs from the diffusion of a distribution of several particles, or *collective diffusion*, where the motion of each particle is influenced by the neighbouring ones, giving rise to a different spreading process.

¹¹ An example is the conformation of flexible macromolecules, as many proteins and other polymeric chains: by considering a macromolecule as a sequence of N independently oriented segments (Kuhn segments, i. e. segments longer than the *persistence length* of the molecule), its conformation would be conceptually analogous to the trajectory of a Brownian particle in discrete time. Consequently, for a long chain of independent segments ($N \gg 1$, true for a flexible polymer by definition), one easily gets to the diffusion equation as Fokker-Planck equation for the probability distribution of the chain's end-to-end distance, the latter describing a molecule's spatial extension as function of its length.

Part II

MATERIALS & METHODS

EXPERIMENTAL STRATEGIES AND PROTOCOLS

3.1 CELL CULTURING AND BIOLOGICAL SAMPLE PREPARATION

I made use of two different mutant strains of *Dictyostelium discoideum* cells for my experiments:

LIFEACT-MRFP AX2 This cell line, originated from the axenic *Dictyostelium discoideum* wild-type AX2 by genetic engineering, expresses a modified version of the F Actin-binding protein *Abp140* [132], which is linked to the fluorescent protein mRFP.

The fluorescent molecule will then accumulate along Actin filaments within the cell, labeling the cell's cortex and cytosolic cytoskeletal filaments.

LIME-MRFP MYOII-GFP AX2 This cell line, again a genetic engineered version of the axenic strain AX2, expresses a GFP-linked version of the *Myosin II* protein and a mRFP-linked F Actin-binding protein, in this case *LimE*.

Within such cells, while mRFP still labels filamentous Actin, an additional fluorophore (specifically GFP) colocalizes with the cytoskeletal motor protein Myosin II.

For the realization of new cultures, cells were harvested from spores, previously stored at -80°C in a freezer suited for long term storage of biological material (UNICRYO deep freezer -86°C , UNIEQUIP, Planegg, Germany). A volume of 100 μl of spore suspension was added into a tissue culture flask (TC Flask T75 Standard, SARSTEDT AG & Co. KG, Nümbrecht, Germany) containing 10 ml of nutrient medium (HL5 medium including glucose, FORMEDIUM Ltd., Norfolk, England).

Following germination (usually complete within 1-2 days from defrosting), cells grew adhered on the bottom surface of the flask, over an available growth area of 75 cm^2 ; to avoid confluency, cell flasks were subcultured into a new flask every 2 days via 1:20 dilution of the cell suspension from the previous flask, or 1:64 prior to weekends.

Cell cultures have been kept at 22°C , under penicillin and streptomycin antibiotics (CELLPURE® Pen/Strep-PreMix, CARL ROTH GMBH+Co. KG, Karlsruhe, Germany) (100 μl /10 ml_{HL5}) to preserve the axenic state of the culture; moreover, 5 μl /10 ml_{HL5} of the antibiotic G418 disulfate (G418 disulfate ultrapure, VWR INTERNATIONAL, LLC.) were added as selection agent, preventing the culture from losing functionality of the mutant gene for actin fluorescent labeling due to genetic drift.¹

In the case of the strain LimE-mRFP MyoII-GFP AX2, having an additional mutant gene for Myosin II labeling, a second selection agent was used, the antibiotic Blasticidin S (Blasticidin S (hydrochloride), CAYMAN CHEMICAL, Ann Arbor, Michigan, USA), in the amount of 10 μl /10 ml_{HL5} .

¹ To keep a genetically engineered cell line genetically stable, it is customary to insert the mutant gene together with a gene conferring resistance to a specific antibiotic (the selection agent): in this way, by keeping the culture under that antibiotic, only cells with an intact functional mutant gene will survive and thrive. In a nutshell, it is about limiting genetic drift by imposing artificial evolutionary pressure.

Cell cultures have been renewed every 4 weeks, to avoid accumulation of any other undesired mutation eventually arising, generation after generation, by genetic drift.

For the purposes of the experiments, a cell suspension was harvested from a flask, normally during the subculturing procedure, thus:

- **if** experiments on the cell-particle system:
 1. cell suspension was diluted, so to have a cell count of roughly $50 \times 10^3 \text{ ml}^{-1}$ at the expected time of the experiment (doubling time of roughly 8-12 h [14]);
 2. 2 ml of the new suspension were put into a culture dish suitable for fluorescence imaging (FluoroDish™ tissue culture dish with cover glass bottom - 35mm, 23mm well, WORLD PRECISION INSTRUMENTS, INC., Sarasota, Florida, USA).
- **elseif** microfluidics-based experiments:
 1. at most a few hours before the experiment, the cell suspension was diluted, so to have a cell count of roughly $25 \times 10^6 \text{ ml}^{-1}$;
 2. the new cell suspension is kept rocking until usage, to avoid cell sedimentation.

3.2 PARTICLES AND MICROFABRICATION PROTOCOLS

MICROPARTICLE SUSPENSIONS

As cargo model, I adopted polystyrene spherical microparticles (Polybead® Microspheres, POLYSCIENCES EUROPE GMBH, Hirschberg an der Bergstrasse, Germany).

The particles were distributed by the provider in an aqueous suspension with minimal surfactant, as stated in the data sheet with no further detail on the liquid phase. To assure a healthy cell behavior during experiments, purpose-made, biocompatible batches of particle suspensions have been systematically prepared, by washing particles in a given amount of mother solution and resuspending them in a corresponding volume of phosphate buffer:

1. a known amount of mother suspension is put into a conical-bottom centrifuge tube, thus centrifuged at 500 g RCF (Relative Centrifugal Force) for 3 minutes;
2. the supernatant is removed from the tube by pipetting, leaving the sediment only (solid phase i.e. particles);
3. an equal amount of Sørensen buffer is added, so to restore the original total volume in the tube (Sørensen buffer: in ddH₂O added $2 \text{ g l}^{-1} \text{ KH}_2\text{PO}_4$, $0.36 \text{ g l}^{-1} \text{ Na}_2\text{HPO}_4$, $50 \mu\text{l l}^{-1} \text{ 1M MgCl}_2$, $50 \mu\text{l l}^{-1} \text{ 1M CaCl}_2$; pH 6.0).

Three different diameters have been systematically investigated: 10 μm, 45 μm, 75 μm. The company provided all particle suspensions with a given solid fraction of 25 mg ml^{-1} rather than a given particle number density, the latter more relevant for the purposes of my experiments. I found the particle density of the 45 μm size mother suspension (roughly $5 \times 10^5 \text{ ml}^{-1}$, as estimated by me and double checked from

product data sheet) to be well suited for my uses; as a consequence, I adjusted batch suspensions particle density for the other two sizes by proper dilution/concentration so to match them all. Given the spherical shape, particle volume v scales with the cubic power of the diameter, thus:

$$\begin{cases} \frac{v_{10}}{v_{45}} \simeq 80^{-1} & \implies \text{batch suspension diluted 1:80} \\ \frac{v_{75}}{v_{45}} \simeq (5/3)^3 & \implies \text{batch suspension concentrated 5:1} \end{cases}$$

MICROFLUIDICS

The microfluidic device has been designed using the Computer Aided Design (CAD) software DipTrace (NOVARM Ltd.), according to the design concept depicted in section 5.1. The CAD file generated has subsequently been sent to a specialized company (COMPUGRAPHICS JENA GMBH, Jena, Germany) for the realization of the photolithographic mask, a glass substrate coated with an opaque film in to which a 1:1 scale reproduction of the microfluidic circuit geometry is etched (figure 3.1).

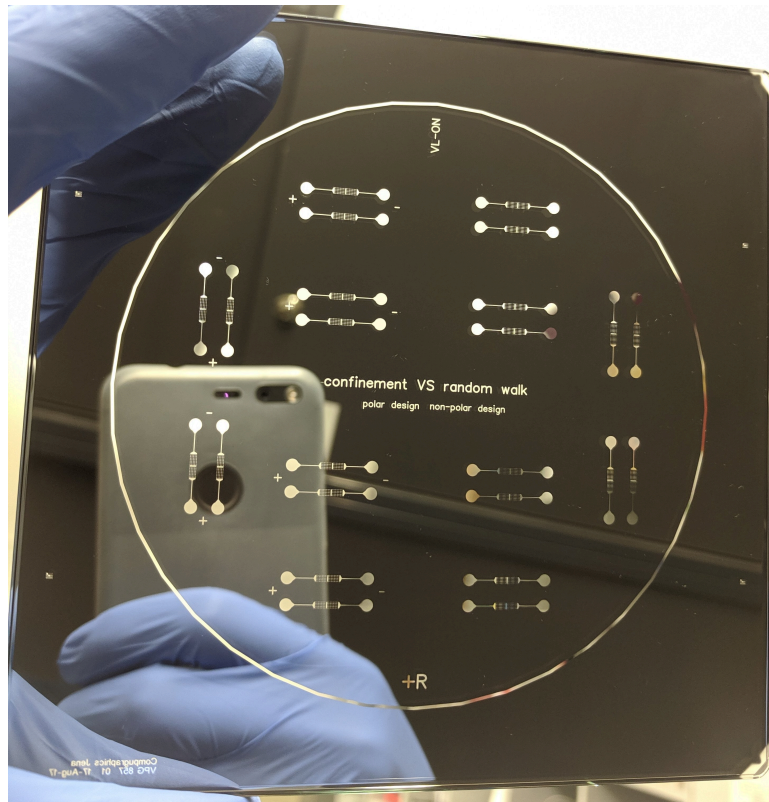


Figure 3.1: Picture of the photolithographic mask.

Based on such mask, microfluidic devices were produced by means of a soft-lithography prototyping strategy, first introduced in [45].

The first step consists in realizing a master wafer by lithography:

1. a silicon wafer (SILICON MATERIALS, Kaufering, Germany) is heated up to 200 °C for 20 min, to remove surface organic impurities by thermally-induced desorption;

2. the wafer is coated with a 10 μm -thick layer of epoxy-based negative photoresist (SU-8 2010, KAYAKU ADVANCED MATERIALS INC., Westborough, USA), using a vacuum spin coater (WS-400B-6NPP/Lite, LAURELL TECHNOLOGIES CORPORATION, North Wales, USA) (15 s at 500 RPM, followed by 45 s at 3500 RPM);
3. the newly coated wafer is kept at 65 °C for 3 min, to promote stress relaxation of the coating layer;
4. if air bubbles present in the resist layer, they were opened with a needle and the procedure steps back to the previous step;
5. the coated wafer is kept in an oven at 95 °C for 17 min (pre-exposure baking);
6. after a cool-down time of 10 min, the photolithographic mask is put on top of the coated surface of the wafer;
7. the coated surface is exposed, through the mask pattern, to UV radiation with a Hg–Xe arc lamp (model 2130-CP, RADIATION POWER SYSTEMS, INC.) (power 120 mW cm^{-2} , exposure time 1.6 s);
8. after removing the mask, the coated wafer is kept in an oven at 95 °C for 10 min to speed up the photoresist polymerization kinetics (post-exposure baking);
9. after a slow cool-down lasting 1 h, the coated surface is washed with the developer mr-Dev 600 (MICRO RESIST TECHNOLOGY GMBH, Berlin, Germany), so to wash away the unexposed, unpolymerized photoresist;
10. any developer residual possibly remaining on the wafer is washed away with isopropanol;
11. the newly micropatterned wafer is now undergone a final thermal cycle, in order to relax residual stresses in the polymerized photoresist:
 - a) wafer temperature is raised at a rate of 2 °C min^{-1} , up to 95 °C;
 - b) the wafer is kept at 95 °C for 10 min;
 - c) the wafer is cooled down to room temperature, with rate 2 °C min^{-1} .

Subsequently, the master wafer is used to mould a micropatterned slab of elastomeric polymer:

1. 60 g of polydimethylsiloxane (PDMS) are mixed with 6 g of its curing agent (Sylgard® 184, DOW CORNING, Midland, USA);
2. the master wafer is placed in a paper bowl, patterned face upwards, then the slowly curing yet fluid PDMS is poured on top;
3. the bowl is put in a desiccator and kept under vacuum conditions for 2 h, so to debubble the fluid PDMS (removal of air incorporated during mixing and pouring);
4. the bowl is put in a laboratory oven (THERMOFISCHER, Germany), set to gradually reach 75 °C, thus kept at such temperature for 2.5 h to speed up PDMS crosslinking kinetics;

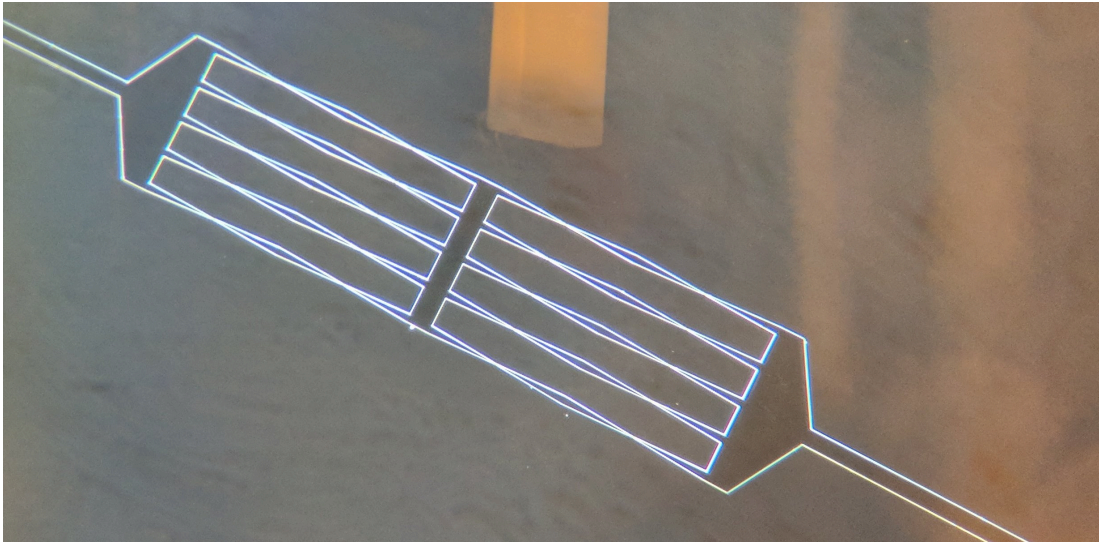


Figure 3.2: Close-up of a microstructure patterned on the master wafer.

5. the oven is gradually cooled down to room temperature, hence the bowl is pulled out.

At last, the microfluidic device is being assembled:

1. at most a few hours before the experiment, a part of the PDMS slab, containing a whole micropatterned circuit, is cut out of the bowl;
2. dust and photoresist residuals possibly present on the patterned surface are removed with tape;
3. the inlets/outlets of the microfluidic circuit are punched through the PDMS piece;
4. the PDMS piece is put into a plasma cleaner (PDC-002, HARRICK PLASMA, Ithaca, USA) together with a cover glass, taking care that the PDMS lies on its non-patterned surface;
5. the plasma cleaner is turned on for 2.5 min, during which the oxygen plasma being created interacts with the PDMS patterned surface and a cover glass surfaces, activating them;
6. immediately after, the patterned PDMS surface is stick on the cover glass exposed surface: the two activated surfaces covalently bind each other (Si–O–Si bridges), covering the micropattern hence creating a microscopic circuit of channels on the cover glass.

To avoid passivation of the surfaces within the device (the microchannels walls), the microfluidic circuit is immediately filled by capillary action with an aqueous liquid, thus kept wet until the time of experiment. Given the risk of pH/osmotic shock cells might experience in contact with pure water at the moment of injection, I chose phosphate buffer (the same used for particle suspension preparation) as filling liquid.

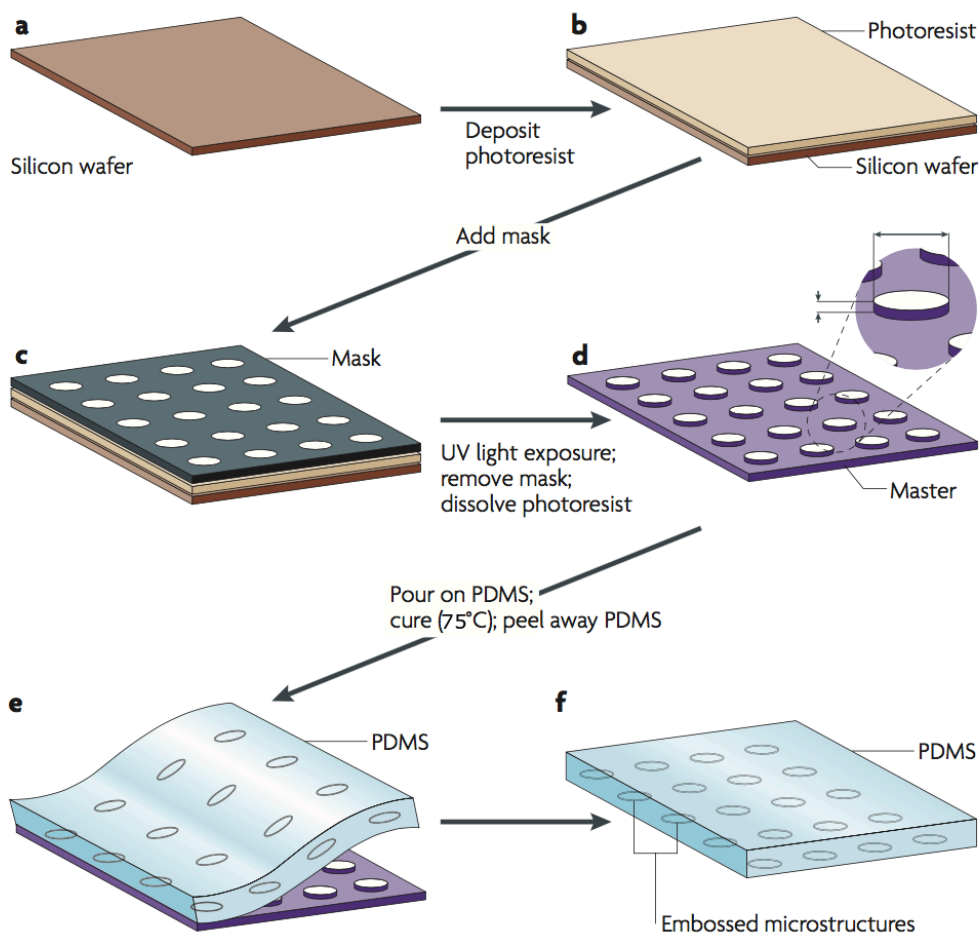


Figure 3.3: Schematics of master wafer realization and PDMS moulding. Modified from [165].

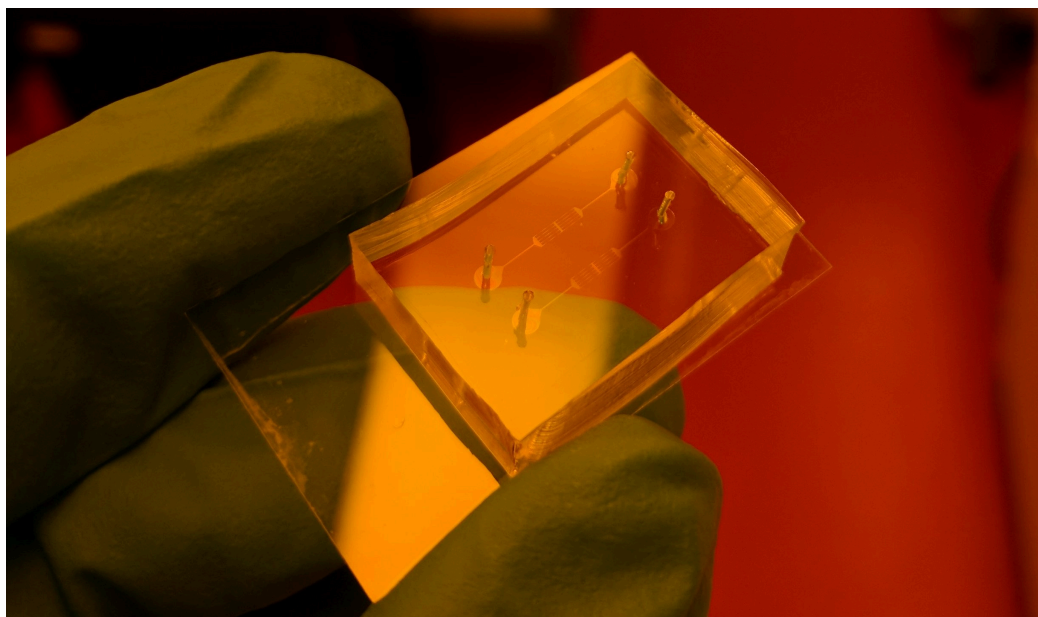


Figure 3.4: Picture of one newly assembled microfluidic chip.

3.3 OPTICS AND EXPERIMENTAL PROTOCOLS

The imaging setup, located on a vibration damping optical table, consisted in a Laser Scanning Microscope (LSM 780, ZEISS, Oberkochen, Germany): this microscope uses a scanning confocal optical path to create an image of the sample.

Such imaging strategy retains spatial resolution also along the optical axis (optical sectioning) thanks to an aperture, the detector pinhole, located on an optical plane which is a conjugated focal plane of the sample one (see figure 3.5): light coming from a specimen section different than the one in focus gets partially stopped by the pinhole, whose aperture size (or, more precisely, the interplay between it and the numerical aperture of the objective) determines the depth of field (resolution of such optical sectioning) [141].

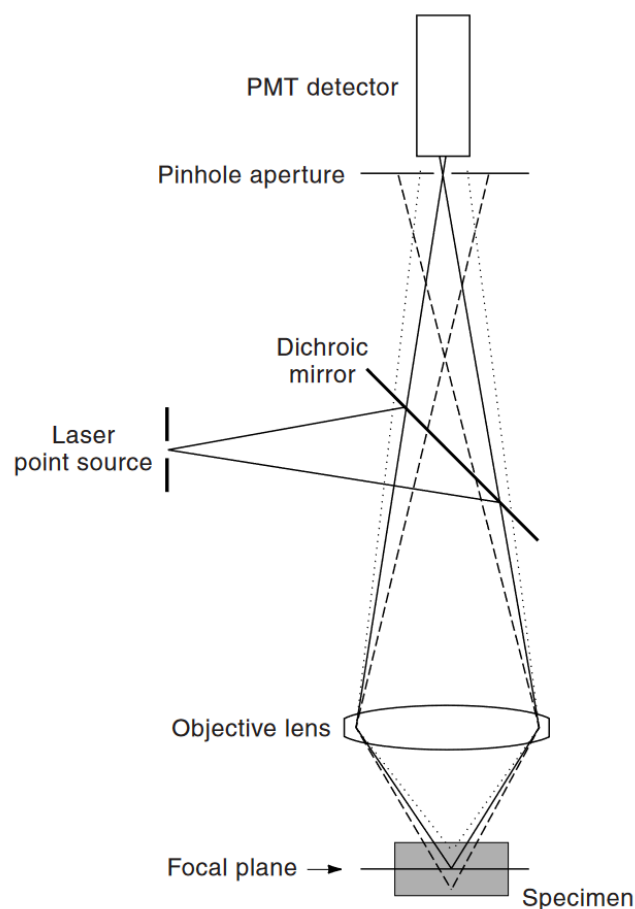


Figure 3.5: Schematic view of the optical path in a confocal microscope. From [106].

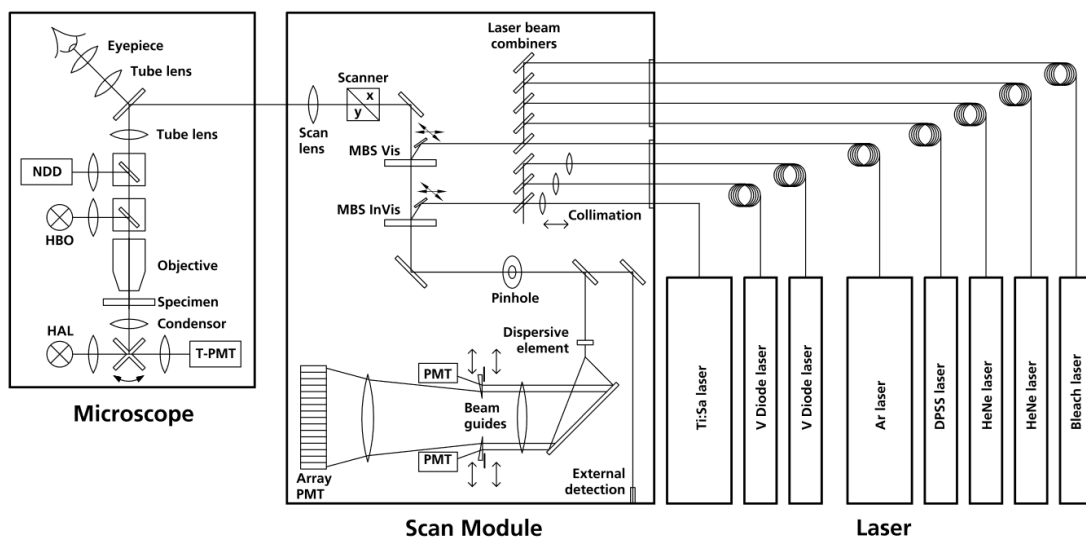
The microscope, being equipped with multiple laser sources, allowed for simultaneous imaging of the fluorescence-labeled cytoskeletal components as well as the particle via multimodal imaging:

CHANNEL I A diode-pumped solid-state laser (DPSS) generates electromagnetic radiation with $\lambda = 561 \text{ nm}$, which excites the fluorophore mRFP co-localizing with F-Actin; the fluorophore reacts by emitting lower energy non-coherent radiation, which is band-pass filtered and then detected by a photomultiplier.

CHANNEL II (only for LimE-mRFP MyoII-GFP AX2 cell line) An Argon-ion laser generates electromagnetic radiation with $\lambda = 488 \text{ nm}$ which excites the fluorophore GFP co-localizing with MyosinII; again, the fluorophore reacts by emitting lower energy non-coherent radiation, which is band-pass filtered and then detected by the same photomultiplier.

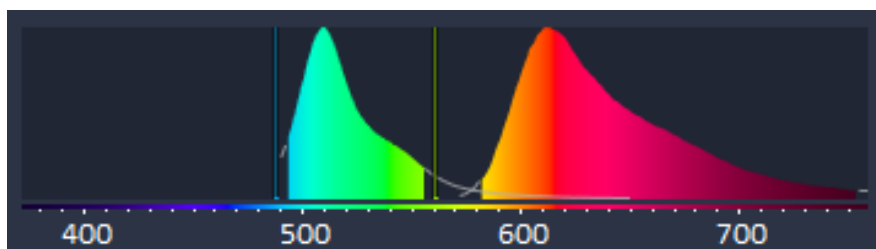
CHANNEL III All the transmitted light is collected by an additional part of the optical path, into a second photomultiplier; in this channel, an image arises from the contrast generated by refractive index discontinuities (much stronger for particles than cells).

The whole configuration of the imaging system, with its optical paths and light sources, can be seen in figure 3.6.



HAL Halogen Lamp
 HBO Mercury Vapor Short-Arc Lamp
 MBS Main Beam Splitter
 NDD Non-Descanned Detector
 PMT Photomultiplier
 T-PMT Transmission-Photomultiplier

(a)



(b)

Figure 3.6: (a) Optical Diagram of the LSM 780. From ZEISS operating manual. (b) Visualization of the excitation spectral line and the (detected) spectrum of fluorescence emission for the two fluorophores used. On horizontal axis, the wavelength λ in nm.

The experimental procedure varies between cell-particle experiments and microfluidics experiments:

- **if cell-particle experiments:**
 1. in the previously prepared culture dish (see section 3.1), 50 μl of purpose-made particle suspension (see section 3.2) are added;
 2. the microscope is being set up (objective and zoom, digital resolution, pixel dwell time, lasers);
 3. the sample is located in position along the optical path of the microscope, then the substrate (inner bottom surface of the dish) is brought into focus by observing the transmitted white light from an halogen lamp through the eyepiece;
 4. the position of the condenser along the optical path is adjusted to achieve an even exposure of the sample to the light from the halogen lamp (Köhler illumination²);
 5. by observing in transmitted white light through the eyepiece, and horizontally translating the field of view with the motorized stage of the LSM, a one cell-one particle system (far from other cells/particles) is found;
 6. the depth of field is reduced as much as possible by narrowing the detector pinhole, thus the focus is finely tuned to focus on the cell ventral surface;
 7. the focus is lifted by 0.3 μm ca., then the detector pinhole is widened to an aperture of 1 Airy Units, corresponding to roughly 0.7 μm of depth of field³;
 8. a time-lapse recording is being run, with frame rate within $(10 \text{ s})^{-1}$ and $(2 \text{ s})^{-1}$, until the system leaves the field of view or becomes unsuitable (cell division, other cells/particles alter the configuration of the system), for a maximum time of 1 h;
 9. the procedure is reiterated from point 5, to possibly observe many systems in the sample.

- **elseif microfluidics experiments:**
 1. a precision syringe (GASTIGHT® 1750, HAMILTON, Bonaduz, Switzerland) is filled with the cell suspension (prepared as discussed in section 3.1);
 2. a plastic tubing is fitted on the syringe needle, then filled with cell suspension;
 3. the syringe-connected plastic tubing is fitted into the inlet of the microfluidic chip, thus the cell suspension is injected slowly by hand, in the amount of 50 μl ca., so to bring some cells into the circuit by advection;
 4. the protocol proceeds as from point 2 of cell-particle experimental protocol, except for searching cells near the microchannels constrictions rather than cell-particle systems.

² It does so by using as an effective source not the lamp filament, but the intensity it generates on a conjugate Fourier plane. See for example [106]

³ By doing so, a bottom section 0.7 μm thick of the cell-particle system is imaged: cell ventral surface is visible together with a section of the particle

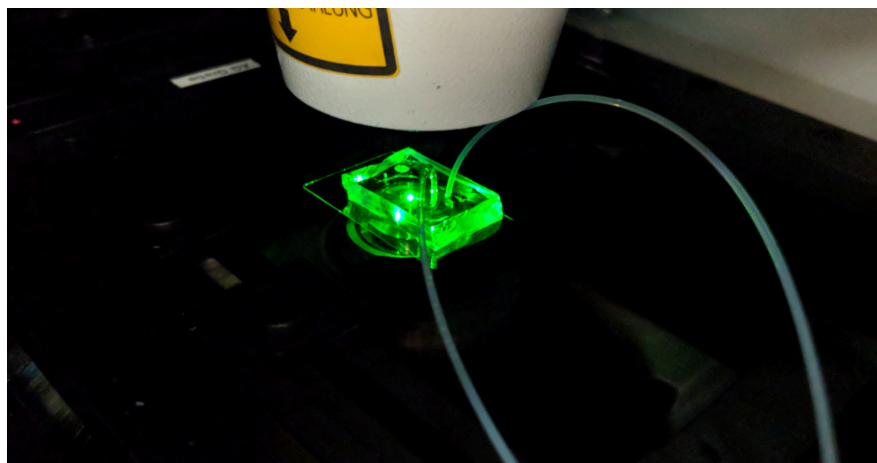


Figure 3.7: View of the microfluidic chip, filled and located in the experimental setup. It is possible to visualize some of the 561 nm electromagnetic radiation from the DPSS laser, scattered away from the optical path by the device.

4.1 IMAGE PROCESSING

All of the algorithmic strategies discussed in this section have been implemented in the form of MATLAB (MathWorks® Inc.) custom code.

SEGMENTATION

Cell segmentation relies on the 561 nm-source fluorescence channel (channel 1, see Section 3.3), exploiting the contrast created by the fluorescence emission from the mRFP labeling the F-actin. Particle segmentation is otherwise based on brightfield images (channel 3, see Section 3.3), where contrast is generated by refractive index discontinuities. Both objects are anyhow detected with akin algorithms, the only main difference being that, in the case of particles, the algorithm runs over the complement of the original images.

In order to separate the image pixels into two classes (pixels belonging to objects/regions of interest, pixels belonging to the background), on the basis of contrast-encoded information, a simple and fairly common strategy called *thresholding* relies on the image histogram to determine an intensity threshold, which then allows binary classification of the pixels based on their intensity values: “low intensity” pixels will be treated as logical zeros, “high intensity” pixels as logical ones¹ [88].

On the search of optimal threshold values, a well-known and established algorithm has been proposed in 1979 by Nobuyuki Otsu [111]. Otsu’s approach consists in finding the intensity value T that divides the histogram in two classes while maximizing a certain measure of class separability, i.e. inter-class variance

$$\sigma_{\text{inter}}^2 = \omega_0(\mu_0 - \mu)^2 + \omega_1(\mu_1 - \mu)^2$$

where (n_i pixel count for intensity i , $N = \sum_{i=1}^I n_i$ total pixel count)

$$\begin{aligned} \omega_0(T) &= N^{-1} \sum_{i=1}^T n_i = \text{Prob}[0|T], & \mu_0(T) &= \sum_{i=1}^T i \frac{n_i}{N \omega_0(T)} = \sum_{i=1}^T i \text{Prob}[i|0], \\ \omega_1(T) &= N^{-1} \sum_{i=T+1}^I n_i = \text{Prob}[1|T], & \mu_1(T) &= \sum_{i=T+1}^I i \frac{n_i}{N \omega_1(T)} = \sum_{i=T+1}^I i \text{Prob}[i|1], \end{aligned}$$

which means separating into two dissimilar, very distinct classes grouping together relatively similar pixels². Such optimization problem is solved iteratively, by cycling over each possible threshold value and calculating the corresponding inter-class

- 1 Thresholding belongs to the family of similarity-based segmentation techniques: pixels are grouped based on how “similar” they look with respect to some property, e.g. intensity [60].
- 2 In fact, it can be shown that maximizing class separability (inter-class variance) is equivalent to minimizing the (weighted average) intra-class variance $\sigma_{\text{intra}}^2 = \omega_0 \sigma_0^2 + \omega_1 \sigma_1^2$, i.e. maximizing intra-class similarity [57, 111].

variance, while storing in a variable the one that returned up-to-then maximum variance.

As one can guess from such description, Otsu's method performs best for images with bimodal distribution of intensities, featuring histograms with a deep and sharp valley between two peaks. As a matter of fact, it has been extensively shown how the performance of global thresholding techniques as Otsu's method are limited by factors adverse to bimodality, e.g. small object size, small mean difference between foreground and background pixels, large variances of the pixels belonging to the object and the ones of the background, large amount of noise [88].

Such adverse factors markedly occur in live cell imaging. Being the cell essentially a complex active hydrogel, its refractive index is close to the one of water and consequently creates little and inhomogeneous contrast over the projected cell area (more scattering from organelles/macromolecular assemblies). In case of live fluorescence imaging, laser sources need to work at low intensities in order to avoid fluorophore photobleaching [160] or, even worse, sample overheating; as a consequence, fluorescence emission may show as a weak signal, inhomogeneous and with poor Signal-to-Noise ratio (eventual medium self-fluorescence as contributing factor).

Figure 4.1 shows the look and features of a typical frame from my recordings.

Its histogram displays a single prominent peak quickly decaying into a short tail, representing a dominant noisy background merging with not-so-dissimilar meaningful intensities, and highlighting a poor use of the full scale dynamics.

In order to successfully apply Otsu's method for segmentation, I developed an algorithm that, by means of noise reduction and non-affine histogram transformation, increases object-background difference in intensity (intuitively, moving their distributions further apart) and leads to a quasi-binarized bimodal image.

An initial step consists in removing eventual high-frequency noise (commonly referred to as *salt-and-pepper* noise), as illustrated in figure 4.2. Here I opted for a median filter, since it tends to eliminate impulsive noise rather than spreading it over the surroundings, while retaining sharp object edges [39].

Subsequently, a first histogram transformation improves full scale dynamics usage by means of a one-sided saturation (so to say, like "zooming" on the interesting part of the histogram), followed by a second, non-linear transformation featuring two-sided saturation.

Figure 4.3 gives a visual understanding of the process. Optimal values for saturation thresholds of these two transformations depend on fluorescence intensity, noise features and in general on experimental settings, thus are given as input parameters by the user³.

The effect of such procedure on the image can be appreciated in figure 4.4. At this point, Otsu's thresholding is able to robustly and consistently segment live cell images. However, because of their intrinsic nature, fluorescent labels tagging specific cellular components may localize in certain regions within the cell, thus granting little to no contrast to the remaining part of the cell body. In this specific case, the

³ That is one main reason for the first transformation: in principle, one could directly perform the second transformation after noise reduction with same results; however, the performances of this step would be strongly sensitive to the exact values of the two saturation thresholds. Thanks to a preceding one-sided saturation, the overall histogram transformation results very robust, normally requiring at most an adjustment of the one first-transformation threshold only (so to say, how much to "zoom").

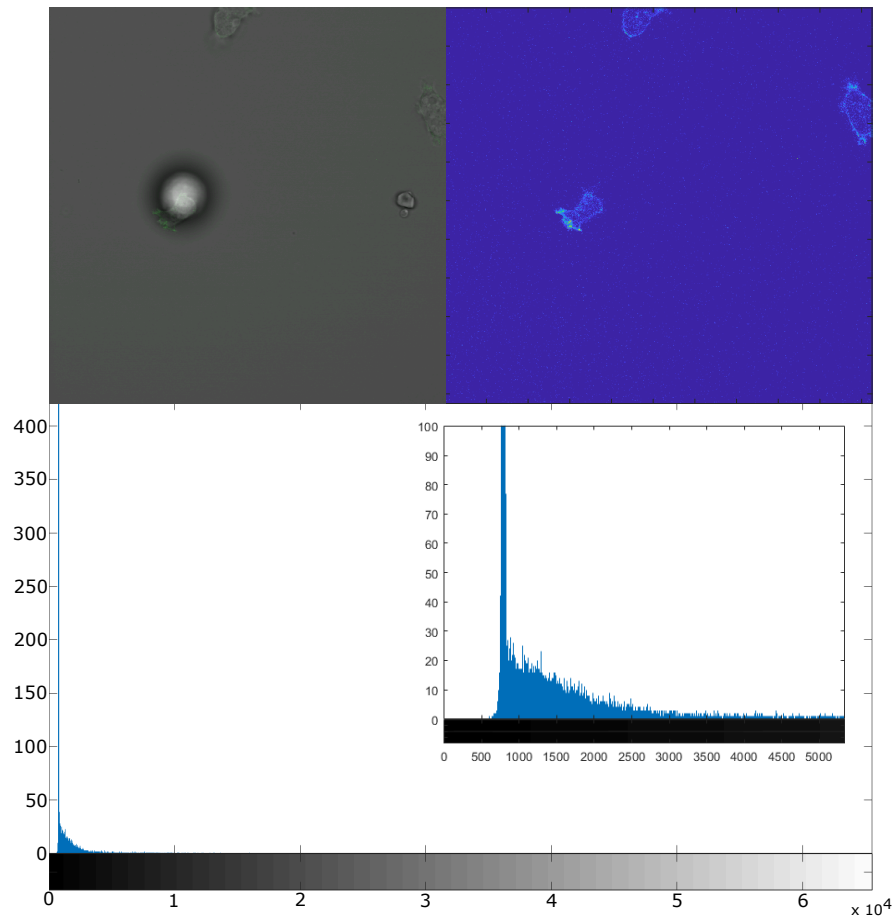


Figure 4.1: **top-left** Typical appearance of a frame from time-lapse recording of cellular trucks, using the optical setup described in Section 3.3. The imaging channel 3 (here in grey scale) allows particle visualization, while channel 1 (in green), barely visible, encodes for the distribution of the fluorescently labeled F-actin. **top-right** Colour-scale visualization of channel 1 from the same frame. **bottom** Histogram of intensities for the channel 1 frame shown above. Intensity is resolved with 16-bit precision; vertical axis refers to pixel count. To make the distribution visible, the sharp peak has been cut (it reaches counts in the order of 10^4); the insert shows a close-up on the peak decay.

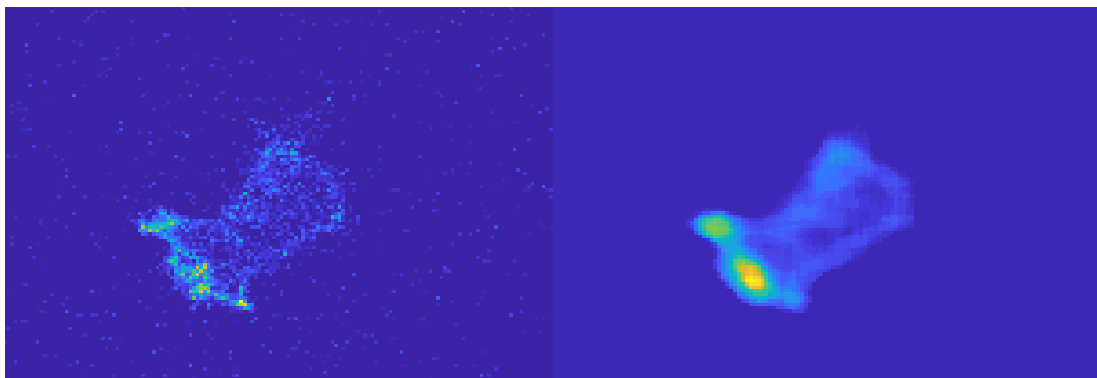


Figure 4.2: Close-up on a cell **left** *before* and **right** *after* median filtering (mask size $7\text{px} \times 7\text{px}$, $1\text{px} = 0.26\ \mu\text{m}$).

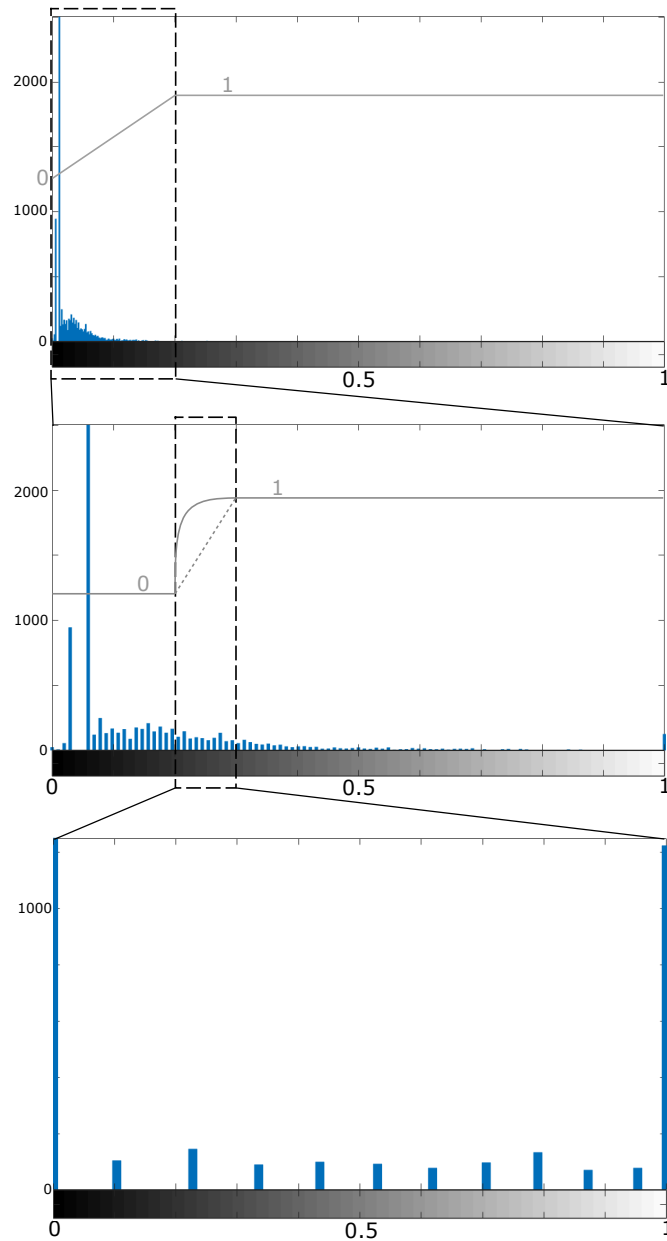


Figure 4.3: Schematic view on the two-step histogram transformation. The first transformation (**top to center**) “stretches” the peak while saturating higher intensities. The second one (**center to bottom**) performs a two-sided saturation, non-linearly remapping the pixel intensities in between the two thresholds to optimize contrast among intensities of interest. The non-linearity of the remapping function for the second step (grey line on central figure) has been overemphasized in figure. To make the distributions visible, the sharp peaks have been cut.

fluorescence signal used for segmentation mainly comes from filamentous-Actin rich regions, as growing cellular protrusions, Actin foci (dense regions of Actin cortex at substrate-adhering sites) and, to some extent, the cell cortex as a whole [23, 161]. As a consequence, after segmentation the detected regions may not fully cover the actual cell area: they typically display holes, or even show a disconnected topology (e.g. separated regions corresponding to different actin structures within the cell).

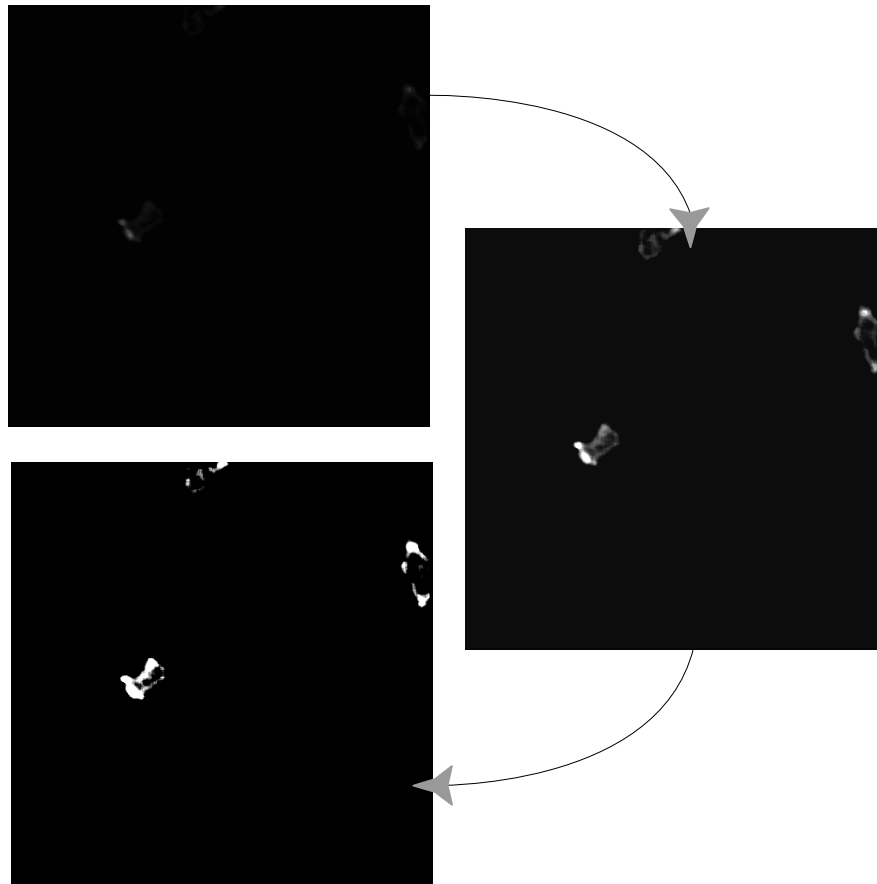


Figure 4.4: Glance view of the contrast enhancement occurring during the two-step histogram transformation.

Rather than drastically increasing sensitivity of the segmentation algorithm (not always enough, may also cause issues with noise and overall robustness), or introducing additional markers for cytosol labeling (rising experimental complexity and data size, with no real benefit on information content), I here lean on a solution based on morphological transformations of the segmented regions. Disconnected areas of a given cell merge into a whole after an operation of dilation, which basically adds a layer of white pixels (logical ones), with a given thickness in pixels, over all the detected perimeters; a subsequent operation of erosion performs the opposite task, removing a layer of equal thickness from the boundaries of the newly-formed merged region⁴ [150]. This two-step process is, so to say, hysteretic, and can merge separate parts of a cell area into a single relatively faithful cell shape. A final topological transformation reduces to zero the genus⁵ of the regions, filling the holes possibly remaining within detected objects. Figure 4.5 illustrates the outcome of these morphological operations⁶.

⁴ Algorithmically speaking, dilation/erosion is accomplished by substituting the value of each pixel in the image with the local maximum/minimum value, calculated among pixels within a sub-frame of size $(s * 2 + 1)px * (s * 2 + 1)px$ (s thickness of the layer of white pixels to be added/removed) centered on such pixel.

⁵ The genus, in topology, represents a generalization of the concept of hole [87].

⁶ Such sequence of morphological operations on detected areas makes the segmentation even more robust, less dependent on the exact saturation thresholds used.



Figure 4.5: Close-up on a binarized cell **left** before any morphological transformations, **center** after *dilation* and **right** after a *dilation-erosion* cycle followed by genus reduction.

In addition to the segmentation strategy discussed above, which can be classified as Region-based segmentation, I implemented an alternative algorithm for Edge-based segmentation: here binary classification, rather than based on pixels similarity, relies on the pixel property of discontinuity (with local surroundings) [60, 73].

Here my idea was to decode the meaningful information content (now considered to be the local intensity discontinuity) from the original image, and encode it in a new “fictitious” image in the form of intensity; hence, such artificial image can undergo segmentation analogously to what previously discussed, returning the object-enclosing boundaries for the real image. As measure of local discontinuity, I opted for the euclidean norm of the spatial gradient of intensity:

$$\begin{aligned}
 I_{\text{fictitious}}(i, j) &= \|\nabla I_{\text{real}}(i, j)\| \\
 &= (\nabla I_{\text{real}}, \nabla I_{\text{real}})_{L^2} \Big|_{i,j} = \left(\left(\begin{bmatrix} \partial_x \\ \partial_y \end{bmatrix} I_{\text{real}} \right)^T \cdot \begin{bmatrix} \partial_x \\ \partial_y \end{bmatrix} I_{\text{real}} \right)^{1/2} \Big|_{i,j} \\
 &= \sqrt{(\partial_x I_{\text{real}}|_{i,j})^2 + (\partial_y I_{\text{real}}|_{i,j})^2}
 \end{aligned}$$

where the partial derivatives are evaluated using a centred finite differences scheme. The resulting image is then smoothed via median filtering, normalized and thresholded. An example is shown in figure 4.6.

This approach is preferable for images where relevant information is encoded in the spatial distribution of intensity (discontinuities), rather than the actual pixel intensities, e.g. frames acquired by Phase Contrast or Differential Interference Contrast imaging. It is very versatile, performing well even with more “traditional” imagings as brightfield/fluorescence, though for the latter case not as performant as the previously described Region-based segmentation. As a matter of fact, it has been developed and used mainly for cooperations with other projects.

The full image-processing program allows selection between the two segmentation strategies via a switch in the main function.

TRACKING

The analysis of motion, and in general of any physical quantity’s temporal dynamics, of an object from a time-lapse imaging record requires its univocal identification through the frames it occurs. Practically, this means connecting all its segmented regions within different frames and assign to them the same “name”, or ID, without ambiguity. Establishing such connections, that is following the moving object through time frames, is what we call *tracking*.

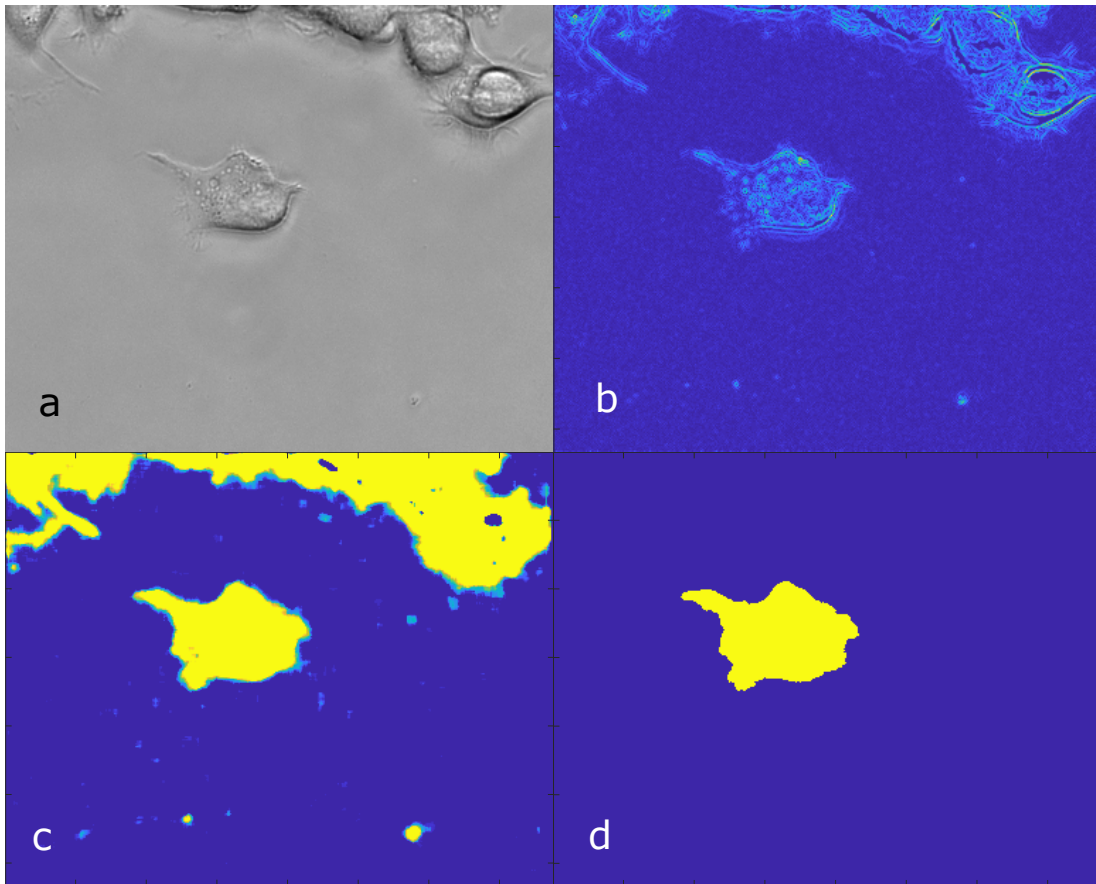


Figure 4.6: **a** Frame from a time-lapse recording of a mouse neuroblastoma cell (cell line N1E-115-1), performed by Annie Voigt via Differential Interference Contrast imaging. **b** Artificial image $I_{\text{fictitious}}$ created from image a. **c** Image $I_{\text{fictitious}}$ after median filtering and the previously described two-step contrast enhancement. **d** Image $I_{\text{fictitious}}$ after segmentation (objects too small, or in contact with image edges, have been automatically removed).

Albeit potentially challenging to address [17, 72], the tracking can be reduced to the simple observation of overlap between segmented regions of consecutive frames, as long as the time-sampling meets the condition

$$f_{\text{sampling}} > 2 \frac{\text{object max speed}}{\text{object size}} = \frac{v_{\text{max}}}{r_{\text{obj}}}$$

reminiscent of the Nyquist-Shannon criterion⁷.

To understand its meaning, let us imagine a worst-possible (tracking-wise) scenario, namely a tightly-packed collection of randomly-moving objects (here considered rigid, for sake of simplicity): if the maximum distance each object can run between two frames is less than half its length along the axis, then information on its identity can

⁷ The Nyquist-Shannon sampling theorem states that the information content of a band-limited continuous function (e.g. a finite-power, continuous-time signal) can be faithfully reconstructed from a series of samples, if its bandwidth (i.e. the maximum frequency in its spectrum) is less than half the sampling rate [142]; thus the sampling criterion $f_{\text{sampling}} > 2f_{\text{max}}$.

be retrieved by finding the one, in the previous frame, with whom it overlaps the most⁸.

In my case, given a peak cell speed of $\simeq 10 \mu\text{m min}^{-1} \sim 2r_{\text{cell}}\text{min}^{-1}$ (see Section 1.3), this translates in the condition $f_{\text{sampling}} > (30 \text{ s})^{-1}$, abundantly satisfied in my recordings (frame rate always within $(10 \text{ s})^{-1}$ and $(2 \text{ s})^{-1}$, as stated in Section 3.3). As a matter of fact, for a sparse distribution of objects as the cells in my experiments, each region would allegedly overlap with its previous occurrence only; having some inter-frame same-object overlap is then sufficient, granted by the less strict condition $f_{\text{sampling}} > (\text{object max speed})(\text{object size})^{-1} \sim 1 \text{ min}^{-1}$.

On the basis of the aforementioned arguments, I performed overlap-based tracking with the following algorithmic strategy.

A preliminary step consists in assigning, for every frame, a label to each segmented region, which is used to refer to a specific region within a frame. For each binarized frame I_{logic} , a labeled copy I_{label} is saved where, while the background pixels still assume value zero, pixels of different regions assume different integer values corresponding to the respective region labels.

Consequently, a first step of tracking creates a data structure for each segmented object in the first frame ($t = 0$), intended to collect the whole variety of computed informations about the object through the frames; thus, assigns to each a unique ID number, stored in the structure together with the region properties (e.g. boundary points and centroid coordinates) in such frame and other metadata.

Starting from the second frame ($t = \Delta t$), a sequence of mathematical operations, cycled over all the frames, identifies the inter-frame region connectivities:

An overlap matrix is obtained via the logical operation

$$I_{\wedge}(t) = I_{\text{logic}}(t) \wedge I_{\text{logic}}(t - \Delta t)$$

This matrix is used to sample the labeled images (\circ Hadamard product)

$$I_{\wedge}^{\text{old}}(t) = I_{\wedge}(t) \circ I_{\text{label}}(t - \Delta t), \quad I_{\wedge}^{\text{new}}(t) = I_{\wedge}(t) \circ I_{\text{label}}(t)$$

At this point I can define an inter-frame connectivity tensor, representing the pixel-wise coupling between labels, by merging the two matrices into a third-order tensor

$$\left. \begin{array}{l} C_{i,j,1}^t = I_{\wedge_{i,j}}^{\text{old}}(t) \\ C_{i,j,2}^t = I_{\wedge_{i,j}}^{\text{new}}(t) \end{array} \right\} \implies C_{i,j}^t = \begin{bmatrix} \text{label}_{i,j}(t - \Delta t) \\ \text{label}_{i,j}(t) \end{bmatrix}$$

An inter-frame list of object-to-object connectivities is finally obtained by cycling over the elements $C_{i,j}^t$ and listing all the label couples without repetition.

At last, each object in the current frame gets identified as the one in the previous frame whose label is connected to, and its features are added to the same data structure.

Exceptions while tracking are treated as follows:

⁸ The analogy with the sampling of a 1-dimensional time signal (in the context of which the Nyquist-Shannon sampling theorem is commonly introduced) gets more clear by imagining a 1-dimensional version of such example, that is a line of object in close contact to each other, moving with a given speed towards the same direction along the line axis: following an object would be no different than "following" the peaks of harmonics making up a time signal.

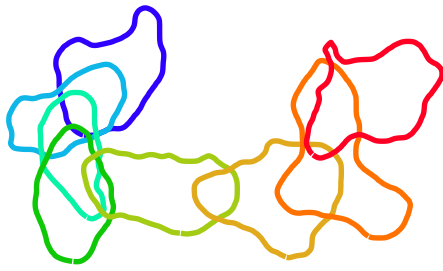


Figure 4.7: Accumulating plot of a cell's boundary, plotted every minute. The colour scale encodes time, from blue ($t = 0$) to red ($t = 7$ min), so to visualize cell shape and position evolving in time. The labeling of boundaries, detected through consecutive frames, as belonging to the same cell is executed by the tracking algorithm.

- Region with no connection to any in the previous frame (new object appearing): a new ID is created and a new data structure is initialized.
- Multiple regions are connected to a same one in the previous frame (e.g. cell division): all of them are treated as new objects (new IDs and data structures are created for each).
- A region connects to many previous ones (e.g. during cell contact with no possibility of distinguishing the single bodies): the region is treated as a new object and receives an ID and data structure.

After tracking, many informations on object motion (trajectory, estimated instantaneous speed) and shape dynamics (local boundary displacement) can be calculated by different functions and stored in the respective structure.

Regarding the centroid speed, its instantaneous value is estimated via a centred finite differences scheme over a smoothed version of the actual trajectory. In fact, sudden changes in cell shape (as well as rare-yet-possible segmentation noise) can reflect in abrupt displacements of the centroid, causing overshoot spikes of estimated velocity which can alter significantly even the average velocity. Low-pass filtering the real centroid track, with a moving average spanning a time frame comparable to the characteristic time for protrusion maturation ($\sim 1/2$ min [22]), solves the issue by returning speeds more faithful to actual cell displacement (cancels out overshoots without significant loss on random cell motion fine structure).

The algorithm for analysis of shape dynamics, instead, is a challenging issue on its own, and it is the focus of another PhD project within our research group.

BOUNDARY REFINEMENT

The rationale behind the segmentation protocol previously discussed focuses on consistent *detection* of objects, rather than high shape accuracy: although returning generally good boundaries, it sacrifices some sensitivity in favor of much needed detection robustness. This may make some difference in the data analysis outcome, particularly when morphological transformations had to be used intensively (setting a thick layer of pixels for dilation-erosion).

In order to address this weak point and obtain faithful cell shapes, I made use of *active contouring* [74] for refining the detected boundaries of cells (exclusively, no need of it for particles).

In an active contouring method, the boundary of an object is treated as an elastic 1-dimensional body, representing a closed deformable curve lying on the image

$I_{\text{image}}(x, y)$ and referred to as *snake*. A snake $\vec{\sigma}$, starting from a given shape, would deform under the effect of a force field $\vec{f}(x, y)$ stemming from the image, converging to a shape that minimizes its energy functional, i.e. (Lagrange's notation for differentiation)

$$E = \int_0^1 \left(\frac{1}{2} (\alpha \|\vec{\sigma}'(s)\|^2 + \beta \|\vec{\sigma}''(s)\|^2) + E_{\text{image}}(\vec{\sigma}(s)) \right) ds \quad (4.1)$$

where: s is the snake's curvilinear coordinate; the terms $1/2 \alpha \|\vec{\sigma}'(s)\|^2$ and $1/2 \beta \|\vec{\sigma}''(s)\|^2$ (α and β being axial and bending rigidities) represent respectively the tensile and bending elastic energies, as derived in the context of continuum mechanics [65, 93]; $E_{\text{image}}(\vec{\sigma}(s))$ is the so-called image functional [74], an external energy contribution associated to the force field, calculated from the image to be minimal near features of interest (e.g. edges).

The mathematical problem of functional optimization is addressed by the variational calculus, which shows, among other things, that optimizing a functional of the type $\int_{\Delta\tau} \mathcal{L}(\tau, q(\tau), q'(\tau), \dots, q^{(n)}(\tau)) d\tau$ is equivalent to finding the solution $q(\tau)$ of an associated Euler-Lagrange equation⁹ [53]:

$$\sum_{k=0}^n (-1)^k \frac{d^k}{d\tau^k} \left(\frac{\partial \mathcal{L}}{\partial q^{(k)}} \right) = 0$$

Applied to the snake's energy functional (4.1), this theorem leads to the equation ($\nabla E_{\text{image}} \stackrel{\text{def}}{=} -\vec{f}$ ¹⁰)

$$\alpha \vec{\sigma}''(s) - \beta \vec{\sigma}''''(s) + \vec{f} = 0 \quad (4.2)$$

[74], which has the form of a force balance. Accordingly, one can write down an equation of motion for the snake:

$$\partial_t \vec{\sigma}(s, t) = \alpha \partial_s^2 \vec{\sigma}(s, t) - \beta \partial_s^4 \vec{\sigma}(s, t) + \vec{f} \quad (4.3)$$

The solution $\vec{\sigma}$ minimizing the energy can thus be found by numerically integrating eq. (4.3), i.e. iteratively solving its discretized counterpart over time steps, until the snake stabilizes [74].

The potential of snakes in shaping into object boundaries within an image relies on the choice of a proper force field \vec{f} , able to attract and deform the snake so to conform it to the object shape.

In literature there can be found several force field formulations, usually conservative fields defined as $\vec{f} \stackrel{\text{def}}{=} -\nabla E_{\text{image}}$, with the image functional treated as a potential for the force field. Among more sophisticated ones, the Gradient Vector Flow (GVF) field [170] has been previously used by my research group in similar contexts, with positive

⁹ In the context of analytical mechanics, for example, the principle of stationary action translates into an analogous optimization problem for the time integral of the Lagrangian function, leading to an alternative formulation of Newton's classical mechanics (so-called Lagrangian mechanics).

¹⁰ This is not always the case, since non-conservative fields may as well be used [126]. For a field \vec{f} with a solenoidal component, one can still adopt a force balance as in eq. (4.2), although this will not be identical to minimizing the energy functional (4.1) since the image functional E_{image} can only encode, by definition, the irrotational part of the force field [103].

outcomes. In this formulation, $\vec{f}(x, y) = [f_x(x, y) \quad f_y(x, y)]$ is defined as the vector field minimizing the functional¹¹

$$\epsilon = \int \int \mu (\|\nabla f_x\|^2 + \|\nabla f_y\|^2) + \|\nabla E_{\text{image}}\|^2 \|\vec{f} - (-\nabla E_{\text{image}})\|^2 dx dy$$

with the image functional defined as $E_{\text{image}}(x, y) = -\|\nabla I_{\text{image}}(x, y)\|^2$. I opted for such force field, making use of the algorithm for GVF force developed by Chenyang Xu and Jerry L. Prince (to whose article please refer for further details) [170].

For each detected object in a given frame, a local GVF field is calculated and a snake, initialized with the object shape as detected from segmentation, is let to evolve in it according to eq. (4.3). Eventually, the approximate boundaries from the segmentation procedure finely adjust to a tight match of the cell perimeter. An example of such procedure is shown in figure 4.8.

4.2 ANALYSIS OF CELL-CARGO DYNAMICS AND INTERACTION

All of the algorithmic strategies discussed in this section have been implemented in the form of MATLAB (MathWorks® Inc.) custom code.

RELATIVE DYNAMICS

Evidence on distinct dynamical patterns of particle displacement over the cell body, seemingly correlated with the dynamics of cell cytoskeletal machinery (see Section 5.1), has been the main drive leading towards an in-depth analysis of the cell-cargo relative motion.

In order to focus on the relative motion between the carrier (cell) and cargo (particle), often hard to discern from the convoluted overall motion of the two bodies, plots have been made for the visualization of cell (centroid) trajectory in a relative frame of reference, firm with the particle centroid. Specifically, the time-evolution of the 2-dimensional variable

$$\vec{r}_{\text{rel}}(t) = -l_0 \vec{\Delta}(t) \stackrel{\text{def}}{=} -[\vec{R}(t) - \vec{r}(t)] \quad \vec{R}(t) = \begin{bmatrix} x_{\text{pcl}}(t) \\ y_{\text{pcl}}(t) \end{bmatrix}; \quad \vec{r}(t) = \begin{bmatrix} x_{\text{cell}}(t) \\ y_{\text{cell}}(t) \end{bmatrix}$$

is displayed in the $x_{\text{rel}}-y_{\text{rel}}$ space, with color-encoded time so to grasp dynamics.

The choice of showing the cell relative motion with respect to the particle $\vec{r}_{\text{rel}}(t) = -l_0 \vec{\Delta}(t)$ rather than its opposite is, of course, purely arbitrary and irrelevant with regards to relative motion analysis: here, the preference is rooted into an instinctive tendency of looking at the motion of the one only active body involved. However, this same tendency lead to the choice of its counterpart $l_0 \vec{\Delta}(t) \stackrel{\text{def}}{=} \vec{R}(t) - \vec{r}(t)$ in the context of modeling (see Section 7.1), which is why \vec{r}_{rel} is here introduced with respect to it.

¹¹ From the GVF functional one can spot two distinct terms: $\|\nabla E_{\text{image}}\|^2 \|\vec{f} - (-\nabla E_{\text{image}})\|^2$ conforms the force field to the traditional $\vec{f} \stackrel{\text{def}}{=} -\nabla E_{\text{image}}$, in the vicinity of features of interest (where $\|\nabla E_{\text{image}}\|$ is high, i.e. edges); $\mu(\|\nabla f_x\|^2 + \|\nabla f_y\|^2)$ “diffuses” the perturbation on the field stemming from features (μ smoothing parameter), increasing their range of action. In fact, the associated Euler-Lagrange equation is a diffusion-reaction p.d.e. .

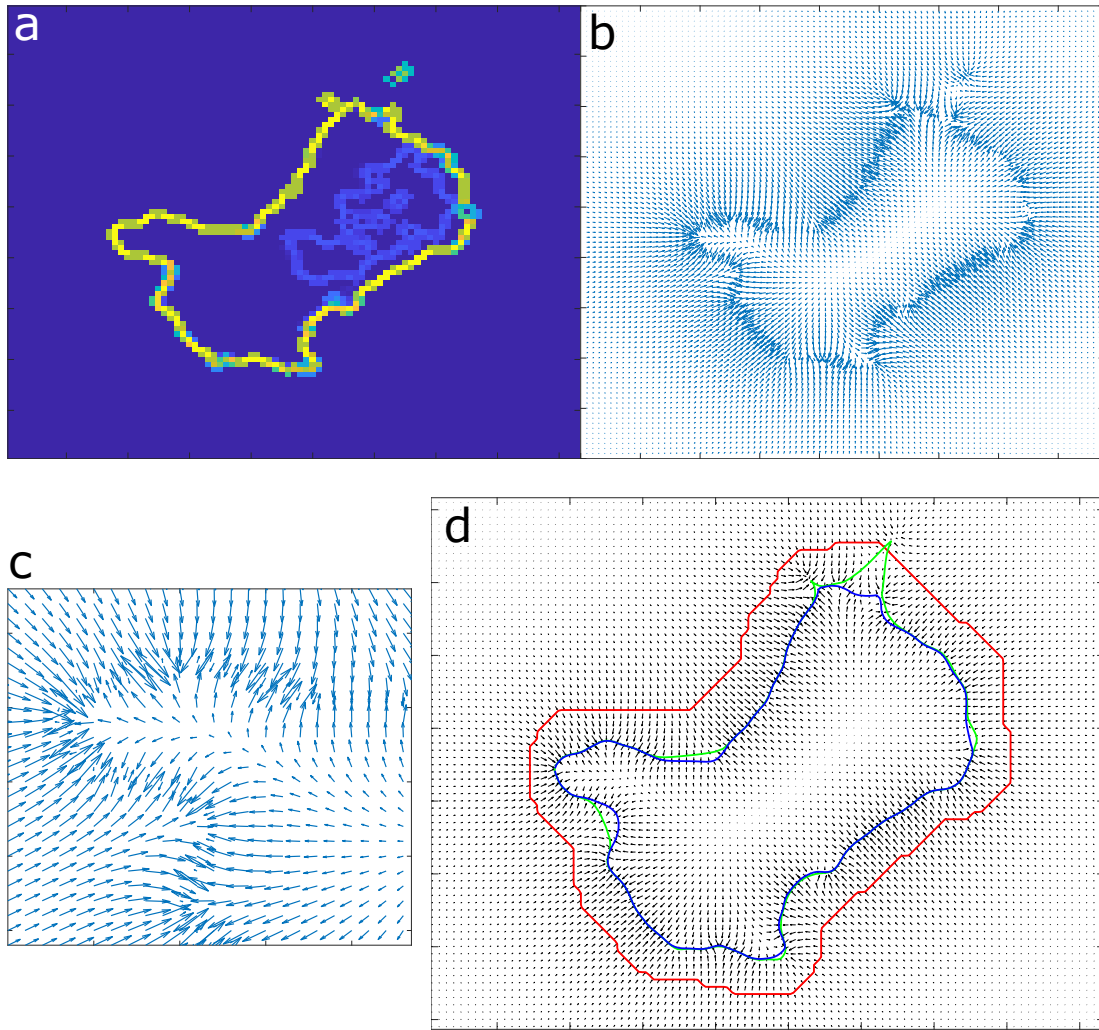


Figure 4.8: **a** Close-up on a cell, with colour scale encoding the absolute value of the image functional $|E_{\text{image}}(x, y)| = \|\nabla I_{\text{image}}(x, y)\|^2$. The image I_{image} underwent a fine-grain median filtering (impulsive noise removal) and contrast enhancement, prior to calculation of the image functional. **b** Vector map of the resulting GVF force field, with **c** showing a close-up on a protrusion. **d** Visualization of the process of mechanical deformation of a cell boundary, under the effect of the force field. From red to blue, the approximate boundary (in red, here on purpose overly inaccurate) gradually deforms (in green, intermediate state) to converge into a more accurate cell shape (blue).

The time-evolution of the relative (scalar) distance $\|\vec{R}(t) - \vec{r}(t)\| = \|\vec{r}_{\text{rel}}(t)\|$ is also being plotted, so to have a straightforward read of the intermittent behavior displayed by the system (see Section 5.1), without the additional information on orientation and rotational noise.

For an understanding of the type of dynamical process dictating such relative motion, and a possibly more thorough comparison among different cell-cargo systems, *Recurrence Plots* (RPs) have been generated from the time evolution of the cell relative position.

RPs graphically represent time correlation in a dynamical system by means of a matrix of self-similarity, calculated over a time series of a system's phase space¹² vector $\vec{x}(t)$: self-similarity of the system in two different time instants t_i and t_j is quantified by their distance in the phase space $I(t_i, t_j) = \|\vec{x}(t_j) - \vec{x}(t_i)\|$, usually with Euclidean metrics [47, 95]. Such approach for dynamical analysis is in fact powerful yet simple, overcoming some limitations of other more complex methods for dynamical parameters computation [47]; at the same time, conversely to a typical autocorrelation function¹³, it describes time correlation without requiring time averaging.

I applied this data analysis technique by defining the cell-cargo relative coordinates as phase space of the dynamical process, thus using the cell relative position \vec{r}_{rel} as phase-space vector. As a consequence, the normalized difference in relative position between two times $\|\vec{\Delta}(t_i) - \vec{\Delta}(t_j)\|$ measures for the index of similarity $I(t_i, t_j)$.

Recurrence plots have been used to analyse the relative scalar distance $\|\vec{r}_{\text{rel}}(t)\| = l_0 \|\vec{\Delta}(t)\|$ as well, mainly for comparing to the ones for its vectorial counterpart, so to grasp some additional knowledge on rotational noise and the reorientation process (see Section 5.2).

Figure 4.9 shows a summary of the relative dynamics analysis for a given cell-cargo system.

For the experimental estimation of rates of occurrence λ and time duration τ_{rev} of the reorientation process, detection of reorientation events was performed with two distinct strategies: thresholding the $\|\vec{r}_{\text{rel}}(t)\|$ time signal via Otsu's method (described, in the context of image segmentation, in Section 4.1); binarizing (again, by Otsu thresholding) the Recurrence Plot for $\|\vec{r}_{\text{rel}}(t)\|$, where such events appear as a distinct horizontal/vertical bands of sudden decorrelation. The two methods provided consistent event counts. Their time duration was measured over the thresholded time series, as the time spent under threshold for a given occurrence.

As sudden changes in cell shape can cause abrupt displacements of the cell centroid, relative distance time series may appear noisy, making difficult at times to distinguish reorientation events, as fluctuations near threshold may cause e. g. multiple crossings of the latter during a single reorientation. In order to reduce sudden, non reorientation-related fluctuations in relative distance, time series of $\|\vec{r}_{\text{rel}}(t)\|$ have been low-pass filtered prior to thresholding/RP-based count. Specifically, I employed a moving average, spanning a time frame comparable to the characteristic time for protrusion

¹² In the context of dynamical systems theory, a phase space is a normed vector space built upon the whole set of N variables describing a dynamical system: each physical variable acts as space coordinate, leading to an N -dimensional vector space in which all possible states of the system are represented. As a consequence, the state of a dynamical system is represented by a unique set of coordinate values, namely a point in the phase space, whose time-evolution depicts the system's dynamics. As an example, in analytical mechanics, the Hamiltonian formalism describes the motion of a body in an alternative $2n$ -dimensional phase space (n generalized coordinates, n associated momenta), which generalizes the Euclidean physical space by treating the associated momenta (here considered independent variables) as additional coordinates. [110, 153]

¹³ Broadly speaking, a (time) correlation function is a mathematical tool measuring statistical (time) correlation among variables of random/unknown processes. For a generic number N of variables $X_i(t)$, time correlation $C(X_1, \dots, X_N)$ is quantified by their covariance $\left\langle \prod_{i=1}^N (X_i(t) - \langle X_i \rangle_t) \right\rangle_t \equiv \left\langle \prod_{i=1}^N X_i(t) \right\rangle_t - \prod_{i=1}^N \langle X_i \rangle_t$, usually normalized by the product of their standard deviations. Particularly, when calculated between a signal $X_1 = X(t)$ and a delayed copy $X_2 = X(t - \delta)$, it defines the function $C(\delta)$ called *autocorrelation function*. [114]

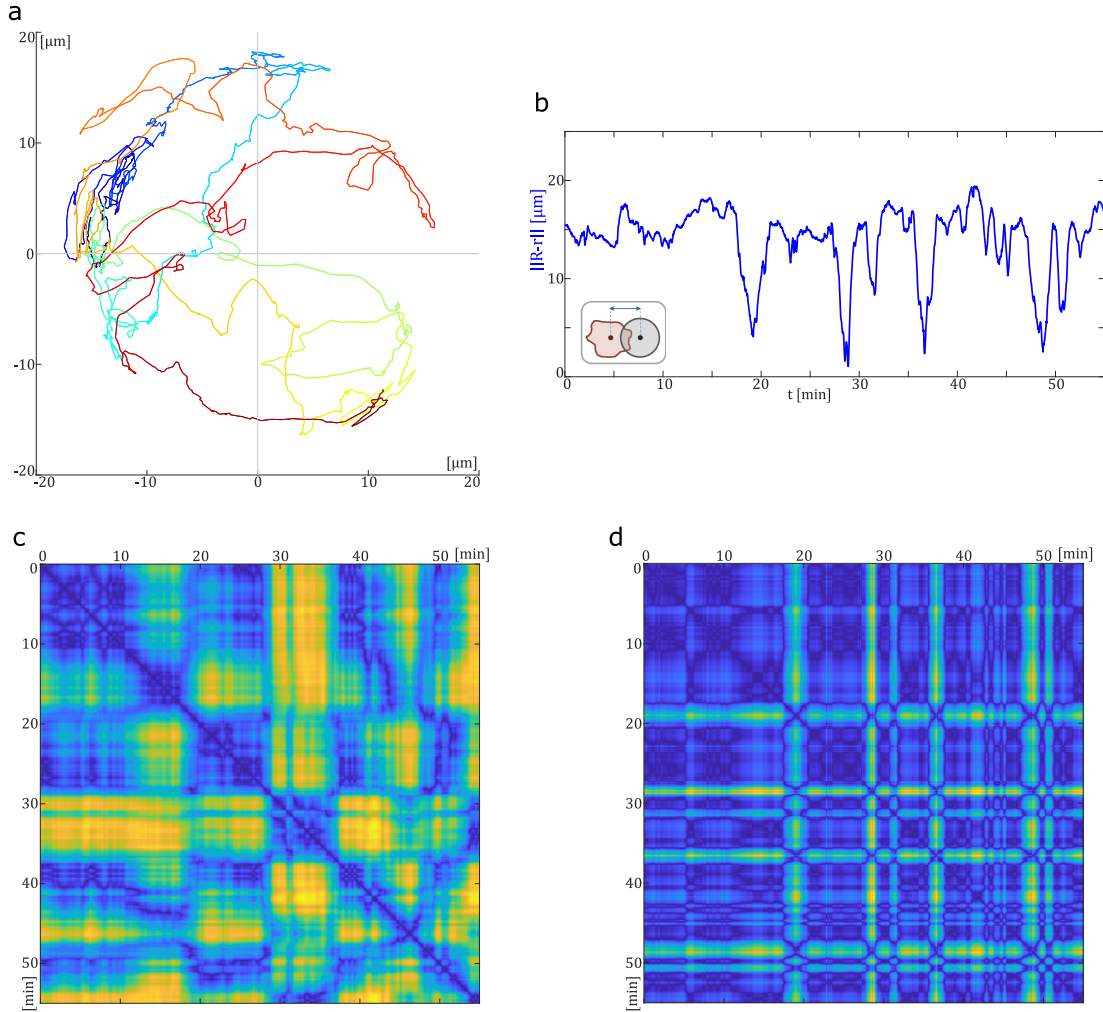


Figure 4.9: Overview on the type of information, regarding cell-cargo relative motion, extracted from simultaneous tracking of cell and particle. **a** Evolution of the cell relative position $\vec{r}_{\text{rel}}(t)$ around the particle position. Time is colour-coded, from blue to red. **b** Plot of the corresponding time series of relative distance $\|\vec{r}_{\text{rel}}(t)\|$. **c** and **d** are the corresponding Recurrence Plots, respectively, for $\vec{r}_{\text{rel}}(t)$ and $\|\vec{r}_{\text{rel}}(t)\|$. The measure of similarity $I(t_i, t_j)$, properly rescaled, is colour-coded from dark blue ($I = 0$, high similarity) to light yellow ($I = 1$, low similarity).

maturation ($\sim 1/2$ min [22]): as already discussed for the measurement of cell speeds in Section 4.1, such time filtering solves this type of issues by returning trajectories more faithful to actual cell displacement.

By collecting counts of reorientation events from several time series, and classifying them on the basis of particle size, I could carry out a *Maximum Likelihood Estimation* of reorientation rates, assumed Poissonian, for different cargo sizes. As illustrated in Appendix A, by maximizing the likelihood for a Poissonian model $n(t) \sim \text{Pois}(\lambda)$ to yield a measured occurrence count, one eventually comes to the following estimates for the rate parameter λ and its standard deviation $\sigma_{\hat{\lambda}}$:

$$\hat{\lambda} = \frac{\sum_i n_i}{\sum_i T_i} \quad \sigma_{\hat{\lambda}} = \frac{\hat{\lambda}}{\sqrt{\sum_i n_i}}$$

with n_i and T_i respectively event count and time duration of a given time series i .

COUPLE INTERACTION

The physical quantity represented by $\vec{r}_{\text{rel}}(t) = -l_0 \vec{\Delta}(t)$, namely the cell-cargo relative position, has been of interest for more than just dynamical features.

In fact, by binning a time series of $\|\vec{r}_{\text{rel}}(t)\| = r_{\text{rel}}(t)$, one obtains a distribution of counts, or frequencies, for the relative distance being within the range ρ^i of the i -th bin, i. e. $n(r_{\text{rel}} \in \rho^i) = n(i)$; this type of information is commonly visualized as an histogram.

Given a time series spanning a sufficiently broad time frame¹⁴, so to sample a window of the stationary dynamics for the process of interest, the relative frequencies $\frac{n(i)}{\sum_i n(i)}$ obtained by this procedure will represent, according to the definition of statistical probability¹⁵, a time-averaged estimate of probability for the observable (here being $\|\vec{r}_{\text{rel}}(t)\|$) to measure within the i -th bin [25].

Further normalization of the relative frequencies by the bin width w_i ultimately provides a numerical estimate of the steady-state probability density function $p(r_{\text{rel}})$:

$$\hat{p}(r_{\text{rel}}) dr_{\text{rel}} = \frac{n(i)}{w_i \sum_i n(i)} \quad r_{\text{rel}} \in \rho^i$$

Such empirical probability distributions are particularly valuable in light of their connection with the system's thermodynamics, as being observable manifestation of the underlying interactions.

As a matter of fact the probability distribution of any physical quantity q , for a system weakly coupled¹⁶ with its surrounding and in thermal equilibrium with it, is dictated by the energy landscape $E(q)$, according to the canonical (or Gibbs) distribution:

$$p(q) = \frac{1}{Z} e^{-\beta E(q)} \quad (4.4)$$

with $Z = \int_{\bar{q}} e^{-\beta E(\bar{q})}$ normalization constant (so-called partition function), and β^{-1} relates to the noise power (energy scale for the fluctuations, $\beta^{-1} = k_B T$ for thermal

¹⁴ I. e. longer than the characteristic time scale of the underlying physical process.

¹⁵ Statistical probability is defined as the long-run limit value of the relative frequency with which a given event occurs, namely the limiting value to which the ratio of occurrence $\frac{n_{\text{occur}}}{n_{\text{total observations}}}$ would converge for an hypothetical endless measurement/dataset. This empirical definition of probability differs conceptually (and sometimes even practically) from its logical counterpart, the so-called inductive probability: the two concepts define different schools of thought partially in conflict, and theoretical conundrums still to be addressed. [25]

¹⁶ For two macroscopic systems in thermal contact with each other (meaning they exchange energy exclusively at a microscopic/molecular scale, i. e. as heat) the overall hamiltonian can be written as $\mathcal{H} = \mathcal{H}_1 + \mathcal{H}_2 + \mathcal{H}_{1-2}$, with \mathcal{H}_{1-2} coupling term that adds to the unperturbed hamiltonians \mathcal{H}_1 and \mathcal{H}_2 the two systems would have if isolated. The presence of this term reflects how the accessible microscopic configurations for the two systems are dependent on each other, thus energy is not additive and the numerosity of total possible configurations $\Omega(\mathcal{H})$ does not factorize. However, for intermolecular interactions decaying within a distance of the order of few molecules (better defined in the context of mean field theory), the coupling will involve a very limited number of molecules at the interface, with negligible contribution to the energy of the two systems, exclusively allowing heat exchange between them. It follows that microstates onfiguration $\Omega_i(\mathcal{H}_i)$ for the single systems will not be significantly affected by the thermal contact, and $\Omega(\mathcal{H}) \simeq \Omega_1(\mathcal{H}_1) \cdot \Omega_2(\mathcal{H}_2) \simeq \Omega_1(\mathcal{H}_1) \cdot \Omega_2(\mathcal{H} - \mathcal{H}_1)$. This condition, rather ubiquitous in statistical physics, is defined as *weak coupling*. [121]

noise); this represents a pivotal result of statistical physics and direct consequence of the fundamental assumption of statistical mechanics¹⁷ [84, 121].

A probability-energy relation as in equation (4.4) can actually be generalized to any observable of a stationary out-of-equilibrium system, granted the probability current for the observable goes to zero, namely, detailed balance¹⁸ is satisfied [133, 176]. In the specific case of the cell-cargo system, it is reasonable to say the relative distance dynamics satisfies detailed balance: as discussed in Chapter 5, $r_{\text{rel}}(t)$ consistently shows a steady and recurrent dynamics with no measured drift over time (as in figure 4.9b) which, on the contrary, would emerge from a non-zero probability current¹⁹. This gives credit to the estimate $\hat{p}(r_{\text{rel}})$, and enables the calculation of an effective energy landscape Φ for the relative distance by simply inverting equation (4.4):

$$\Phi(r_{\text{rel}}) = \beta E(r_{\text{rel}}) = -\log \left[\frac{p(r_{\text{rel}})}{p(r_{\text{rel}})^{\text{ref}}} \right]$$

where Φ is an adimensional measure of interaction strength, leading to a radial *effective interaction potential* for the cell-cargo couple, as previously shown in literature in similar contexts [36]. In this expression, $\log [p(r_{\text{rel}})^{\text{ref}}]$ is an arbitrary reference value for the energy; I defined $p(r_{\text{rel}})^{\text{ref}} = p(r_{\text{rel}} : r_{\text{rel}} \in \rho^1)$.

Figure 4.10 gives a glance at the workflow of such strategy for cell-cargo interaction analysis.

The outcome of this approach for empirical estimation of probability distributions and effective potentials is, to some extent, intrinsically dependent on the binning procedure, that is the positioning of bin edges along the full range of $r_{\text{rel}}(t)$: the fewer in number and wider are the bins that cover the range of measured values, the higher the count each bin will contain, thus the estimated probabilities will be more reliable, less affected by statistical fluctuations. However, increasing the bin width gives a coarser, less resolved, probability distribution for the values of the observable. On the other hand, distributions estimated via excessively fine binning are characterized by

17 The fundamental assumption of statistical mechanics consists in a foundational principle of statistical physics, stating that «An isolated system in equilibrium is equally likely to be in any of its accessible states». This translates into assuming a flat probability distribution for the $\Omega(E)$ accessible microscopic configurations of an isolated system with energy E , which implies a probability distribution $p(q) dq = \frac{\Omega(q|E)}{\Omega(E)}$ for any generic physical quantity q of the system, called *microcanonical distribution*. A microcanonical distribution for the energy E_s of a system in equilibrium with its surrounding (keep in mind, a system with its surrounding represents an isolated system by definition), weighting for the degeneracy of microstates $\Omega(E_s|E)$, leads (under hypothesis of weak coupling) to the so-called *canonical distribution* as defined by equation (4.4). [84, 121]

18 A stochastic process satisfies *detailed balance* when there are no net probability currents within its state space. This is in fact a more stringent condition than stationarity.

For example, considering for simplicity a discrete-time Markovian process with a discrete state space, an equation for the time-evolution of probability of state i will have the form $P^t(i) - P^{t-1}(i) = \sum_{k \neq i} (P^{t-1}(k) \cdot P(k \rightarrow i) - P^{t-1}(i) \cdot P(i \rightarrow k))$ (so-called Master equation), with $P(k \rightarrow i)$, $P(i \rightarrow k)$ transition rates responsible for probability currents to and from state i . As it can be easily seen from such equation, stationarity requires only for the sum of all net probability fluxes to be zero, while detailed balance forces each each single net flux $(P^{t-1}(k) \cdot P(k \rightarrow i) - P^{t-1}(i) \cdot P(i \rightarrow k))$ in the sum to be zero. In other words, detailed balance reflects a steady state with no circuitation of probability, namely a conservative stochastic process. For a more advanced discussion, and its connection to thermodynamics and equilibrium, see e.g. [61].

19 For a bounded 1-dimensional state space as the set \mathbb{R}^+ , stationarity in the probability distribution can only be achieved with no probability flow, that is when detailed balanced is satisfied.

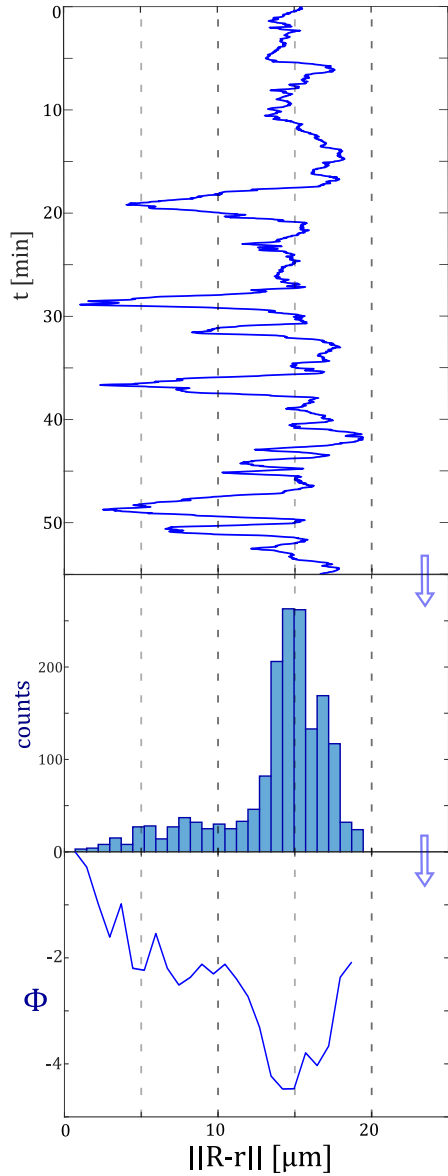


Figure 4.10: Schematics of the cell-cargo interaction analysis workflow. The time series of relative distance $\|\vec{r}_{\text{rel}}(t)\|$ (**top** figure) is binned into an histogram of frequencies (in the **center**), counting the total time (in frames) spent by the cell within given ranges (the bins) of relative distance from the cargo. Being such counts (properly normalized) an estimate for probability, an effective interaction potential (**bottom** plot) can be calculated from the distribution of frequency by generalizing the canonical distribution.

being noisy and strongly sensitive to the specific value of bin width used, leading to a lack in robustness of the whole analysis.

A proper binning relies on a trade-off between resolution and statistical significance, basically choosing the smallest bin width possible still granting good estimates, so to obtain the optimal distribution shape given a limited set of data. For this purpose I made use of an automatic binning algorithm implemented in MATLAB (syntax: `histogram(r_rel, 'BinMethod', 'auto')`), which uses constant bin widths optimized to return the most faithful possible shape of the underlying distribution.

By binning altogether several time series within the same cargo size category, I obtained population-wide probability distributions and effective interaction potentials for each tested particle diameter.

To compensate for the limited yet present cell-to-cell variability in cell size (the latter arguably acting as spatial scale of relative motion and affecting relative distance distribution), thus making more consistent ensemble statistics, values of each $r_{\text{rel}}(t)$ time series have been normalized by the respective average cell radius, defined as the

radius $\hat{\rho}_{\text{cell}} = \sqrt{\hat{A}_{\text{cell}}/\pi}$ of a circle with area equal to the average projected area \hat{A}_{cell} of the cell during a given measurement.

As stated in Section 3.3, the time-lapse recording of different experiments has been carried out using no universal frame rate. As a consequence, time series have been downsampled when necessary, in order to match the lowest frame rate used ($(10\text{ s})^{-1}$): by having identical sampling density, equal time intervals from different measurements in an ensemble are always granted equal weight in shaping the population-wide distribution.

4.3 NUMERICAL STOCHASTIC SIMULATIONS

All of the algorithmic strategies discussed in this section have been implemented in the form of MATLAB (MathWorks® Inc.) custom code.

SIMULATING THE *coarse-grained* MODEL

As thoroughly discussed in Section 6.1, my proposed coarse-grained mathematical model describes the motion of the cellular truck center of mass $\vec{x}(t)$ as governed by the following Langevin equation²⁰:

$$\frac{d}{dt}\vec{x}(t) = v[s] \cdot \vec{p}[\phi(t)] + \sqrt{2D_{\text{int}}}\vec{\xi}_{\text{int}}(t) \quad (4.5)$$

where: $\sqrt{2D_{\text{int}}}\vec{\xi}_{\text{int}}(t)$ describes a Gaussian δ -correlated noise, with zero mean and standard deviation (i. e. noise amplitude) $\sqrt{2D_{\text{int}}}$; $v[s] \cdot \vec{p}[\phi(t)]$ represents the active term encoding for the peculiar intermittent dynamics of the cellular truck, and is therefore dependent on which behavioural phase the truck is at time t .

According to the model, the three behavioural phases \mathcal{S} , \mathcal{R} and \mathcal{M} (introduced and described in detail in Section 5.1) define a Markov chain²¹ for the cellular truck (depicted in Figure 6.1), where transitions among different phases of the system are assumed to be Poisson processes thus stochastically occurring with constant rates. As a consequence, dwelling times for the system in any phase are exponentially distributed.

Every occurrence of phase \mathcal{R} is bound to trigger a random reorientation of the truck's polarity vector $\vec{p}[\phi(t)]$:

$$\mathcal{S} \rightarrow \mathcal{R} \vee \mathcal{M} \rightarrow \mathcal{R} \implies \phi \rightarrow \phi + \delta\phi$$

The truck velocity $v[s]$ is treated as a dichotomous variable, with a switch s that makes it non-zero during phase \mathcal{M} only:

$$v[s] = \begin{cases} 0 & s = 1 \text{ (behavioural phases } \mathcal{S}, \mathcal{R}) \\ v_{\text{run}} & s = 2 \text{ (behavioural phase } \mathcal{M}) \end{cases}$$

²⁰ See Section 2.1 for a brief introduction on Langevin equations.

²¹ A Markov chain is a stochastic model, often depicted as a directed graph, describing a memory-less stochastic process as sequence of mutually exclusive events or states, occurring with probabilities depending solely from the state previously attained (namely, the Markov property) [58].

In order to simulate such Langevin dynamics, I developed an algorithm for numerical integration of equation (4.5), inspired by the Gillespie algorithmic scheme [59]. Explicitly, given a fully polarized (phase \mathcal{M}) cellular truck at time t with orientation $\phi(t)$, and an index $i(t)$ counting the occurrence of reorientation events:

1. generation of the time interval $T_{i+1} \sim \text{Exp}(\lambda)$ before the occurrence of the next repolarization/reorientation of the truck (decision on *when* to reorient);
2. generation of the change in orientation $\delta\phi_{i+1} \sim \text{Unif}(-\pi, \pi)$ caused by the next reorientation (decision on *where* to reorient);
3. generation of the time duration $T_{i+1}^{\text{rev}} \sim \text{Exp}(\alpha)$ of the next reorientation event (how much time it takes to reorient, i. e. the time spent dwelling in phase \mathcal{R});
4. numerical integration of the Langevin dynamics within the time interval $[t, t + (T_{i+1} + T_{i+1}^{\text{rev}})]$:
 - a) generation of the cell polarity persistence time $T_{i+1}^{\text{run}} \sim \text{Exp}(\tilde{\sigma})$;
 - b) within $[t, t + \min\{T_{i+1}, T_{i+1}^{\text{run}}\}]$, numerical integration of equation (4.5) by assuming $s = 2$ (phase \mathcal{M});
 - c) within $[t + \min\{T_{i+1}, T_{i+1}^{\text{run}}\}, t + (T_{i+1} + T_{i+1}^{\text{rev}})]$, numerical integration of equation (4.5) by assuming $s = 1$ (phase \mathcal{S} if occurring, phase \mathcal{R});
5. update orientation angle ($\phi \rightarrow \phi + \delta\phi_{i+1}$) and index i ($i \rightarrow i + 1$), thus repeat from point 1.

My program simulates in parallel several cellular trucks, using vectorized code to better exploit Matlab performances for matrix operations.

Particularly, the stochastic variables T_i , $\delta\phi_i$, T_i^{rev} and T_i^{run} are simultaneously generated for every occurrence i and all simulated systems, which lead to matrices as, e. g.

$$\mathbb{T} = \begin{bmatrix} T_{1,1} & \dots & T_{1,N_{\text{ens}}} \\ \vdots & \ddots & \vdots \\ T_{N_{\mathcal{R}},1} & \dots & T_{N_{\mathcal{R}},N_{\text{ens}}} \end{bmatrix}$$

with $N_{\mathcal{R}}$ and N_{ens} being the maximum number of simulated reorientations and the population size, respectively.

As a consequence, the total time a system's dynamics is simulated for is not a deterministic parameter, since a maximum is fixed for the \mathcal{R} phase occurrence counter i rather than for time t . This also implies for simulations performed in parallel to have generally different time lengths, distributed around an average duration of $N_{\mathcal{R}}(\lambda^{-1} + \alpha^{-1})$: ensemble-averaged Mean Squared Displacements are calculated over a time span corresponding to the shortest of the simulated tracks; diffusivity curves $\mathcal{D}(\lambda)$ are sampled by using values of $N_{\mathcal{R}}$ increasing with λ .

The numerical integration of equation (4.5) is performed via a forward Euler scheme for finite differences approximation of the time derivative [128], which leads to:

$$\vec{\Delta x}(t) = \vec{x}(t + \Delta t) - \vec{x}(t) = \Delta t \cdot v[s] \cdot \vec{p}[\phi(t)] + \sqrt{2D_{\text{int}}\Delta t} \vec{\zeta}_{\text{int}}(t)$$

where the noise $\sqrt{2D_{\text{int}}\Delta t}\zeta_{\text{int}}^{\vec{r}}(t)$ results from summing over the multitude of independent realizations of the process $\sqrt{2D_{\text{int}}}\xi_{\text{int}}^{\vec{r}}(t)$ within the time step Δt , hence again a zero mean Gaussian noise²², δ -correlated in between time steps.

To generate all stochastic variables, I used a pseudorandom number generator algorithm [83] to numerically produce uniformly distributed random numbers in the interval $[0, 1] \subset \mathbb{R}$, thus I performed (when necessary) Inverse Transform Sampling (or simply Inversion method) [42] over such numbers, so to remap them within the domain of existence of the stochastic variable of interest according to the requested distribution.

SIMULATING THE *full-scale* MODEL

As opposed to its coarse-grained counterpart, the full-scale model resolves cell and particle dynamics, by means of a Langevin equation for the cell position $\vec{r}(t)$ and another describing the relative motion:

$$\frac{d}{dt}\vec{r}(t) = v[s] \cdot \vec{p}[\varphi(t)] + \sqrt{2D}\vec{\xi}_r(t) \quad (4.6a)$$

$$\vec{R} = \vec{r} + l_0\vec{\Delta}, \quad \frac{d}{dt}\vec{\Delta}(t) = -\alpha \left(\vec{\Delta}(t) - \vec{\Delta}_0[s] \right) + \sqrt{2D_{\Delta}}\vec{\xi}_{\Delta}(t) \quad (4.6b)$$

with \vec{R} being the particle position.

Here, the variable $s \in \{1, 2\}$ refers to the motile state of the cell only (persistent motion when cell polarized, as in behavioural phases R and M), unlike for the coarse-grained model where it acts as motility switch for the whole truck (persistently moving only during behavioural phase M by definition). As a matter of fact, the value assumed by s is determined by a different Markov chain (depicted in Figure 7.1), modelling the alternation between non-polar and polar biophysical states of the cell, which dictates an intermittent motion for the virtual cell in line with experimental evidence (see Section 7.1 for further details).

An additional Langevin equation $\frac{d}{dt}\varphi(t) = \sqrt{2D_{\varphi}}\xi_{\varphi}(t)$ introduces some degree of noise in the orientation of the cell's polarity vector $\vec{p}[\varphi(t)]$.

The derivation and physical meaning of this mathematical model is thoroughly discussed in Section 7.1.

Such two-body Langevin dynamics is simulated by numerical integration of equations (4.6), performed via a forward Euler scheme for finite differences approximation of the time derivative [128], which translates in iteratively solving the following set of coupled numerical equations:

$$\begin{aligned} \Delta\vec{r}(t) &= \Delta t \cdot v[s] \cdot \vec{p}[\varphi(t)] + \sqrt{2D\Delta t}\vec{\zeta}_r(t), & \Delta\varphi(t) &= \sqrt{2D_{\varphi}\Delta t}\zeta_{\varphi}(t) \\ \Delta\vec{R}(t) &= \Delta\vec{r}(t) + l_0\Delta\vec{\Delta}(t), & \Delta\vec{\Delta}(t) &= -\alpha \left(\vec{\Delta}(t) - \vec{\Delta}_0[s] \right) \cdot \Delta t + \sqrt{2D_{\Delta}\Delta t}\vec{\zeta}_{\Delta}(t) \end{aligned}$$

with $\zeta \sim N(0, 1)$ for all noises, assumed independent and δ -correlated in time.

As the Langevin equations are numerically integrated, the stochastic switching of a cell's motile state is simulated according to the Markov chain in Figure 7.1, set to govern the active cell motion.

²² By virtue of the Central Limit Theorem [25].

Specifically, a polarized cell ($s = 2$) may repolarize

$$\{s = 2, \vec{p}[\varphi]\} \rightarrow \{s = 2, \vec{p}[\varphi']\} \sim \text{Pois}(\lambda)$$

or lose polarity

$$\{s = 2, \vec{p}[\varphi]\} \rightarrow \{s = 1\} \sim \text{Pois}(\sigma)$$

at random. This translates in a probability $P[2 \rightarrow (1 \vee 2)] = 1 - e^{-(\lambda+\sigma)\Delta t}$ that a change in the current state of cell polarity (either repolarization or depolarization) occurs at any time step, leading either again to state $s = 2$ or to state $s = 1$ with conditional probabilities $\frac{\lambda}{\lambda+\sigma}$ and $\frac{\sigma}{\lambda+\sigma}$, respectively.

For a non-polar cell (isotropic, $s = 1$), repolarization

$$\{s = 1\} \rightarrow \{s = 2, \vec{p}[\varphi']\} \sim \text{Pois}(\lambda)$$

is the only event possibly occurring, with a probability $P[1 \rightarrow 2] = 1 - e^{-\lambda\Delta t}$ at any time step.

The stochastic time evolution of the cell's motile state is thus easily simulated by exploiting uniform distributions²³: at each time step, a random number rnd uniformly distributed in the interval $[0, 1] \subset \mathbb{R}$ is numerically generated, using a pseudorandom number generator algorithm [83]; if $rnd \in [0, P]$, the cell switches from its current state. If it were in state $s = 2$, another random number rnd is generated, then a decision on which state to attain next is made with analogous strategy ($rnd \in [0, \frac{\lambda}{\lambda+\sigma}] \Rightarrow s = 2 \rightarrow 2$, $rnd \in (\frac{\lambda}{\lambda+\sigma}, 1] \Rightarrow s = 2 \rightarrow 1$).

At every occurrence of repolarization ($s = (1 \vee 2) \rightarrow 2 \sim \text{Pois}(\lambda)$), the cell instantaneously polarizes towards the particle $\varphi(t) \rightarrow \theta(t) + \eta$, with $\eta \sim N(0, 0.2)$; thus the minimum energy relative position vector

$$\vec{\Delta}_0[s] = \begin{cases} +\vec{e}_\Delta[\theta] = \frac{\vec{\Delta}(t)}{\|\vec{\Delta}(t)\|}, & s = 1 \\ -\vec{p}[\varphi], & s = 2 \end{cases}$$

flicks accordingly.

The pull of the cargo over the cell, key feature of the cellular truck reorientation, is consequently reproduced by the term $-\alpha \left(\vec{\Delta}(t) - \vec{\Delta}_0[s] \right) \cdot \Delta t$, encoding for the cell-cargo mechanical interaction, with α dictating the time scale of such process.

It is worth of notice that the reorientation of the cellular truck (behavioural phase \mathcal{R}) is not "hardcoded" as a state in the Markov chain governing the active term, as it is for the coarse-grained model, but rather emerges as a dynamical process during the polarized activity of the cell ($s = 2$), driven by the encoded internal mechanics of the cellular truck.

²³ Given $rnd \sim \text{Unif}(0, 1)$ and $x \in [0, 1] \subset \mathbb{R}$, it results $P[rnd \in [0, x]] = \int_0^x \frac{1}{1-0} d(rnd) = x$.

Part III

RESULTS & DISCUSSIONS

5.1 A DETAILED LOOK AT THE CELLULAR TRUCK BEHAVIOUR

THE CELLULAR TRUCK

Figure 5.1 depicts a typical conformation of a cell-cargo system, referred to as *cellular truck* (or simply truck) hereafter. Cellular trucks systematically exhibited transient directed runs, during which the particle lies towards an edge of the cell while the latter moves roughly in the opposite direction, displacing the cargo by acting as a puller.

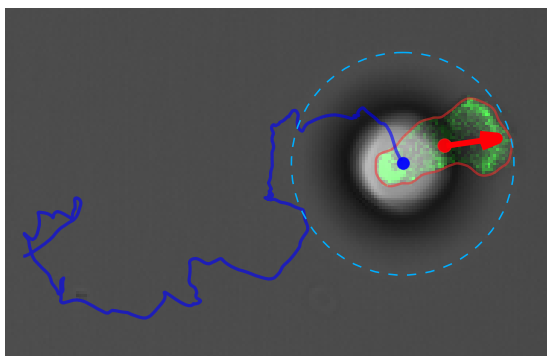


Figure 5.1: Dual-channel confocal imaging of a *cellular truck*, loaded with a $20\ \mu\text{m}$ spherical polystyrene particle. In green, fluorescent cytoskeletal Actin. In grey-scale, the signal from the transmitted light channel, mapping inhomogeneities in refractive index along the optical path. The spherical particle creates a characteristic refraction pattern, visible in transmitted light as a brighter central area (roughly corresponding to the particle's optical section at the focal plane) surrounded by a dark corona, which fades gradually within the projected area of the particle (here highlighted as a dashed azure circle). Overlaid in solid blue and red, respectively, cargo trajectory (time duration $\Delta t = 27\ \text{min}$) and detected cell boundary and speed vector.

The optical confocality of the imaging system (see Section 3.3) grants vertical resolution, which in turn provided knowledge on the vertical positioning of the cargo relative to the cell. The cargo has ever been found lying over the cell, interacting with its dorsal surface as the ventral one adheres on the flat substrate (see illustration in figure 5.2c).

Given the non-specific adhesive capabilities of the amoeba *Dictyostelium discoideum* (the cellular carrier), the binding of polystyrene microparticles (the cargo) to the cellular membrane did not require any surface functionalization (in line with previous studies [108]), whereas this may be required for specific applications depending on the cell type. Here, the physical link between cargo and carrier is established spontaneously as a cell gets in touch with a particle; following contact, the particle adheres to the cell membrane, allegedly through van der Waals interactions [92], and is thereupon subjected to forces exerted by the cell.

Multi-channel live cell imaging recordings (see Section 3.3) involving the genetically engineered *Dictyostelium discoideum* strain LimE-mRFP MyoII-GFP AX2, shed some light on the underlying mechanisms governing the behaviour of a cellular truck.

This double mutant strain (described in Section 3.1) expresses different fluorescent labels for Myosin II protein and F Actin-binding protein. As introduced in Section 1.3, directed amoeboid locomotion involves a cycle of protrusive and retractive deformations, during which cell cytoskeleton symmetry is broken, particularly: Myosin II tends to accumulate at the trailing edge of the cell, generating traction and pulling forward the cell body; conversely, filamentous Actin-rich regions include Actin foci (dense regions of Actin cortex at substrate-adhering sites [161]) and growing cellular protrusions, the latter defining the leading edge of what results to be a polarized cell [38].

Consequently, this type of experiments allowed the motions of cell and cargo to be resolved while visualising the polarization of the cell cytoskeleton.

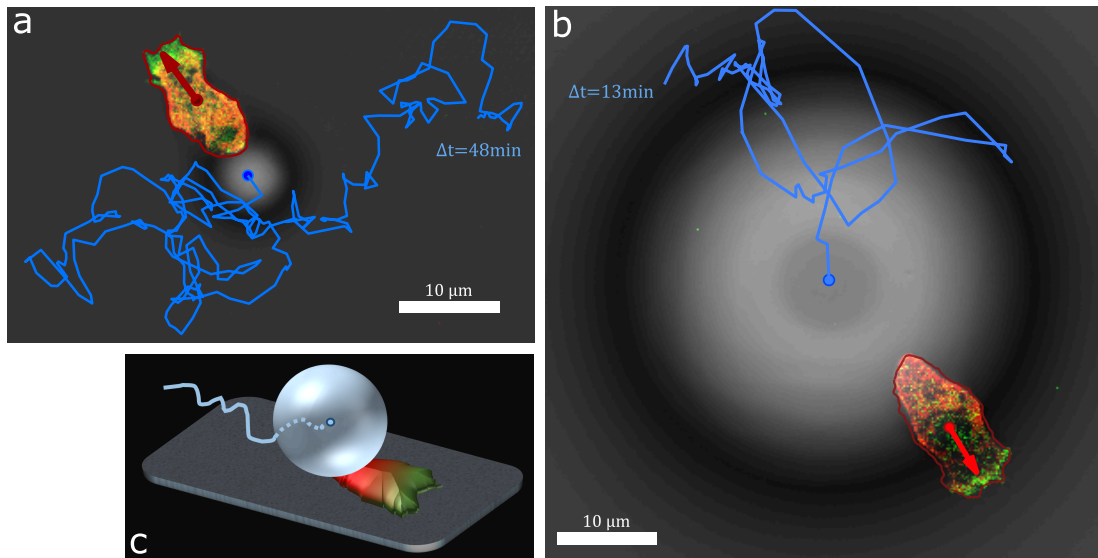


Figure 5.2: **a-b** Multi-channel confocal microscopy images of *cellular trucks*, loaded with **a** $10\ \mu\text{m}$ and **b** $45\ \mu\text{m}$ spherical polystyrene particles. Here, the double-mutant cell strain LimE-mRFP MyoII-GFP AX2 has been employed as carrier, allowing visualization of Myosin II (in red) and F-Actin (in green) proteins distributions. Overlaid in solid blue and red, respectively, cargo trajectory and detected cell boundary and speed vector. **c** Three-dimensional sketch of a cellular truck moving over a flat substrate; cell polarity is represented by color gradient within the cell body, as red and green encode for Myosin-rich and F Actin-rich regions, respectively.

As shown in figure 5.2**a-b**, the aforementioned transient directed runs resulted to be associated with a markedly polarized configuration of the cytoskeleton, where the particle locates towards the rear edge of the cell, corroborating the role of the cell as puller.

By simultaneously observing cytoskeletal dynamics and cell-cargo displacements, I could identify three distinct *behavioural phases*, consistently emerging for all the tested particle sizes, which are shown in figure 5.3**a-c**:

- *Stop (S) phase.* The cell and the particle move around each other, keeping their relative distance roughly constant, without significant net displacement of the whole truck; in this phase, the cell shows short-lived if no cytoskeletal polarization. Trucks can dwell in such phase up to several tens of minutes.
- *Reorientation (R) phase.* The cell suddenly polarizes towards the cargo, crawling underneath while pulling the latter towards its newly defined rear. This process usually takes a few minutes; I define τ_{rev} as its characteristic time duration, and λ as its rate of occurrence.
- *Motile (M) phase.* After such transition, a persisting cell polarization causes the cell to keep moving pulling the cargo forward; this phase is usually associated with significant displacement of the cellular truck. Once the cell spontaneously loses polarity, typically in a few minutes, such persistent run ends and the truck goes back to the phase S waiting for another reorientation event to be triggered. The cell may also repolarize towards the cargo while being in phase M; in such case, the truck ends its current run and directly jumps to the second behavioural phase R.

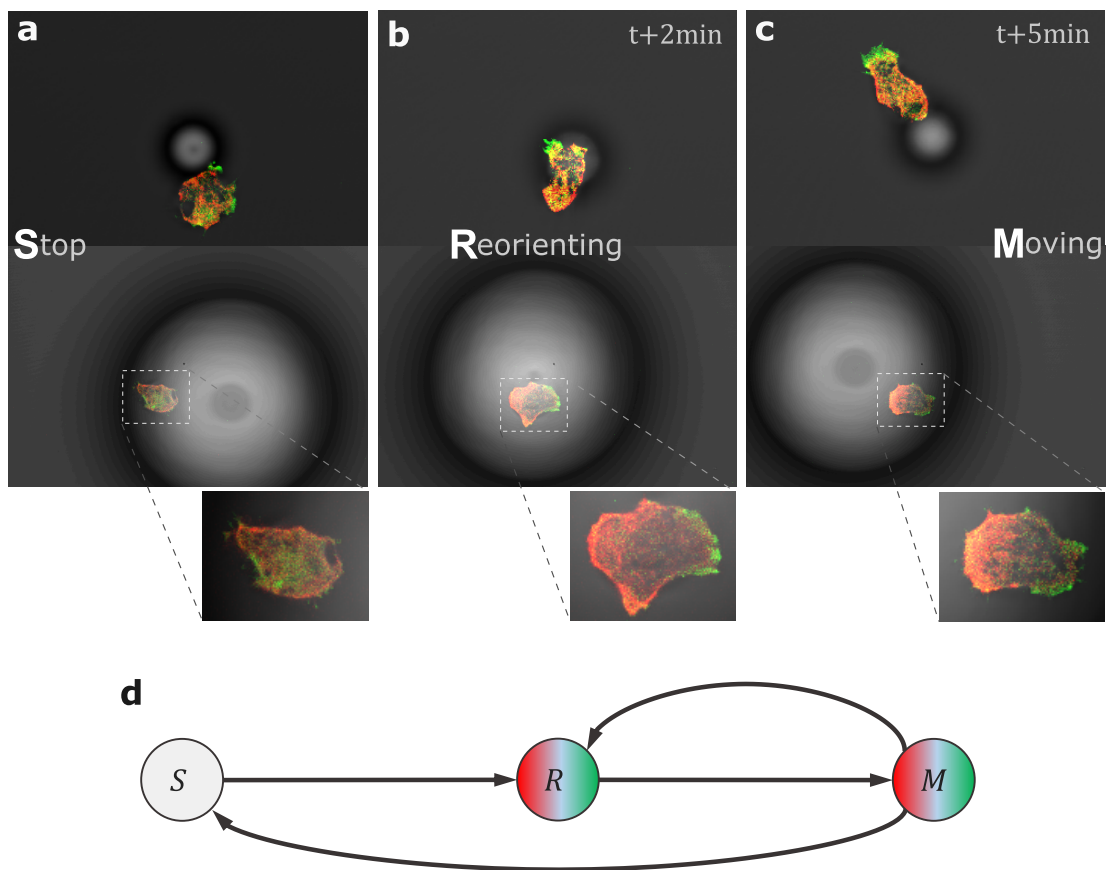
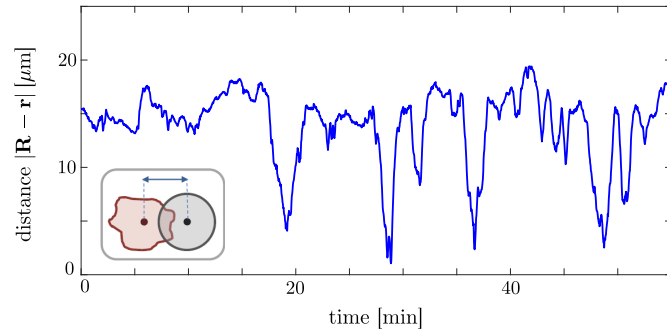


Figure 5.3: **a-c** Multi-channel confocal microscopy images of two cellular trucks, as they go through the three behavioural phases. Particles with diameter of $10\ \mu\text{m}$ and $75\ \mu\text{m}$ have been used as cargoes, respectively for the example on top and the one on bottom images. For the latter, additional close-ups on cell cytoskeletal polarity are provided. **d** Directed graph illustrating the connectivity among behavioural phases.

The structure of such behavioural cycle, i. e. the connectivity among behavioural phases, is graphically illustrated in figure 5.3d in the form of a directed graph.

This cyclic change of behaviour gives rise to a recurrent yet stochastic dynamics for the cell-particle relative distance, as for the example in figure 5.4: the relative distance consistently manifested steady and moderate fluctuations around a certain preferred value, interrupted by recurrent abrupt decays, manifest of the cell transiting under the particle as in phase \mathcal{R} , occurring randomly with rate λ . The average time interval between consecutive downward spikes $\tau = \lambda^{-1}$, i. e. the waiting time between cell repolarization/reorientation events, constitutes a time scale for the cellular truck internal motion.

Figure 5.4: Time series of the relative distance $r_{\text{rel}}(t) = \|\vec{r}(t) - \vec{R}(t)\|$, for a cellular truck loaded with a $45 \mu\text{m}$ particle.



THE ROLE OF CONFINEMENT

As already stated, the interaction between cell and cargo has been found to occur over the otherwise unconfined dorsal surface of the cell. In fact, the particle represents an additional substrate to which the cell can adhere, and its presence on top of the cell alters the otherwise flat geometry of the cell's surrounding environment.

Three-dimensional reconstructions of cellular truck geometries, obtained by stacking several consecutive optical sections of the system, clearly show the cargo as an additional confining structure for the cell, as it can be appreciated from the example shown in figure 5.5. No 3D reconstruction could be obtained for a truck while in phase \mathcal{R} or \mathcal{M} , since the acquisition time for a z-stack of images (with z-sampling, field of view and image resolution sufficient for my needs) required roughly 1 minute at the least, too slow to image the system during such highly motile phases. However, during recordings the cell always remained within the same focal plane, over the bottom of the dish, while the particle visibly moved vertically during phase \mathcal{R} (witnessed by a change in time of the section of the particle being imaged), proving the cargo to remain over the cell.

This evidence on cellular truck spatial configuration can account, at least qualitatively, for the characteristic motility behaviour observed during experiments: as described in Section 1.3, amoeboid motility relies on cyclic cell shape changes to propel the cell body, whose mechanics is governed by the adhesion pattern and mechanical stress of the cell [6, 9, 35]; as a consequence, the geometry of the surrounding environment can strongly affect cell migration [20, 21, 44, 109, 119, 122].

In the specific case of cellular trucks, additional adhesion provided by a confining particle may favour cell polarization by breaking Actin cortex symmetry (see Section 1.3), thus promoting motility along the cell-cargo axis, as illustrated in figure 5.6.

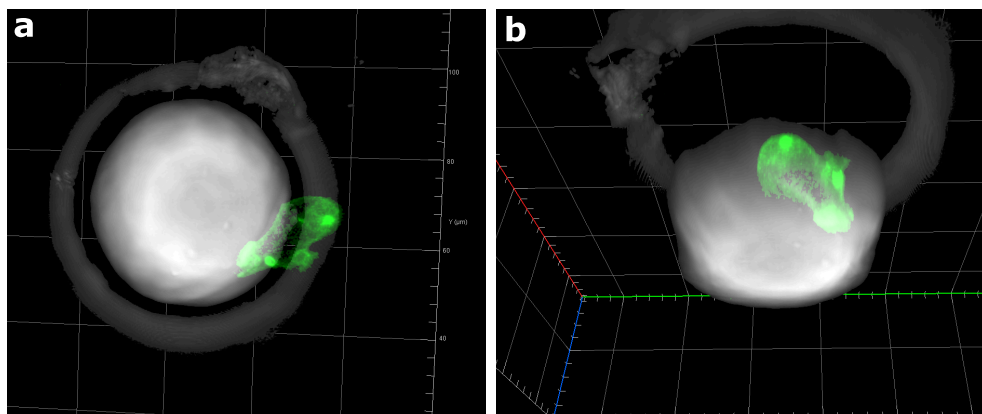


Figure 5.5: **a** Bottom view and **b** bottom-side view of a cellular truck three-dimensional geometry, reconstructed by z-stacking optical sections. In green, the Actin cytoskeleton; in grey scale, lower spherical cap of the particle, together with a circular halo the particle creates at optical sections above its equatorial plane, as its shape and refractive index mismatch cause lensing.

This may explain the spontaneous bursts of cell motility towards the cargo (phase \mathcal{R}), which drive cell transiting under it and give rise to the observed recurrent relative dynamics; moreover, a typical persistence in cell polarity [62, 119, 125] would cause the cell to keep crawling in the same direction for some time after transiting (as in phase \mathcal{M}), pulling the cargo forward and leading to net displacement of the truck.

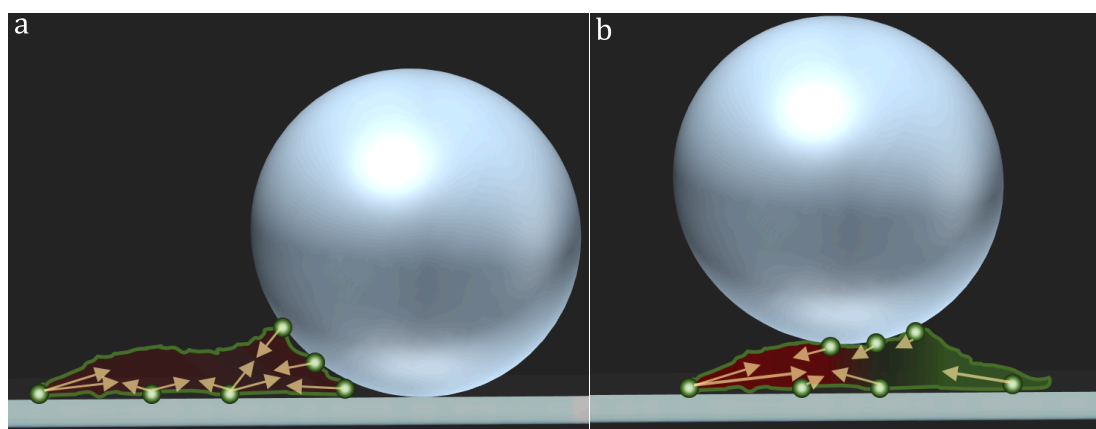


Figure 5.6: **a** Schematic representation of the broken cytoskeletal symmetry of a cell interacting with a particle. Here, small green circles on the cell membrane correspond to adhesion sites (Actin foci [161]), while vectors represent motor-generated contractile forces exerted on adhesion sites through the Actin network [139]. The same imaginary cell-cargo system is depicted in **b** during the consequent reorientation event (cell advancing towards the cargo while pulling the latter backwards); cytoskeletal polarity is represented by color gradient, as red and green encode for MyosinII-rich (trailing edge) and F-Actin-rich (emerging protrusions at leading edge) regions.

Driven by such interpretation, I developed prototypes of a microfluidic device aimed to analyse the occurrence of confinement-triggered bursts in cytoskeletal polarization, in a more simple and better defined confining geometry, to further investigate the symmetry breaking in cell motility.

These devices, realized by Soft Lithography as described in Section 3.2, consist in microfluidic circuits for cells to move through, designed in 2 variants:

- An *apolar* design (figure 5.7a-b) consists in linear parallel channels with symmetric constrictions, requiring the cell to squeeze in order to get through (square section with side of $5\ \mu\text{m}$). This circuit has been conceived to test the emergence of recurrent cell motion around a constriction, thus reproducing the cell-cargo relative motion in a simpler 1-dimensional setting.
- A *polar* design (figure 5.7c-d), similar to the previous but with asymmetric constrictions to possibly impose, solely by means of broken symmetry in substrate geometry, directionality to the otherwise random motion of the cell, inducing what we may call “*stenotaxis*”¹. Furthermore, a maximum inter-constriction distance able to grant directional migration could provide additional information on cell polarity persistence.

While I performed some preliminary experiments to test these prototypes, a proper protocol has to be developed, particularly regarding the delicate procedure of delivering healthy cells in the microchannels; such prototypes may also be optimized according to specific needs. This experimental platform, though stemming from my findings on cellular truck behaviour, represents a separate and diverse branch of future research, pointing to further understand the biophysics of amoeboid motion, hence its further study has not been under focus within my PhD project.

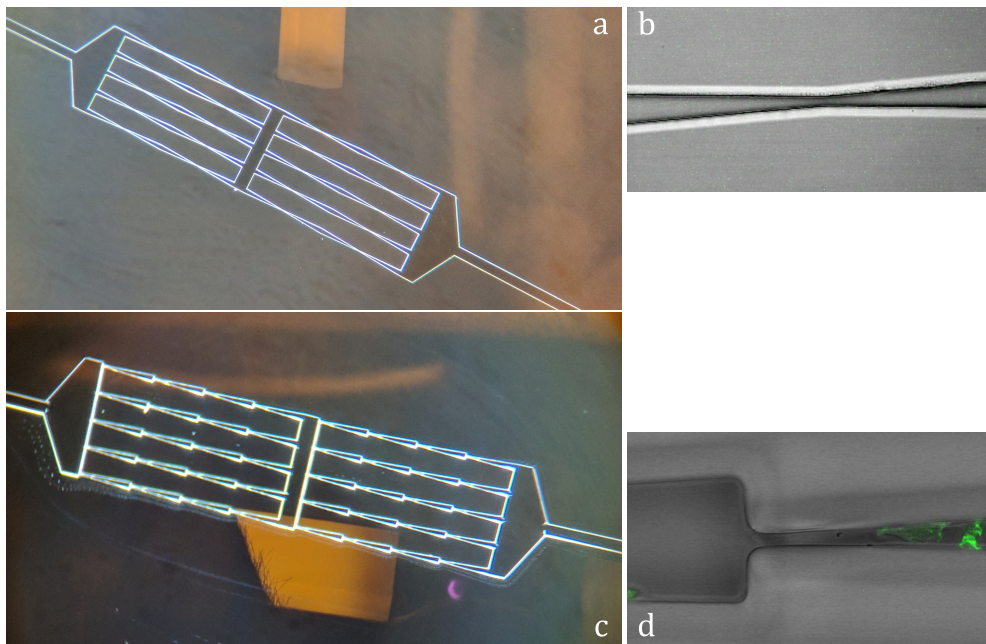


Figure 5.7: Microfluidic circuit geometries, here shown from the corresponding master wafers used for soft lithography, imaged in reflected light. Microchannels height and width at constriction are both $5\ \mu\text{m}$ a Apolar design, with b close-up on a symmetric constriction. c Polar design, with d close-up on the asymmetric constriction it features.

¹ from ancient greek words *stenos* (narrow) and *taxis* (arrangement, used in the context of cell migration to refer to directed/guided motion).

5.2 SHEDDING LIGHT ON CELL-CARGO RELATIVE DYNAMICS

Figure 5.8a compares relative distance time series of cellular trucks loaded with different particle sizes. While highlighting consistency in the qualitative features of their dynamics, comparative analyses disclosed crucial differences from a quantitative standpoint, with values of relative distance and time scale τ both increasing with particle size.

A more detailed look at the complex relative motion within the truck is provided by the relative trajectories $\vec{r}_{\text{rel}}(t) \stackrel{\text{def}}{=} \vec{r}(t) - \vec{R}(t)$, shown in figure 5.8b. As it can be seen, the cell tends to spend most of the time pulling the cargo randomly around itself, keeping a characteristic distance; as a consequence, well defined arcs arise within plots of relative trajectory, conferring a clearly outlined circular shape to the latter.

From time to time, the cell runs towards the particle, pulling the cargo to the opposite side. This reflects as bursts in relative motion, with quick and relatively straight runs roughly crossing the particle center.

The smaller the particle, the less prominent such pattern in the relative motion is, as it can be appreciated from the noisy trajectories of the relative motion emerging from measurements on $10\ \mu\text{m}$ particle-loaded trucks.

Recurrence Plots (RPs) allowed a quantitative analysis of the whole cell-cargo relative dynamics (see Section 4.2), granting insights on the type of dynamical process governing such motion.

In figure 5.8c three examples of RPs are shown for the time evolution of the cell relative position $\vec{r}_{\text{rel}}(t)$, involving three different particle sizes, where the similarity index $I(t_i, t_j) = \|\vec{r}_{\text{rel}}(t_i) - \vec{r}_{\text{rel}}(t_j)\|$ is colour-coded.

Such RPs generally displayed a distinctive checkerboard pattern, with patches of high similarity encoding for high time correlation, suggesting the presence of metastable states (or attractors), among which the systems abruptly jumps. These patches, often referred in literature as laminar phases [78], corresponded to dwells of the system in \mathcal{M} and \mathcal{S} behavioural phases, and usually showed gradual fading as the truck goes from phase \mathcal{M} (particle roughly fixed at the rear of the cell) to \mathcal{S} (particle pulled randomly around the cell).

Transitions between laminar phases emerged as well from RPs of the scalar relative distance $\|\vec{r}_{\text{rel}}(t)\|$, illustrated in figure 5.8d: here, information over the angular coordinate is lost and drastic decorrelation emerges exclusively during reorientation events (behavioural phase \mathcal{R}), as horizontal and vertical bands located at times of abrupt decay of relative distance. The comparison, between these RPs and their counterpart for the vectorial relative position, clearly showed the presence of rotational noise particularly during phase \mathcal{S} ; this would make less predictable the direction a cellular truck aligns to after the next reorientation event.

High laminarity patterns are representative of an intermittent dynamics [78, 95], reminiscent of dynamical processes typical of non-linear oscillators and excitable systems.

Laminar phases tended to be more defined and extended for bigger particles, reflecting longer dwelling times at a preferred distance for cells around big cargoes, consistently to the trend observed from $r_{\text{rel}}(t)$ time series. More faded and noisy RP arose for smaller cargo sizes as $10\ \mu\text{m}$ in diameter, in line with the simple observations on relative trajectories discussed previously.

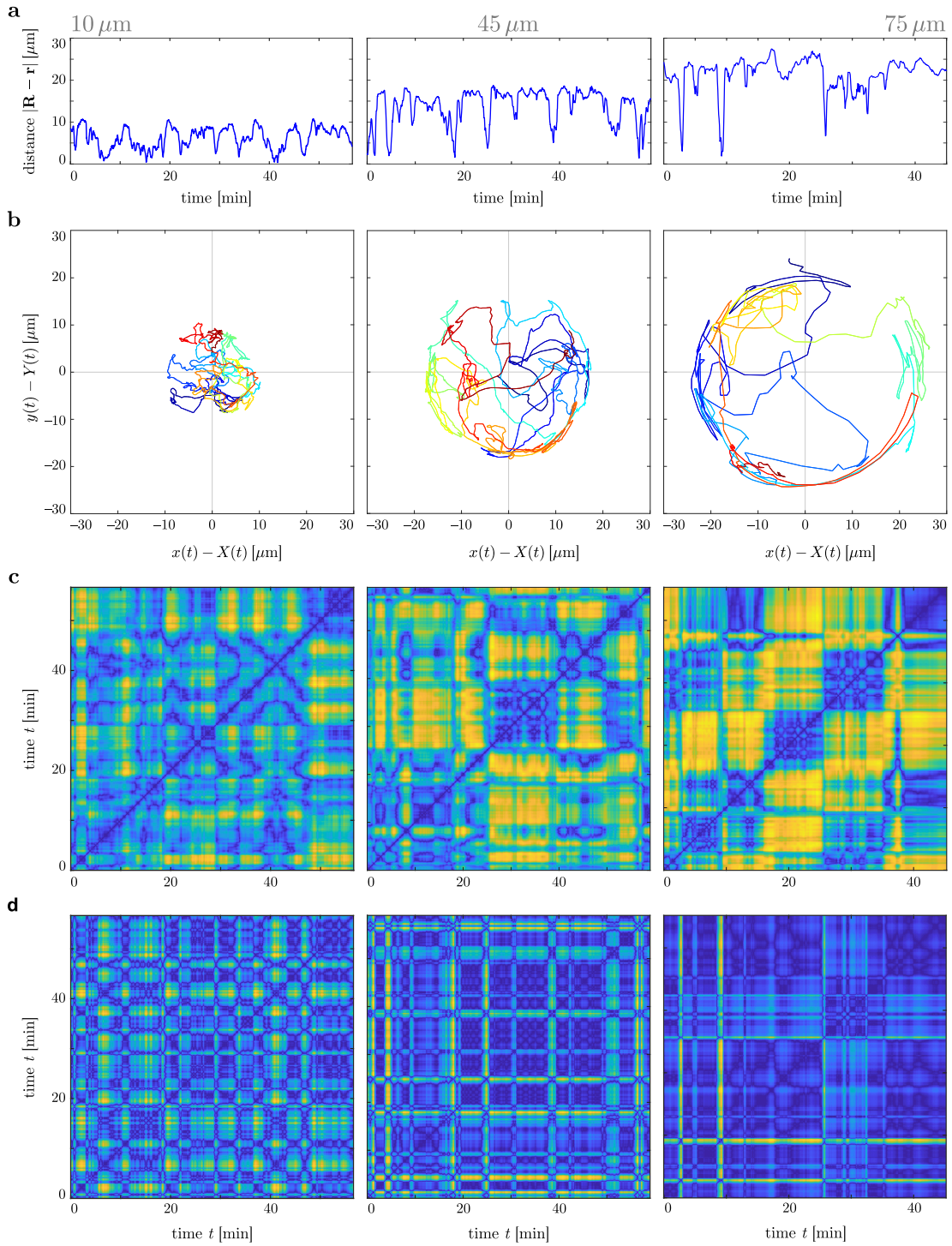


Figure 5.8: Analysis of the relative cell-cargo motion for three cellular trucks, loaded with particles of different size. **a** Time series of relative distance. **b** Relative cell trajectories with respect to particle position (colour-coded time, from blue to red). **c** Recurrence Plots of the time evolution of cell-cargo relative position $\vec{r}_{\text{rel}}(t)$. **d** Recurrence Plots of the time evolution of cell-cargo relative distance $r_{\text{rel}}(t) = \|\vec{r}_{\text{rel}}(t)\|$. Recurrence plots colour scale: dark blue for $I = 0$, light yellow for maximum I .

Altogether, RP analysis suggests an intermittent relative dynamics, where dwelling at a certain preferred distance (as in behavioural phases \mathcal{S} and \mathcal{M}) alternates with

sudden relative motion bursts (behavioural phase \mathcal{R}), eventually leading the system back to such metastable relative distance but with generally different orientation of the cell-cargo couple.

An experimental estimation of both reorientation rate λ and time duration τ_{rev} has been performed over populations of cellular trucks, as described in Section 4.2.

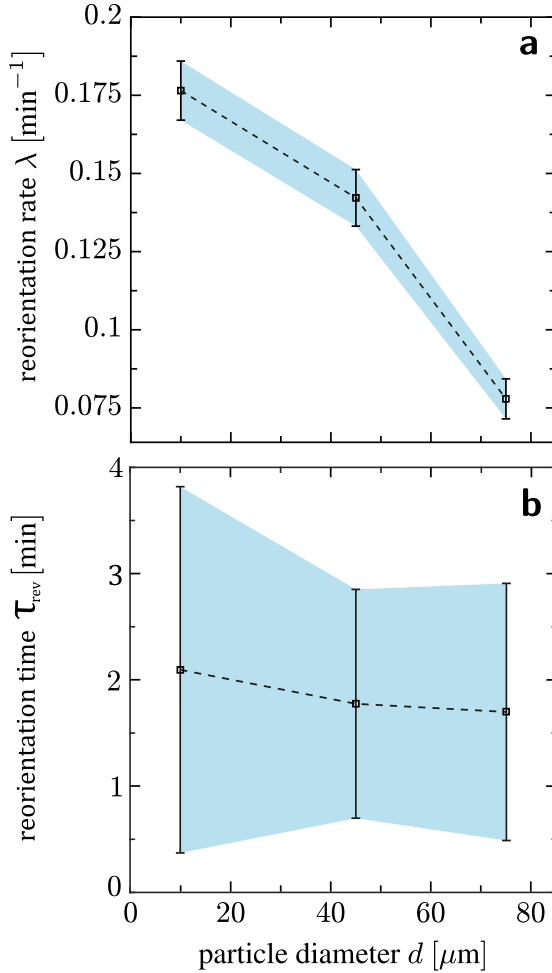


Figure 5.9: Statistics on occurrence rate and time duration of reorientation events, for the three tested particle sizes (10 μm , 45 μm and 75 μm). Each data point represents an estimate of expected value over a population of 10 cellular trucks, recorded for 45 to 60 min. Bars refer to standard deviation.

The ensemble-averaged statistical estimates $\hat{\lambda}$ reported a monotonic decrease with the particle diameter, as visible in figure 5.9a, supporting the evidence from single-system comparison.

No significant difference emerged for the typical time duration of the reorientation process (i. e. the time a truck dwells in phase \mathcal{R}) τ_{rev} when different particle sizes are being used (figure 5.9b), suggesting this time scale to be independent from cargo size, at least within the range of diameters tested. In fact, as a newly polarized cell is pulling the cargo over its body from front to back, one would expect the time it takes for an adhesion site to “flow” across the membrane, to be an intrinsic feature of the cell cytoskeleton mechanics: the latter connects to such bundles of transmembrane adhesive proteins (forming the so-called Actin foci [23, 161]), thus imposes displacement on them according to motor-induced contraction of the Actin network [139, 161]; as long as needed forces do not exceed motor capabilities, this dynamics would be dictated by the Actin flow and relatively independent by opposing forces from the cargo.

5.3 CHARACTERIZATION OF CELL-CARGO INTERACTION

Figure 5.10 compares estimates of probability density function $p(r_{\text{rel}}) = p(\|\vec{r} - \vec{R}\|)$ and effective pair interaction potential $\Phi(r_{\text{rel}})$, inferred as described in Section 4.2, for three cellular trucks loaded with different particle sizes.

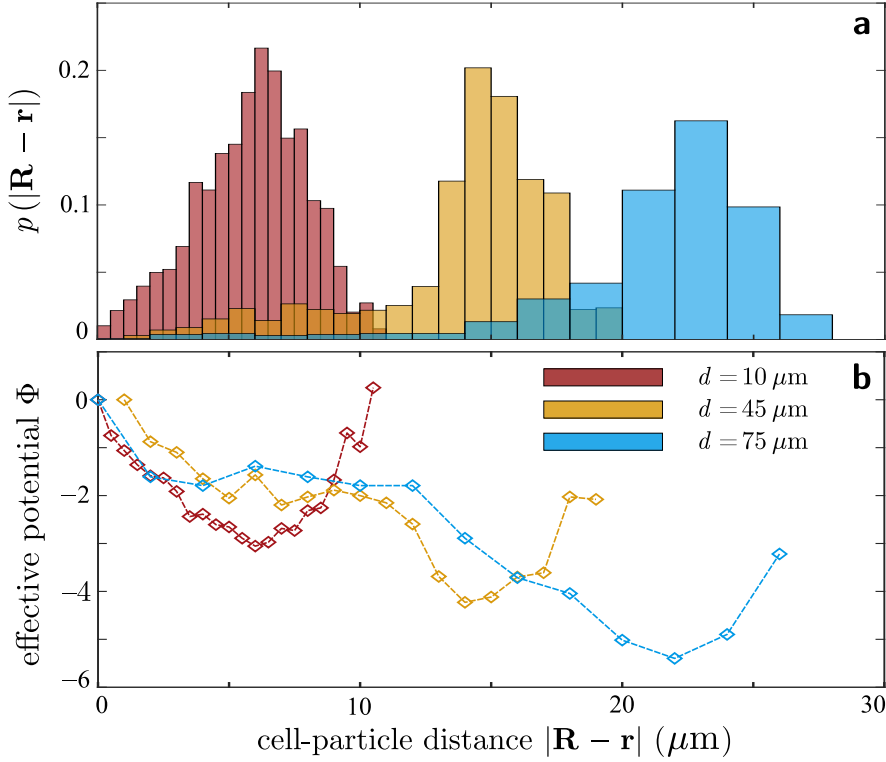


Figure 5.10: Estimates of probability density function for the cell-cargo relative distance, along with the inferred effective pair interaction potentials, for three cellular trucks loaded with particles of different size.

Distributions of probability for the relative distance consistently showed as markedly peaked distributions, for all tested cargo sizes, with a negative skew (i. e. left-tailed distributions) due to the reorientation events, as the cell suddenly moves away from a preferred relative distance and crosses underneath the particle, while pulling the latter towards its newly defined trailing edge.

Effective pair potentials revealed well-defined energy wells, locating farther and deeper as bigger cargoes are used. Intuitively, this makes it harder for a cell to crawl underneath the particle, implying, in turn, decreasing reorientation rates λ with cargo size, in line with the findings on cell-cargo relative dynamics discussed in the previous section.

Population-averaged probability distributions and pair potentials, shown in figure 5.11a-b, confirm the evidence collected for single cell-cargo systems, suggesting such probability and energy landscapes, together with their monotonic dependence on particle diameter, to be systematic and consistent among different cellular trucks.

Interestingly, the ensemble-averaged potentials disclosed a distinct harmonic form for the energy well close to the peak position, as highlighted in figure 5.11c. Here,

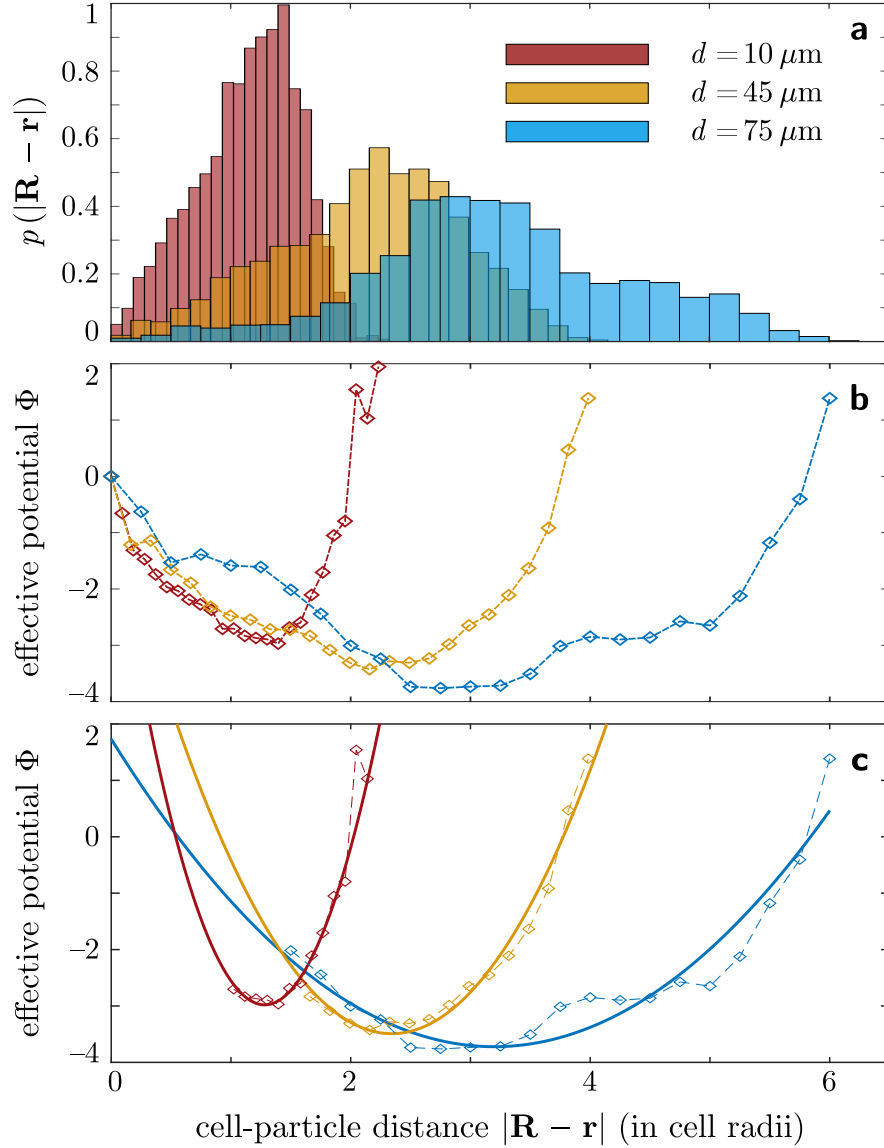


Figure 5.11: **a-b** Population-wide estimates of probability density function for the cell-cargo relative distance, along with the inferred effective pair interaction potentials. Each histogram has been obtained from a collection of 10 cellular trucks, recorded for 45 to 60 min, loaded with particles of a given size. In **c**, harmonic fit of the effective potential well for the three distinct populations. Here, the potential shape near the origin (left of the wells) is not being shown: it stems from the left tail of skewed distributions, reflecting the crossing dynamics during reorientation rather than motion around resting position (the energy well); hence, it is not considered in the fitting as the two parts have different physical meanings.

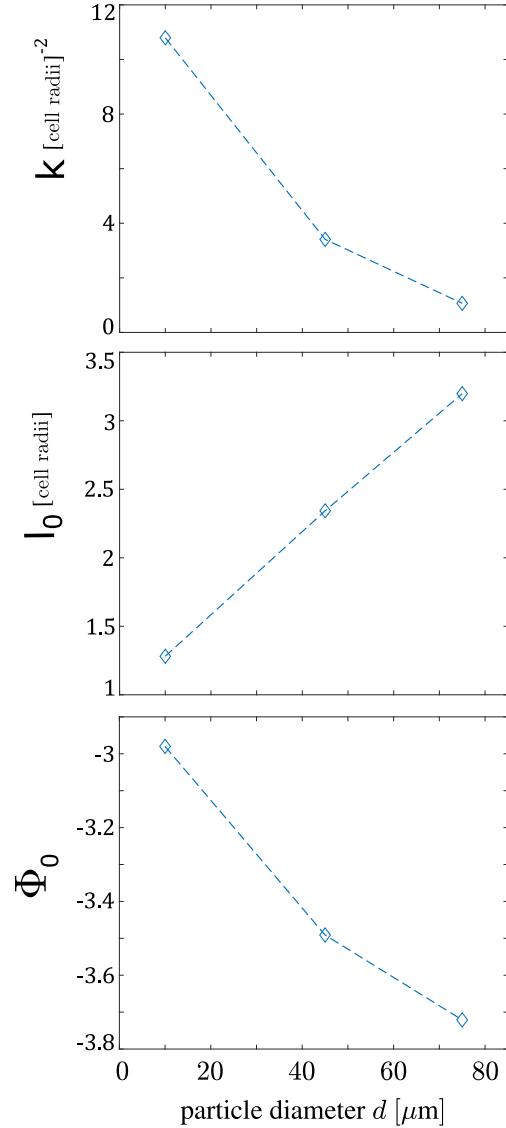
effective interaction potential wells have been fitted with the following second-order polynomial function:

$$\Phi(r_{\text{rel}}) = k(r_{\text{rel}} - l_0)^2 + \Phi_0$$

representing the functional form of an harmonic potential with k , l_0 and Φ_0 respectively the elastic spring constant, resting position and energy minimum.

As illustrated in figure 5.12, the fitting procedure suggests monotonic scaling with respect to cargo size for all three fitting parameters, quantitatively validating the evidence of farther and deeper interaction potential wells for the cell-cargo couple as bigger particles are used.

Figure 5.12: Harmonic fit parameters as function of cargo size, obtained from the fitting in figure 5.11c.



Overall, the outcomes from cell-cargo interaction analysis endorse a description of the convoluted cell-cargo relative motion as a Brownian-like random motion, confined around a resting position at distance l_0 by an harmonic potential well, during behavioural phases \mathcal{S} and \mathcal{M} ; upon cell repolarization (beginning of phase \mathcal{R}), such metastable relative position may switch to a newly defined location on the cell trailing edge, again at distance l_0 , thus driving the truck reorientation.

The relative dynamics analysis discussed in the previous section, besides agreeing with such idea as an intermittent behaviour is disclosed, allows to discern phases \mathcal{S} and \mathcal{M} , as the system shows more rotational noise while dwelling in phase \mathcal{S} : once cell polarity is lost, it is reasonable to consider the cargo resting position no more constrained with respect to the angular coordinate, given the temporary isotropy of the cell.

6.1 CONCEPT AND STRUCTURE OF THE MODEL

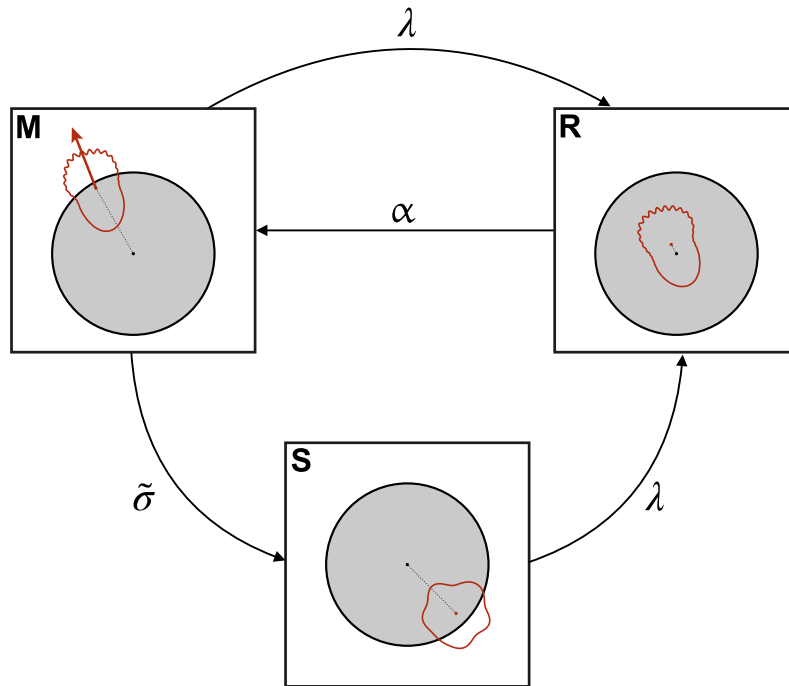


Figure 6.1: Markov chain for the coarse-grained physical model of a cellular truck, built upon the experimentally observed behavioural phases (see Section 5.1).

A first, straightforward way to model the motile behaviour of cellular trucks is to imagine it as an active Brownian particle (ABP) [91, 134], thus build a phenomenological model for self-propelled random motion upon the experimentally observed behavioural phases (the latter introduced in Section 5.1 and illustrated in figure 5.3). In fact, by assuming the occurrence of any behavioural phase a memory-less stochastic process, occurring with a probability depending solely from the phase previously attained, such phases directly translate in states of a Markov chain¹, which dictates the law of motion of the truck as a whole.

According to this idea, the two-body cell-cargo system is *coarse-grained* into a single particle, where the truck internal structure is reduced to a unit vector \vec{p} encoding for the truck orientation (namely, the cargo-to-cell axis). The effect of the truck internal dynamics on overall motility is, thus, explicitly embedded as an active term in a first order Langevin equation² for the motion of the cellular truck center of mass $\vec{x}(t)$ (i. e. the surrogate ABP).

¹ A Markov chain is a stochastic model, often depicted as a directed graph, describing a memory-less stochastic process as sequence of mutually exclusive events or states, occurring with probabilities depending solely from the state previously attained (namely, the Markov property) [58].

² See Section 2.1 for a brief introduction on Langevin equations.

Specifically:

$$\frac{d}{dt}\vec{x}(t) = v[s] \cdot \vec{p}[\phi(t)] + \sqrt{2D_{\text{int}}}\vec{\xi}_{\text{int}}(t) \quad (6.1)$$

where:

- $\sqrt{2D_{\text{int}}}\vec{\xi}_{\text{int}}(t)$ encodes for *intrinsic* randomness in truck motion, here simply treated as an additive Wiener process [46] perturbing cellular truck trajectories; explicitly, it consists of a Gaussian δ -correlated noise, with zero mean and standard deviation (i. e. noise amplitude) $\sqrt{2D_{\text{int}}}$.
- $v[s] \cdot \vec{p}[\phi(t)]$ represents the *active* term encoding for the peculiar intermittent dynamics of the cellular truck, and is therefore dependent on which behavioural phase the truck is at time t .

The three behavioural phases \mathcal{S} , \mathcal{R} and \mathcal{M} define a Markov chain, depicted in figure 6.1, which models the stochastic succession of distinct motility states for the surrogate ABP. Accordingly, such Markov chain governs the time evolution of the active term to reproduce the experimentally observed truck behaviours:

- The truck velocity $v[s]$ is treated as a dichotomous variable, with a switch s that makes it non-zero during phase \mathcal{M} only:

$$v[s] = \begin{cases} 0 & s = 1 \text{ (behavioural phases } \mathcal{S}, \mathcal{R}) \\ v_{\text{run}} & s = 2 \text{ (behavioural phase } \mathcal{M}) \end{cases} \quad (6.2)$$

- Every occurrence of phase \mathcal{R} is bound to trigger a random reorientation of the truck's polarity vector $\vec{p}[\phi(t)]$:

$$\mathcal{S} \rightarrow \mathcal{R} \vee \mathcal{M} \rightarrow \mathcal{R} \implies \phi \rightarrow \phi + \delta\phi$$

Transitions among states, emulating the occurrence of the distinct motile behaviours in a cellular truck, are assumed to be stochastically occurring with constant rates; hence, they are modelled as Poisson processes:

$$\begin{aligned} \mathcal{S} \rightarrow \mathcal{R} \vee \mathcal{M} \rightarrow \mathcal{R} &\sim \text{Pois}(\lambda) \\ \mathcal{R} \rightarrow \mathcal{M} &\sim \text{Pois}(\alpha) \\ \mathcal{M} \rightarrow \mathcal{S} &\sim \text{Pois}(\tilde{\sigma}) \end{aligned}$$

with $\lambda = \tau^{-1}$ and $\alpha = \tau_{\text{rev}}^{-1}$, respectively, rates of occurrence and completion (reciprocal of time duration i. e. dwelling time in state \mathcal{R}) of reorientation events (modelled by state \mathcal{R}), as defined in Section 5.1. The rate $\tilde{\sigma}$ is defined as the reciprocal of a time scale τ_{run} (dwelling time in state \mathcal{M}), describing intrinsic persistence in cytoskeletal polarity [62, 125]: it accounts for the lifetime of cell polarity observed after termination of the polarization-promoting stimulus (cargo being towards the front of a polarizing/polarized cell), namely, upon cell transiting under the particle (termination of phase \mathcal{R}).

6.2 MODEL PREDICTIONS

In order to investigate its Langevin dynamics and eventually make predictions on cellular truck spreading, I performed computer simulations of this coarse-grained truck model by numerical integration of equation (6.1), as discussed in Section 4.3.

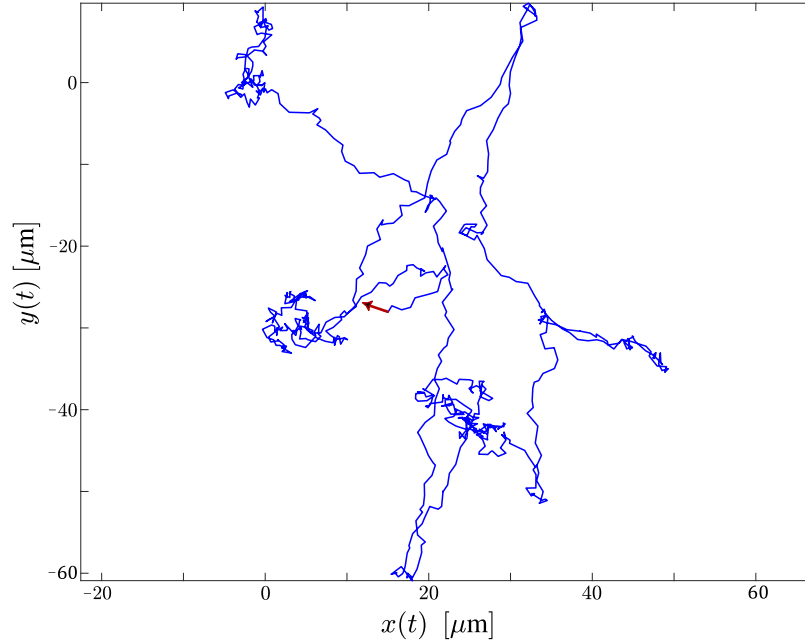


Figure 6.2: A cellular truck trajectory I simulated according to the coarse-grained model (time duration 120 min). In red, truck orientation vector \vec{p} . Parameters set values: $\lambda = (5 \text{ min})^{-1}$, $\alpha = (2 \text{ min})^{-1}$, $\tilde{\sigma} = (6 \text{ min})^{-1}$, $v_{\text{run}} = 6 \mu\text{m min}^{-1}$, $D_{\text{int}} = 1 \mu\text{m}^2 \text{ min}^{-1}$, $\delta\phi \sim \text{Unif}(-\pi, \pi)$, time integration step $\Delta t = 0.1 \text{ min}$.

Experimentally measured values are adopted for all of the model parameters. The velocity v_{run} of a persistently moving truck (state \mathcal{M}) identifies with the average speed of a *Dictyostelium discoideum* cell; thus, values between $4 \mu\text{m}$ and $10 \mu\text{m}$ have been used, according to literature [8] and in line with my measurements. As for the time scale τ_{run} , necessary to define the rate $\tilde{\sigma} = \tau_{\text{run}}^{-1}$, I tested a range of values between 4 min and 8 min obtained by simple observation from my recordings; such values of post-stimulus polarity lifetime comply with literature, as directional memory/persistence has been reported from $\sim 2 \text{ min}$ [62, 125] up to a few tens of minutes [63], depending on stimulus nature and dynamics, substrate geometry, and the quantitative definition of such biophysical feature adopted within the specific experimental context. The remaining parameters are derived from my analysis of cell-cargo behaviour and trajectories, as described through Chapter 5.

For the probability distribution of the truck reorientation angle $\delta\phi$, I adopted a uniform distribution $\delta\phi \sim \text{Unif}(-\pi, \pi)$: in fact, as discussed in Section 5.2, the noise in the relative motion plays a relevant role in randomizing the truck orientation among distinct reorientation events; being the truck internal configuration not resolved in this model, all information relative to this process is missing, therefore the choice of the uniform distribution being the least assumptive³.

³ A uniform probability distribution over the variable domain, for a finite domain, maximizes the information (or Shannon) entropy, therefore is the one with the least information content [37].

The model predicts a *diffusive long-time spreading dynamics* as the truck's ensemble-averaged Mean Squared Displacement ($\text{MSD}(t) = \langle \vec{x}(t)^2 \rangle_{\text{ens}}$), after an initial transitory, grows linear in time. This can be appreciated in figure 6.3a, which further highlights the dependence of the long-time truck diffusivity \mathcal{D} from the reorientation rate λ , as the steepness of this linear regime is affected by the value adopted for such rate.

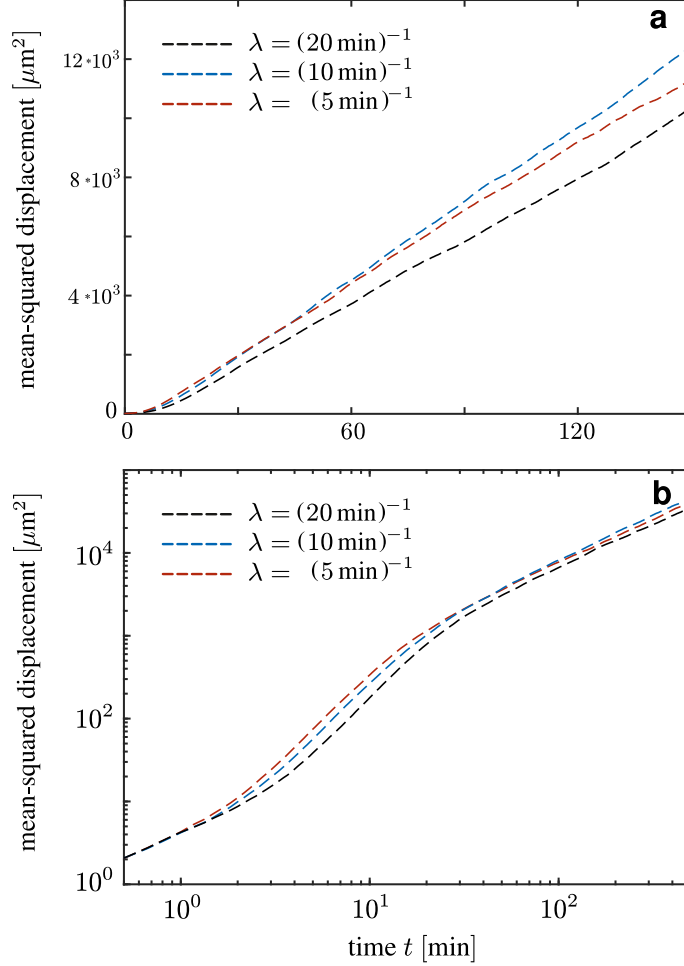


Figure 6.3: **a** linear and **b** logarithmic plot of the Mean Squared Displacement time evolution $\text{MSD}(t)$ of coarse-grained modelled cellular trucks, for three different values of reorientation rate λ . All the other parameters are set as in figure 6.2. Each curve stems from an ensemble average over 2500 simulated trucks. Simulations have been initialized with the trucks being in state \mathcal{S} .

Being the two terms of eqn. (6.1) additive and uncorrelated stochastic processes, it follows:

$$\begin{aligned} \langle \vec{x}(t)^2 \rangle &= \left\langle \left(\int_0^t v[s] \cdot \vec{p}[\phi(t)] dt + \int_0^t \sqrt{2D_{\text{int}}} \vec{\xi}_{\text{int}}(t) dt \right)^2 \right\rangle = \\ &= \left\langle \left(\int_0^t v[s] \cdot \vec{p}[\phi(t)] dt \right)^2 \right\rangle + \left\langle \left(\int_0^t \sqrt{2D_{\text{int}}} \vec{\xi}_{\text{int}}(t) dt \right)^2 \right\rangle + 0 = \\ &= \langle \vec{x}_{\text{act}}(t)^2 \rangle + \langle \vec{x}_{\text{int}}(t)^2 \rangle \end{aligned}$$

which means their contributions to the MSD are additive as well. As a consequence, the long-time diffusivity of the truck can be separated into two independent contributions: $\langle \vec{x}(t)^2 \rangle \sim 4\mathcal{D}(\lambda) t = 4(\mathcal{D}_{\text{act}}(\lambda) + D_{\text{int}})t$.

By plotting such MSD curves in logarithmic scale, the initial transitory can be better resolved and the different dynamical regimes are identified, as the curve steepness here reflects the scaling exponent. As shown in figure 6.3b, the system undergoes a distinctive spreading process, characterized by an initial diffusive dynamics which, within a time frame comparable with the time scale $\lambda^{-1} = \tau$, goes through an anomalous diffusion transient phase and eventually evolves back into a long-time diffusive regime.

The simulations are initialized with the trucks being in state \mathcal{S} , performing Brownian-like diffusion by the action of the Wiener process $\sqrt{2D_{\text{int}}}\vec{\xi}_{\text{int}}(t)$; this explains the initial linear scaling of the MSD(t) for small times. Within the characteristic lifetime of the \mathcal{S} state, namely λ^{-1} , a transition towards a faster scaling is in fact expected, as it accounts for the active persistent motion gradually triggering as trucks get through state \mathcal{R} and reach state \mathcal{M} . Eventually, the scaling becomes linear in the long-time limit, once the stochastic process of truck reorientation relaxes⁴.

Interestingly, the intermediate anomalous diffusion regime features a scaling exponent higher than one may naively expect. In fact, the active term in eqn. (6.1) drives ballistic runs for trucks in state \mathcal{M} , as it provides directed motion at constant velocity. For an object performing ballistic motion, the Mean Square Displacement is expected to grow quadratically with time ($\langle \vec{x}(t)^2 \rangle = v_{\text{run}}^2 t^2$); here, the presence of the noise $\sqrt{2D_{\text{int}}}\vec{\xi}_{\text{int}}(t)$ perturbs such ballistic runs with an additive contribution of pure diffusive nature, which may only decrease the scaling exponent (to an extent depending on the noise amplitude). Accordingly, one may expect the intermediate regime to be superdiffusive (scaling exponent between 1 and 2). However, as highlighted in figure 6.4a, simulations predict a faster scaling during this regime, with an exponent greater than 2.

This “super-ballistic” behaviour, referred to as hyperdiffusive [144], becomes clear once the overall population dynamics is taken into account. In fact, the trucks making an ensemble initially in state \mathcal{S} would not simultaneously reach state \mathcal{M} , but rather gradually as transitions between states are assumed to be Poissonian processes. Precisely, being ρ_i the fraction of systems in state i , trucks starting in state \mathcal{S} would leave the latter with constant rate

$$\frac{d}{dt}\rho_{\mathcal{S}} = -\lambda\rho_{\mathcal{S}}$$

building up a sub-population of systems in state \mathcal{R}

$$\frac{d}{dt}\rho_{\mathcal{R}} = \lambda\rho_{\mathcal{S}} - \alpha\rho_{\mathcal{R}} = \lambda e^{-\lambda t} - \alpha\rho_{\mathcal{R}}$$

From here, trucks would gradually switch to state \mathcal{M} , again with constant rate, leading to the following dynamics of ballistic motion triggering:

$$\begin{aligned} \frac{d}{dt}\rho_{\mathcal{M}} &\simeq \alpha\rho_{\mathcal{R}} = \alpha\left(\lambda e^{-\alpha t} \int_0^t e^{(\alpha-\lambda)t'} dt'\right) = \frac{\alpha\lambda}{\alpha-\lambda}\left(e^{-\lambda t} - e^{-\alpha t}\right) \\ \rightarrow \rho_{\mathcal{M}} &= \frac{1}{\alpha-\lambda}\left(\alpha(1 - e^{-\lambda t}) - \lambda(1 - e^{-\alpha t})\right) \end{aligned}$$

⁴ The recurrence of random reorientations over time randomizes the motion, back to a diffusive spreading. For an explanation of random walks relaxation, see Chapter 2.

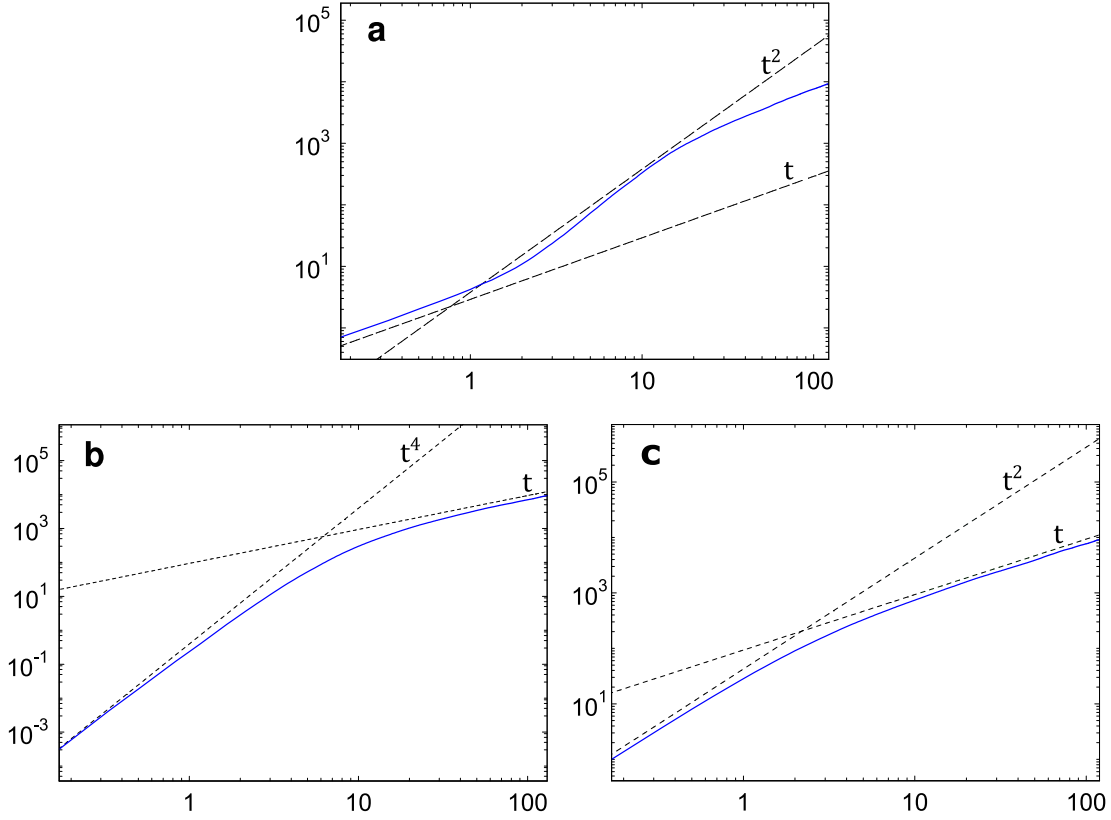


Figure 6.4: Logarithmic plot of the Mean Squared Displacement time evolution $\text{MSD}(t)$ of coarse-grained modelled cellular trucks, for three distinct cases: **a** simulations initialized in state \mathcal{S} ; **b** simulations initialized in state \mathcal{S} , but run with no noise ($D_{\text{int}} = 0$); **c** simulations initialized in state \mathcal{M} , no noise. All model parameters (except for D_{int} in panels b-c) are set as in figure 6.2. Each curve stems from an ensemble average over 2500 simulated trucks.

which goes as $t^2 + o(t^2)$. The ensemble-averaged Mean Squared Displacement will then grow as:

$$\langle \bar{x}(t)^2 \rangle_{\text{ens}} = \langle v^2 \rangle_{\text{ens}} t^2 + 4D_{\text{int}} t = v_{\text{run}}^2 \rho_{\mathcal{M}} \cdot t^2 + 4D_{\text{int}} \cdot t$$

where the first term (contribution of the active term) goes as $t^4 + o(t^4)$, and sums to the pure diffusive dynamics stemming from the noise $\sqrt{2D_{\text{int}}} \vec{\xi}_{\text{int}}(t)$ (second term). The scaling exponent is then expected to be between 1 and 4, in line with the intermediate scaling observed from simulations. Figure 6.4b confirms this argument, as simulations with no noise ($D_{\text{int}} = 0$) display a short-time hyperdiffusive regime with scaling exponent equal to 4, fading into the long-time diffusive dynamics.

It is thus revealed how, even though each single truck is either non-motile or ballistic, the whole ensemble can manifest population-wide acceleration, depending on the initial condition. For comparison, analogous simulations initialized in state \mathcal{M} show no hyperdiffusive behaviour (figure 6.4c), with an initial ballistic regime (all trucks running ballistic) gradually evolving into the long-time diffusive dynamics.

In order to elucidate the impact of the reorientation rate λ , key feature of the cell-cargo system, on transport efficiency, I made predictions on the long-time diffusivity \mathcal{D} for a range of values of this parameter, hence sampling the curve $\mathcal{D}(\lambda)$.

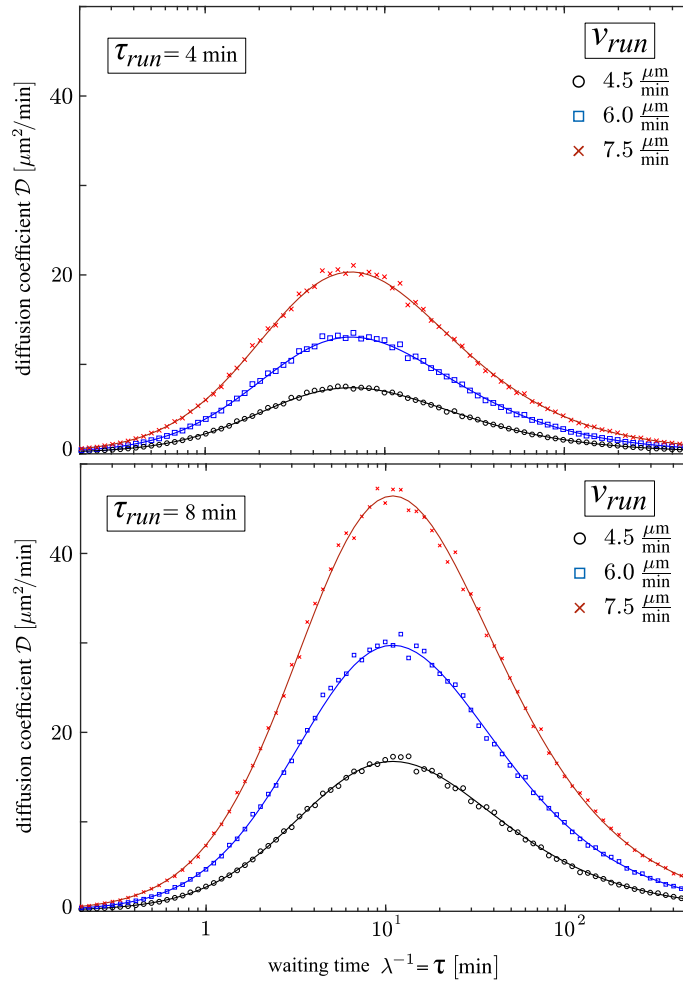


Figure 6.5: Curves of predicted long-time diffusivity $\mathcal{D}(\lambda)$ for a range of repolarization rates λ . Each curve refers to a different location in the parameter subspace $v_{run}-\tau_{run}$, pointing out the impact of cell biophysical properties on long-time transport. Solid lines represent analytical solutions (eqn. (6.3)), while markers numerical estimates. Values adopted for the remaining parameters are as in figure 6.2.

As it can be appreciated in figure 6.5, a non-monotonic dependence of \mathcal{D} on λ emerged, featuring a single peak located at rates close to $\tilde{\sigma} = \tau_{run}^{-1}$ (precisely, around $(\tau_{run} + \tau_{rev})^{-1}$). Regarding the curve dependence on cell intrinsic features, the polarity lifetime τ_{run} resulted to affect position as well as amplitude of the peak, while cell speed v_{run} regulates the amplitude only with no effect on functional shape.

Although such trend in long-time spreading may not seem intuitive at first, the physical mechanism behind its non-monotonicity and peak location can be easily grasped by means of a simple scaling argument.

In fact, two distinct time-scales are pivotal in determining the characteristic motile behaviour of cellular trucks: the average time interval between truck reorientations $\tau = \lambda^{-1}$, dictated by the rate at which the cell repolarizes towards the cargo and the truck reorients; the lifetime of persisting cell polarity $\tau_{run} = \tilde{\sigma}^{-1}$, which determines the average run time for the cellular truck after reorientation. To lowest order, one can write the estimate $\mathcal{D}_{act} \sim \frac{\langle l_{run}^2 \rangle}{\tau}$, where $\langle l_{run}^2 \rangle = (v_{run} T)^2$ is the mean square value of the distance run between two reorientation events, and T is the average time the system is

actually running before the next reorientation. In general T is different than τ , since a spontaneous decay of cell polarity may terminate the run before a new reorientation event occurs. Specifically, $T = \min(\tau, \tau_{\text{run}})$, and follows:

$$\mathcal{D}_{\text{act}} \propto \begin{cases} \tau & \tau \ll \tau_{\text{run}} \\ \tau^{-1} & \tau \gg \tau_{\text{run}} \end{cases}$$

which gives a diffusivity non-monotonic with respect to τ and peaked around τ_{run} , in agreement with simulations.

The presence of a finite time duration of the truck reorientation process $\tau_{\text{rev}} = \alpha^{-1}$ introduces a third time-scale, that changes the small τ (i.e. high λ) limit scaling and leads to the actual peak shape and position (now located at $(\tau_{\text{run}} + \tau_{\text{rev}})^{-1}$):

$$\mathcal{D}_{\text{act}} \sim \frac{\langle l_{\text{run}}^2 \rangle}{\tau + \tau_{\text{rev}}} \propto \begin{cases} \tau^2 & \tau \ll \tau_{\text{run}}, \tau_{\text{rev}} \\ \tau & \tau_{\text{rev}} < \tau < \tau_{\text{run}} \\ \tau^{-1} & \tau \gg \tau_{\text{run}}, \tau_{\text{rev}} \end{cases}$$

This outcome complies with the analytical solution for long-time spreading of a cellular truck, whose derivation by Dr. Robert Grossmann is presented in Appendix B: trucks are in fact expected to follow a diffusive dynamics in the long-time regime, with a diffusivity \mathcal{D} which assumes, for a simplified description of the truck as presented in this chapter, the following expression:

$$\begin{aligned} \mathcal{D} &= D_{\text{int}} + \frac{v_{\text{run}}^2}{2} \frac{\lambda}{(\lambda + \tilde{\sigma})^2} \frac{\alpha}{\alpha + \lambda} \cdot \frac{1}{1 - \langle \cos \delta \phi \rangle} \\ &= D_{\text{int}} + \frac{(v_{\text{run}} \cdot \tau_{\text{run}})^2}{2} \frac{\tau}{(\tau + \tau_{\text{run}})^2} \frac{1}{1 + \frac{\tau_{\text{rev}}}{\tau}} \cdot \frac{1}{1 - \langle \cos \delta \phi \rangle} \end{aligned} \quad (6.3)$$

plotted as solid line in figure 6.5.

A fundamental result is drawn by recalling that, while $\tilde{\sigma}$ is an intrinsic biophysical feature of the cell, λ stems from the peculiar relative motion dynamics hence represents information on cell-cargo interaction.

Such reorientation rate decreases monotonically with particle diameter, according to my experimental findings (see Section 5.2); consequently, *an optimal particle size for cell-driven transport is predicted*: smaller particles cause frequent reorientations thus prematurely stopping the runs in between; on the other hand, bigger particles let the cell-cargo system dwell into a non-polar, non-motile state which is inefficient for transport.

Surprisingly, predictions are in line with independent experimental observations from O. Nagel [107], which suggested a similar trend for the effective truck diffusivity with respect to the particle diameter (see Section 1.3). Moreover, my simulations returned realistic values of truck diffusivity, comparable with the estimates from O. Nagel, and located its maximum near the value of λ I experimentally measured for 45 μm diameter particles, which consistently showed faster spreading in O. Nagel experiments.

In conclusion, coarse-grained modeling of cellular trucks based on observed behavioural phases, even though simplistic, grasps the key aspects of cellular truck motion, allowing predictions on spreading dynamics and long-time mass transport.

7.1 ANATOMY OF THE MODEL

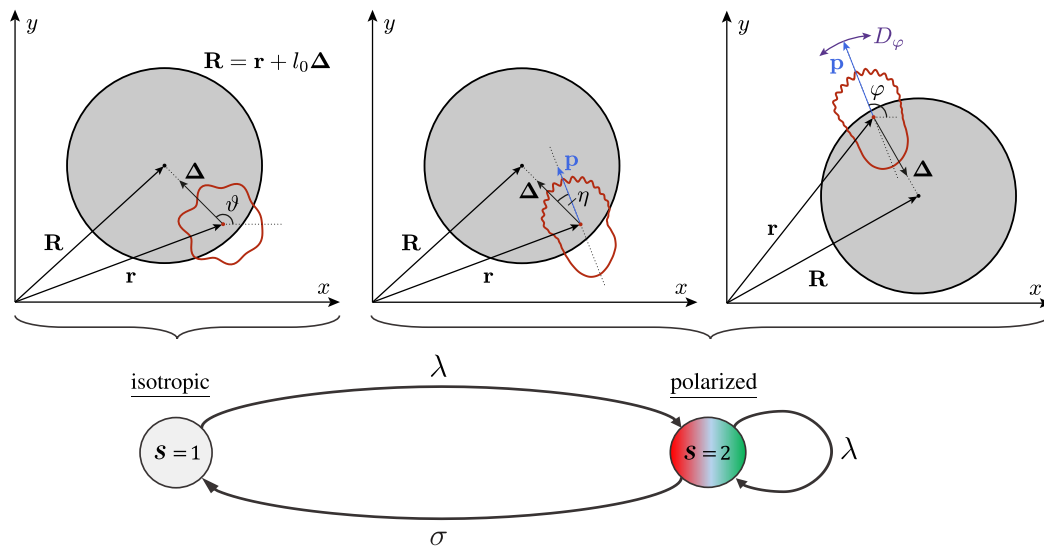


Figure 7.1: Schematic illustration of the full-scale model's key elements: the particle (cargo), the cell (active carrier) and the Markov chain governing the motile behaviour of the latter. The **top** three panels depict the configuration of the cell-cargo couple, together with related geometric quantities (see main text), during the three distinct behavioural phases (from left to right, phases S , \mathcal{R} and \mathcal{M}) manifested by the cellular truck as a whole. **Below**, the Markov chain encoding for the alternation between non-polar and polar biophysical states of the cell, which dictates its intermittent motion. Brackets evidence the link between the truck's behavioural phases and the correspondent state attained by the cell.

The phenomenological physical model discussed in the previous chapter, referred to as coarse-grained model, shed light on pivotal mechanisms governing the mass transport of cellular trucks, bridging the dynamics within the cell cargo system with the long-time spreading of the truck as a whole.

Notwithstanding, such model is by its nature unable to fully represent cellular truck motility: being the two bodies making up a cell-cargo system coarse-grained into a single entity, the internal structure of the truck is not resolved, as it is not the convoluted motion dynamics at spatial scales comparable to truck size; this makes intrinsically impossible to reproduce the relative cell-cargo dynamics and the fine structure of cellular truck trajectories.

To address this issue, I developed a fully resolved, or *full-scale*, phenomenological physical model of the cellular truck, as an evolution of the model previously discussed. Here, cell and particle are treated as distinct bodies, and their motion is resolved separately.

The cell, being the active element of the truck responsible for transport, is modeled as an active Brownian particle (ABP) [91, 134]. Specifically, its position $\vec{r}(t)$ is assumed to evolve in time according to the following first order Langevin equation¹:

$$\frac{d}{dt}\vec{r}(t) = v[s] \cdot \vec{p}[\varphi(t)] + \sqrt{2D}\vec{\xi}_r(t) \quad (7.1)$$

which consists of two additive stochastic processes:

- A Wiener process [46] $\sqrt{2D}\vec{\xi}_r(t)$ exemplifies non-persistent random displacement of a cell; explicitly, it consists of a Gaussian δ -correlated noise, with zero mean and standard deviation (i. e. noise amplitude) $\sqrt{2D}$.
- An active term $v[s] \cdot \vec{p}[\varphi(t)]$ introduces intermittency in the cell motion; it accounts for phases of persistent motility, with directionality dictated by the cell polarity vector \vec{p} .

The behaviour of this cell surrogate ABP is set to be governed by the 2-state Markov chain in figure 7.1, built upon experimental evidence on amoeboid motion (see Section 1.3) and in line with my observations (Section 5.1). Specifically, a cell may attain two distinct motility states:

$s=1$ *Isotropic state*. This state describes a cell in the absence of cytoskeletal polarization, characterized by non-persistent low motility. Accordingly, $v[s=1] = 0$, and displacements of the ABP stem exclusively from the Wiener process.

$s=2$ *Polarized state*. It models the persistent highly motile behaviour of polarized cells, i. e. cells whose cytoskeleton is arranged in a typical asymmetric configuration featuring a leading front edge and a trailing rear. The direction of cytoskeletal polarization is encoded in the cell polarity vector \vec{p} ; $v[s=2] = v_{\text{run}} \neq 0$ and the active term in eqn. (7.1) provides transient bursts of motility with directional persistency.

A polarized cell would eventually *repolarize* towards a new direction

$$\{s=2, \vec{p}[\varphi]\} \rightarrow \{s=2, \vec{p}[\varphi']\}$$

or *lose polarity* prior to the next repolarization

$$\{s=2, \vec{p}[\varphi]\} \rightarrow \{s=1\} \rightarrow \{s=2, \vec{p}[\varphi']\}$$

This translates in the Markov chain connectivity illustrated in figure 7.1. The stochastic occurring of such events is assumed to be Poissonian:

$$\begin{aligned} s = (1 \vee 2) \rightarrow 2 &\sim \text{Pois}(\lambda) \\ s = 2 \rightarrow 1 &\sim \text{Pois}(\sigma) \end{aligned}$$

As discussed in Section 5.1, events of cell repolarization within a cell-cargo system are intrinsically associated to the occurrence of cellular truck reorientations (behavioural phase \mathcal{R}). Consistently, the repolarization rate identifies with the reorientation rate $\lambda = \tau^{-1}$, as defined in Section 5.1 and analogous to the homonymous parameter in the coarse-grained model.

¹ See Section 2.1 for a brief introduction on Langevin equations.

The rate σ is here defined as reciprocal of the cell polarity lifetime, i. e. the average time a cell, within a cellular truck, dwells in a polarized configuration. According to the empirical findings discussed in Section 5.1, this time has to account for both behavioural phases \mathcal{R} (dwell time τ_{rev}) and \mathcal{M} (dwell time τ_{run}), leading to a rate $\sigma = (\tau_{\text{rev}} + \tau_{\text{run}})^{-1}$.

An additional Langevin equation $\frac{d}{dt}\varphi(t) = \sqrt{2D_\varphi}\xi_{,\varphi}(t)$ introduces some noise in the orientation of the cell's polarity vector $\vec{p}[\varphi(t)]$, allowing to set the degree of directional persistency during cell's polarized runs.

The particle represents a passive element, whose displacement is direct consequence of forces exerted by the cell. Following this argument, the cargo dynamics is described from the cell standpoint:

$$\vec{R} = \vec{r} + l_0 \vec{\Delta}$$

Here, the parameter l_0 identifies with the preferred value of cell-cargo relative distance discussed in Sections 5.1 and 5.2, and has been introduced in Section 5.3 as resting distance between mechanically interacting cell and cargo. The data analysis revealed its monotonic dependence with the cargo size, as bigger particles correspond to higher values of l_0 .

The normalized relative position vector $\vec{\Delta}$ encodes for the observed cell-cargo relative motion: it should account for the relative distance fluctuations around l_0 , and for the recurrent bursts in relative motion associated to the behavioural phase \mathcal{R} . Consequently, the description of its dynamics $\vec{\Delta}(t)$ required the adoption of a proper phenomenological model for cell-cargo interaction.

As summarized at the end of Section 5.3, my experimental findings point towards a confined random motion of the particle within an harmonic-like potential well, at distance l_0 from the cell, whose location around the latter changes as the cell repolarizes.

Consistently, I adopted the following Langevin dynamics:

$$\frac{d}{dt}\vec{\Delta}(t) = -\alpha \left(\vec{\Delta}(t) - \vec{\Delta}_0[s] \right) + \sqrt{2D_\Delta} \vec{\xi}_{,\Delta}(t) \quad (7.2)$$

with the term $-\alpha \left(\vec{\Delta}(t) - \vec{\Delta}_0[s] \right)$ encoding for elastic interaction within the cell-cargo couple, and $\vec{\Delta}_0[s]$ representing the resting position of the cargo with respect to the cell.

As long as the cell is in an isotropic state (state $s = 1$), the cargo resting position is not constrained with respect to the relative angular coordinate, thus randomly moving around the cell at distance $\sim l_0$. At every occurrence of cell repolarization (state $s = 2$), the resting position vector flicks towards a newly defined location on the cell's trailing edge. Accordingly:

$$\vec{\Delta}_0[s] = \begin{cases} +\vec{e}_\Delta[\theta] = \frac{\vec{\Delta}(t)}{\|\vec{\Delta}(t)\|}, & s = 1 \\ -\vec{p}[\varphi], & s = 2 \end{cases}$$

Fluctuations in relative distance around l_0 are generated by the Wiener process $\sqrt{2D_\Delta}\vec{\xi}_{,\Delta}(t)$ in eqn. (7.2), which enables particle random motion within the potential well.

The characteristic pull of the cargo over the cell during the truck reorientation (cell repolarized $\Rightarrow s = 2$) is reproduced by the term $-\alpha \left(\vec{\Delta}(t) - \vec{\Delta}_0[2] \right)$, essentially an elastic force relocating the cargo towards the new resting position at $-l_0 \vec{p}$ from the cell. The parameter α (dimensionally $[\text{time}]^{-1}$) sets the time for such dynamics to relax², upon flicking of the resting position as the cell repolarizes. As a result, it is dictated by the observed time scale for the truck reorientation process τ_{rev} (dwell time of behavioural phases \mathcal{R}), playing a role analogous to the one of the homonymous rate $\alpha = \tau_{\text{rev}}^{-1}$ in the coarse-grained model.

The tendency of a cell to polarize towards the current position of the cargo (see Section 5.1) is described by an instantaneous reorientation of the cell polarity vector:

$$\vec{p}(t) \rightarrow \mathcal{R}(\eta) \cdot \vec{e}_\Delta[\theta(t)] = \begin{pmatrix} \cos[\theta(t) + \eta] \\ \sin[\theta(t) + \eta] \end{pmatrix}$$

where $\mathcal{R}(\eta)$ is a rotation matrix around a random angle η following a Gaussian probability density function $g(\eta)$ centred at $\eta = 0$.

In conclusion, the full-scale model here presented serves as a more detailed physical description of the cellular truck.

Compared to the coarse grained model, no assumptions on truck behaviour are hardcoded into the Markov chain of the ABP, as the latter simply describes general features of amoeboid motile behaviour. The variable s here refers to the motile state of the cell only (persistent motion when cell polarized, as in behavioural phases \mathcal{R} and \mathcal{M}), unlike for the coarse-grained model where it acted as motility switch for the whole truck (persistently moving only during behavioural phase \mathcal{M} by definition). Figure 7.1 graphically shows this concept.

The truck internal dynamics is dictated by a physical model for cell-cargo interaction, derived from the analyses discussed in Sections 5.2 and 5.3.

7.2 *in-silico* MODEL TESTING

As for the coarse-grained model, I tested this more sophisticated physical model by means of numerical stochastic simulations, integrating its Langevin dynamics as described in Section 4.3.

Again, all parameters are set to realistic values, either experimentally measured by me or taken from literature. See the related discussion in the first page of Section 6.2 for more details.

Simulations could reproduce the motion of the cell as well as of the particle it carries, providing trajectories with a realistic fine structure.

As for the real system, “virtual” cellular trucks exhibited intermittent motion, where phases of low cell motility and random relative motion are interrupted by recurring transient directed runs, featuring the cell in a polarized, persistently moving state which pulls the particle forward.

² As it can be appreciated from eqn. (7.2), α represents the ratio between an elastic constant and a friction coefficient.

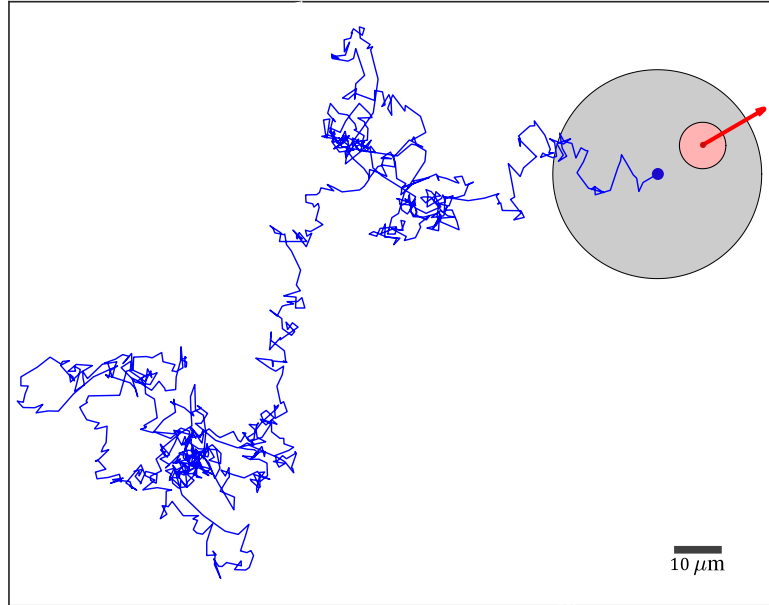


Figure 7.2: An example of cellular truck dynamics I simulated according to the full scale model, for a time duration of 100 min. Here, the virtual cell (in light red, with polarity vector \vec{p} in red) is loaded with a virtual particle (gray, trajectory in blue) of $45 \mu\text{m}$ diameter, hence a repolarization rate $\lambda = 0.1422 \text{ min}^{-1}$ and a resting distance $l_0 = 16 \mu\text{m}$ are used, conforming to experimental observations (Section 5.2). The values adopted for the other parameters are: $v_{\text{run}} = 6 \mu\text{m min}^{-1}$, $D = 1 \mu\text{m}^2 \text{ min}^{-1}$, $\sigma = 0.1 \text{ min}^{-1}$, $D_\varphi = 0.1 \text{ min}^{-1}$, $\alpha = 2 \text{ min}^{-1}$, $D_\Delta = 0.04 \text{ min}^{-1}$, $\eta \sim N(0, 0.2)$, time integration step $\Delta t = 0.1 \text{ min}$.

The same behavioural phases observed experimentally (see Section 5.1), spontaneously emerged here, as in the example shown in figure 7.3.

These outcomes witness faithfulness of the physics embedded into this model to the actual behaviour of a cellular truck.

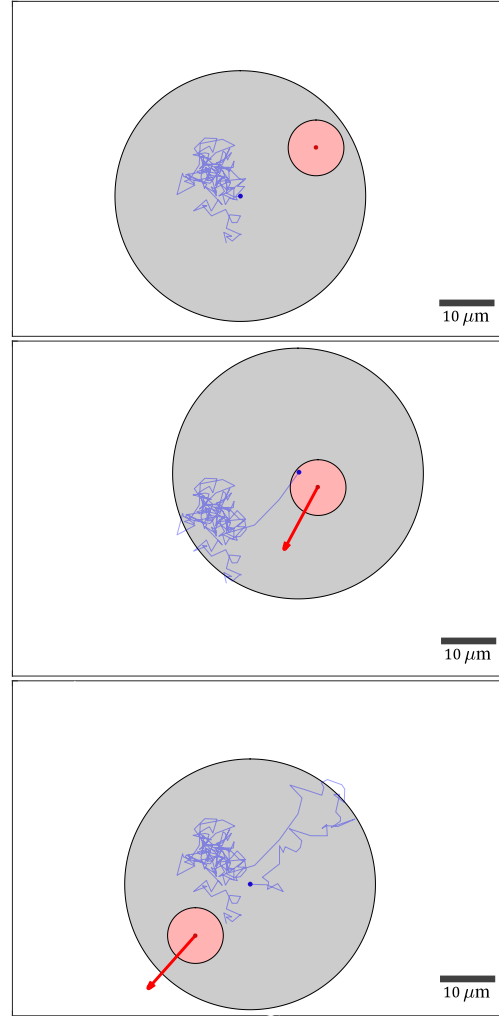
Likewise, the affinity between physical model and real system extends to a higher level of detail, as the two-body cell-particle dynamics within the truck is quantitatively reproduced.

In fact, once the cell-cargo relative motion from full-scale model simulations is analysed, matching dynamical features emerge, corroborating the model performances beyond a merely qualitative similarity.

Time series of the relative distance display the same characteristic intermittent dynamics, with recurring pronounced downward spikes perturbing the fluctuations around a typical distance l_0 . Consistently, such spikes correspond to repolarization events during which the cell pulls the cargo from its leading to the trailing edge. The associated relative distance histograms reveal a negatively skewed distribution with a pronounced peak, conforming to distributions from experimental data. Relative trajectories extracted from simulations retain the typical shape emerging from experiment, approximately circular with occasional crossings due to cell repolarization. In addition, the corresponding recurrence plots consistently display a checkerboard structure, akin to the dynamical pattern manifested by the real system.

Figure 7.4 provides a direct simulation-versus-experiment visual comparison.

Figure 7.3: Emergence of the three experimentally observed behavioural phases within full-scale numerical simulations. From top to bottom panel: phase \mathcal{S} (time t , cell in a non-polar low motility state, randomly displacing the cargo), phase \mathcal{R} (time $t + 1$ min, cell polarizes and moves persistently towards the current location of the cargo, while pulling the latter towards its rear), phase \mathcal{M} (time $t + 5$ min, cell still polarized, carrying the cargo by acting as a puller). The time instants shown here belong to the same simulation as in figure 7.2.



Concerning predictions on mass transport, the full-scale model exhibits a spreading dynamics consistent to the one of the coarse-grained model, with an initial diffusive dynamics followed by an anomalous diffusion transient, unfolding at a time scale comparable to $\lambda^{-1} = \tau$ and eventually leading to a long-time diffusive regime (Figure 7.5a).

In analogy to coarse-grained simulations, I initialized full-scale simulations with cells in isotropic, low-motile state $s = 1$, performing Brownian-like diffusion driven by the noise $\sqrt{2D} \vec{\xi}_r(t)$; such diffusive cell motion is relayed by the cell-cargo elastic interaction $-\alpha (\vec{\Delta}(t) - \vec{e}_\Delta)$ to the particle, hence providing a diffusive early-stage particle transport (initial linear scaling of the MSD(t) for small times). As cells start to polarize ($s = 2$, time scale τ), they drag their cargo via the force $-\alpha (\vec{\Delta}(t) + \vec{p}[\varphi])$, imposing a more persistent motion which translates in a different mass transport dynamics with faster MSD(t) scaling. Eventually, the scaling becomes linear again in the long-time limit, once the stochastic process of cell repolarization relaxes³.

Once more, estimates on long-time diffusivity predict a non-monotonic dependence from the repolarization rate λ , with curves $\mathcal{D}(\lambda)$ peaked at rates corresponding to

³ The recurrence of random reorientations over time randomizes the motion, back to a diffusive spreading. For an explanation of random walks relaxation, see Chapter 2.

$\sigma = (\tau_{\text{run}} + \tau_{\text{rev}})^{-1}$ (Figure 7.5b). As a result, an *optimal cargo size* maximizing long-time mass transport is again predicted, once the monotonic dependence of the rate λ from the particle diameter is taken into account (see Section 5.2). This finding is quantitatively consistent with coarse-grained model predictions, and suggests the same optimal value for λ (hence, the same optimal particle diameter $\sim 45 \mu\text{m}$).

As already mentioned in the previous Chapter while discussing the coarse-grained model predictions, an analytical solution for long-time spreading of a cellular truck has been proposed by Dr. Robert Grossmann, and its derivation is illustrated in Appendix B. It conforms with the diffusive long-time regime predicted by the simulations, and further provides an analytical expression for the long-time diffusivity \mathcal{D} :

$$\mathcal{D} = D + \frac{v_{\text{run}}^2}{2} \frac{\lambda}{\lambda + \tilde{\sigma}} \frac{\alpha}{\alpha + \lambda} \cdot \frac{D_{\Delta} + \lambda}{(D_{\Delta} + \lambda) \cdot (D_{\varphi} + \lambda + \tilde{\sigma} + \lambda g_1) + \tilde{\sigma} \lambda g_1} \quad (7.3)$$

with $\tilde{\sigma} = \tau_{\text{run}}^{-1}$ and $g_1 = \int_{-\pi}^{\pi} \cos(\eta) g(\eta) d\eta$ first Fourier coefficient of the probability density function $g(\eta)$ for the random contribution η to the repolarization angle.

A comparison between eqn. (7.3) and its counterpart for the coarse-grained model diffusivity (eqn. (6.3)) pinpoints the equivalence between the two models in terms of long-time mass transport predictions, as the coarse grained analytical solution is nothing but eqn. (7.3) applied to a particular, simplified case⁴.

This long-time convergence between the two models stems from the empirical fact that the cell-cargo relative motion affects transport in two ways: it dictates the trajectory fine structure, which is not relevant for transport in the long-time limit, and determines the direction the cell reorients to upon repolarization. It follows that, as long as proper stochasticity is embedded into the reorientation $\delta\phi$ of the coarse-grained ABP truck, the latter will spread as the full-scale model in the long-time regime.

As confirmation, one may coarse-grain the full-scale model based on its manifested behavioural phases (figure 7.3), which are the same shown by the real system, ending with a coarse-grained model equivalent to the one described in the previous chapter. In fact, the analytical solution for long-time spreading of cellular trucks has been derived in Appendix B by partial coarse-graining, yet it acts as a general solution perfectly matching with both coarse-grained and full-scale simulations.

In conclusion, the full-scale physical model presented and discussed in this chapter, while performing as well as the coarse-grained one in providing realistic predictions on long-time spreading dynamics, further succeeds in emulating the convoluted cell-cargo relative motion, thus reproducing the random motion of cellular trucks down to spatial scales comparable to the truck size.

The emergence of the same behavioural phases and dynamical patterns of relative motion as the real system, together with the consistent predictions on long-time mass transport, corroborates the fundamental hypotheses the model is built upon, and provides further insights on the role of cell-cargo interaction in the spreading process.

⁴ In fact, applying eqn. (7.3) to the coarse-grained model: $D = D_{\text{int}}; D_{\varphi} = 0$; the change of description of reorientations from $\varphi(t) \rightarrow \theta(t) + \eta$ to $\phi(t) \rightarrow \phi(t) + \delta\phi$ can be translated into $D_{\Delta} = 0$ and $\eta \sim \pi - \delta\phi \implies g_1 = -\langle \cos \delta\phi \rangle$. This indeed returns eqn. (6.3).

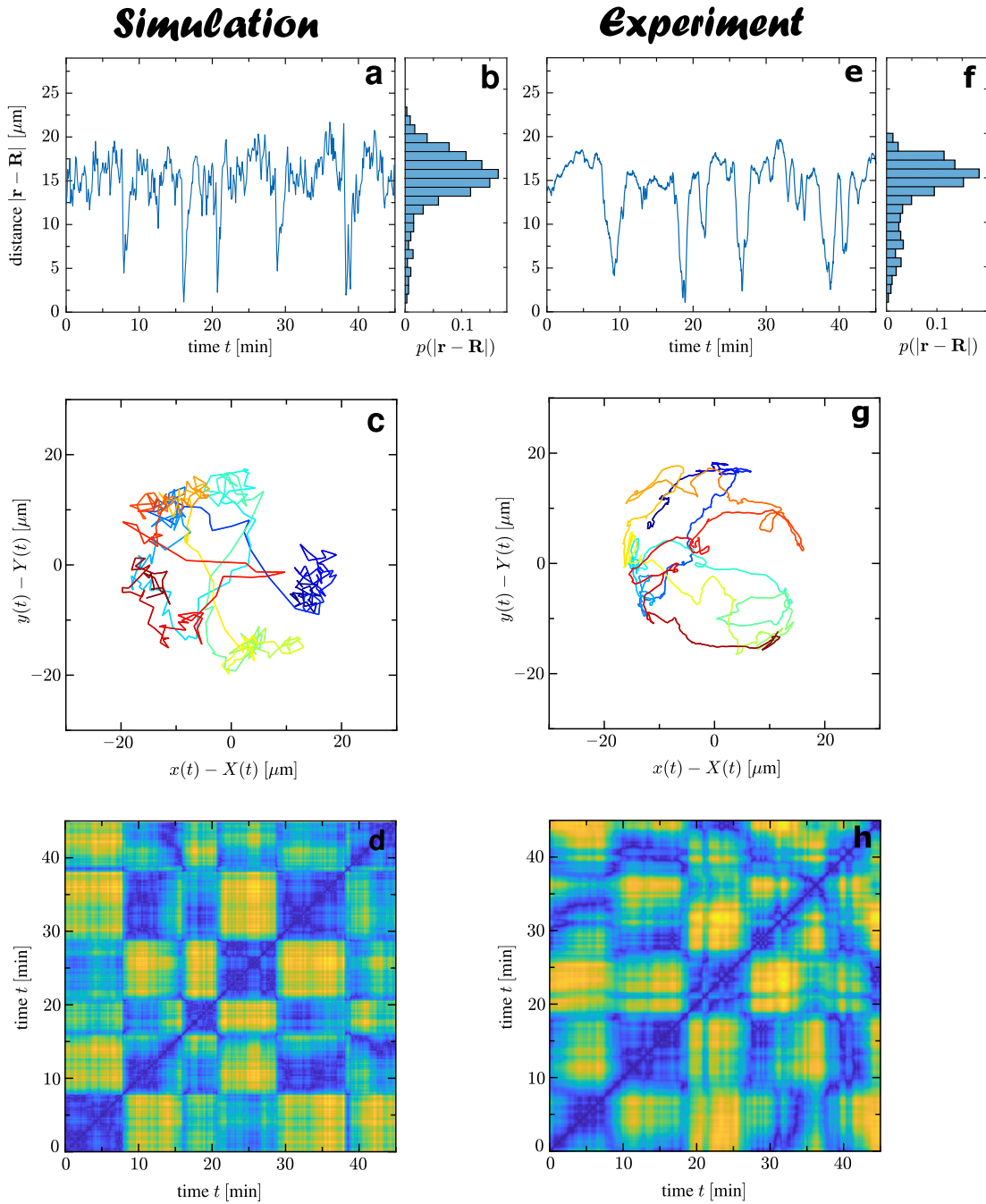


Figure 7.4: Visual comparison between the relative cell-cargo dynamics extracted from a full-scale numerical simulation (same simulation as in figures 7.2 and 7.3) and one extracted from an experimental recording (particle diameter 45 μm). **a** and **e** time series of relative distance; **b** and **f** histograms of relative distance; **c** and **g** relative trajectory of the cell ($\vec{r} - \vec{R}$, frame of reference centred with particle), with colour-coded time (from blue to red); **d** and **h** recurrence plots of the cell relative position $\vec{r}_{\text{rel}} = \vec{r} - \vec{R}$, where the similarity index $I(t_i, t_j) = \|\vec{r}_{\text{rel}}(t_i) - \vec{r}_{\text{rel}}(t_j)\|$ is colour-coded (dark blue for $I = 0$, light yellow for maximum I).

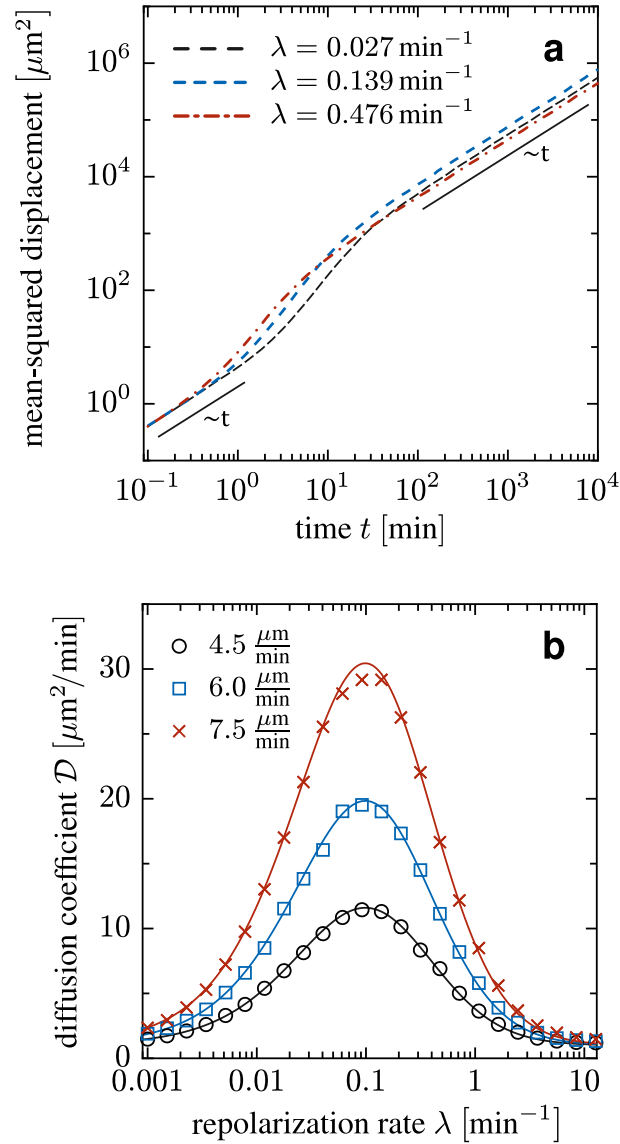


Figure 7.5: **a** Logarithmic plot of the MSD(t) for three different values of repolarization rates λ . All the other parameters are set as in figure 7.2. Each curve stems from an ensemble average over 2500 simulated trucks. Simulations have been initialized with the cell being in isotropic (non-polar) state $s = 1$. **b** Curves of predicted long-time diffusivity $\mathcal{D}(\lambda)$ for a range of repolarization rates λ . Each curve refers to a different value of the parameter v_{run} , to account for variability in cell velocity. Solid lines represent analytical solutions (eqn. (7.3)), while markers estimates from numerical simulations. Values adopted for the remaining parameters are as in figure 7.2.

FINAL CONCLUSIONS AND FUTURE PERSPECTIVES

In my doctoral project, I investigated the behaviour and transport mechanism of a novel kind of bio-hybrid system, referred to as *cellular truck*, which exploits the amoeboid motion of crawling cells to achieve active transport at the micro-scale.

I performed experiments that revealed a complex recurrent cell-cargo relative motion, together with an intermittent motion of the cellular truck as a whole. Particularly, I observed recurrent cellular polarization towards the cargo.

Combining diverse data analysis techniques, I suggest the presence of cargoes on amoeboid cells to act as mechanical stimulus leading cell polarization, thus promoting cell motility and giving rise to the observed intermittent dynamics of the truck. This is corroborated by state-of-the-art knowledge on the mechanics of amoeboid motility: in fact, the cell shape changes occurring during amoeboid crawling depend strongly on the adhesion pattern cells form with their surroundings; the presence of an additional confining structure as the cargo provides additional surface for adhesion, breaks the spatial symmetry and thereby promotes cell polarization. Such conclusion grants an explanation for the characteristic motility behaviour displayed by cellular trucks, and is further supported by the observed bursts in cytoskeletal polarity along the cell-cargo axis, whose rate of occurrence resulted dependent on cargo geometrical features as particle diameter.

In short, cell-cargo interactions play a main role in the emergent cellular truck motion dynamics. Particularly, they can determine the transport capabilities of amoeboid cells, as the cargo shape and size significantly impact the cytoskeletal activity and repolarization dynamics along the cell-cargo axis, the latter responsible for truck displacement and reorientation.

I furthermore developed a modelling framework, built upon the experimental evidence on truck behaviour, that connects the relative dynamics and interactions arising at the truck scale with the actual spatial dynamics and enables the prediction of the long-time transport properties of cellular trucks.

The theoretical analysis clarified the role of cell-cargo interaction on mass transport, unveiling in particular how the long-time transport efficiency is governed by the interplay between the persistence time of cell polarity – a time scale determined by intra-cellular processes – and time scales of the relative dynamics stemming from cell-cargo interaction.

Both suggested models – a simpler one, based on a coarse grained description of the cellular truck's manifested motion behaviour, and a more detailed version (full-scale model), which aims to account for the full spectrum of phenomenology – consistently predict the existence of an optimal cargo size, enhancing the diffusivity of cellular trucks.

Interestingly, such predictions are in line with previous independent experimental data [107], which suggested similar truck diffusivities and optimal cargo size. Notably, such independent data also reported loaded crawling cells to outperform unloaded ones in terms of their long-time transport efficiency, as they scored higher effective

diffusivities. This counterintuitive empirical evidence endorses, once more, the foundational idea of cargo promoting cell motility, consequence of the symmetry-breaking additional adhesion it provides.

In summary, my research work reveals the importance of cargo-carrier interactions in the context of crawling cell-mediated particle transport and provides a prototypical, multifaceted framework for the analysis and modelling of such complex yet to be explored bio-hybrid systems and their perspective optimization.

TOWARDS IN VIVO MULTICELLULAR TRANSPORT

On its way through a living organism towards a target site, a drug-loaded microparticle would likely interact with a multitude of cells, as it crosses the crowded micro-environments constituting most biological tissues. In addition, when the inflammatory/immune response is exploited as route of targeted drug delivery, the particle is expected to be manipulated by a stream of chemotactically migrating cells like neutrophils.

As discussed in Section 1.3, multicellular amoeboid cargo transport has been tested and proven to be successful for guided (chemotactic) transport; yet, prior to my work, it emerged as a seemingly inscrutable process, its high complexity hiding the underlying fundamental mechanisms of transport.

My findings paved the way towards a mechanistic understanding of such means of micro-transport, by shedding light on the processes governing single-celled amoeboid transport, and providing quantitative tools for its estimation and predictions. At this point, in order to address multicellular transport, the modelling framework I developed must be further extended, by incorporating additional laws accounting for *cell-cell interaction* and *force sharing*.

Regarding cell-cell interaction, I could sporadically observe it whenever, during a recording, a second cell approached by chance the cellular truck of interest. I noticed what seemed a short-range repulsive interaction, as cells had the tendency to reorient away from each other upon contact.

In fact, this type of behaviour has been already documented for eukaryotic crawling cells, and still draws the attention of the scientific community for its role in collective migration during physiological and pathological processes [29, 40, 178]. A possible next step could thus be to include an existing cell-cell repulsion model from literature.

More puzzling and unexplored is the inter-cellular force sharing, taking place as multiple cells pull on the same cargo.

During my doctoral work, I performed a few recordings of amoeboid cargo transport experiments using higher cell densities, collecting phenomenological evidence that can be classified in two main categories: in some cases, cells tend to gradually align to each other and successfully cooperate, pulling roughly towards the same direction thus granting net displacement of the shared cargo; conversely, a persisting mismatch of orientation among cells leads the latter to hinder each other, and cargo motion is stalled in a *Tug-of-War* of stochastic nature, where cells compete for particle transport.

A closer look at minimal tugs-of-war (two cells competing for one cargo) suggested a decisive role, on the fate of cargo displacement, for the maximal force a cell can exert on the particle: if cell alignment does not occur first, at some point one of the

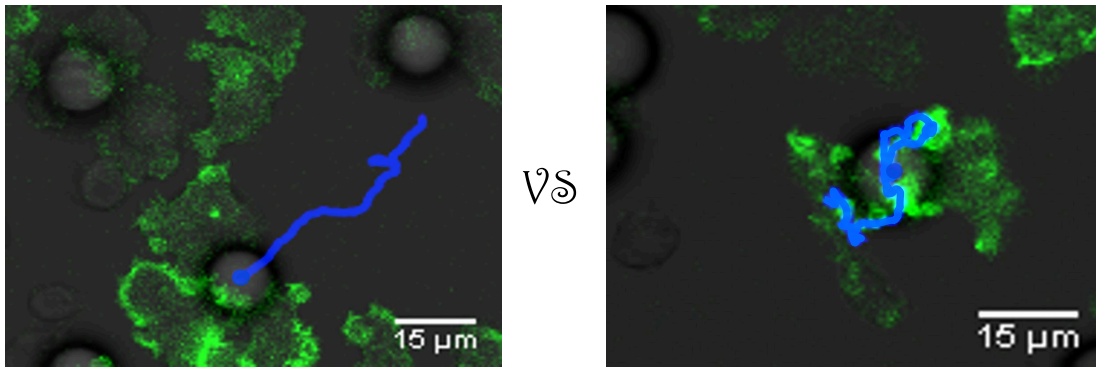


Figure 8.1: On the **left**, three cells pull a particle in a cooperative fashion, providing cargo transport (in blue, ~ 13 min recording of cargo trajectory). Conversely, in the example on the **right**, two cells pull the particle in roughly opposite directions, thus competing for the cargo; the latter is then stalled in a cellular tug-of-war, fluctuating around its position with no net displacement over time (in blue, ~ 20 min recording of cargo trajectory), as long as tug-of-war symmetry does not break.

two cells abruptly loses contact with the cargo and crawls away from it, hence letting the winning cell handle the cargo.

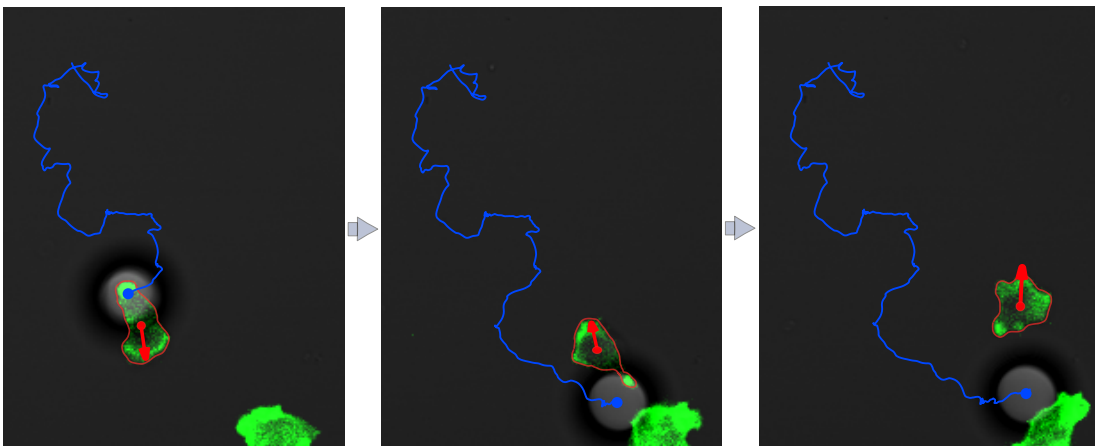


Figure 8.2: In the **left** panel, a cell is shown performing active cargo transport, as it pulls on a particle and provides motion (in blue, 27 min recording of cargo trajectory; in red, cell speed direction and boundary). Upon encountering a second cell, the carrying cell reorients away from it; however, the second cell had the chance to adhere onto the cargo, and its pull is now hindering the first cell from moving away with it (**central** panel, 10 min after left panel). It can be noticed how the first cell stretches under the internal reaction within the emerged tug-of-war, with one visible adhesion focus keeping hold onto the particle. Eventually, the tug-of-war resolves, in this case with the previous cargo carrier losing hold and crawling away (**right** panel, ~ 3 min after central panel).

Comprehensive physical modelling of multicellular transport requires, then, estimates of such maximal force, basically probing the effective interaction potential (discussed in Section 5.3) beyond its steep harmonic barrier.

Attempts on max force estimation have been carried out by Oliver Nagel, using optical tweezers to hinder the displacement of cargoes pulled by single cells; yet, they

resulted to be not strong enough (for laser intensities unharmed to the cell) to keep hold on the particle, and suggested maximal forces higher than 330 pN [107].

Here, I suggest to investigate the use of properly functionalized Atomic Force Microscopes to address such force estimates: by fixing the particle on the extremity of a tipless AFM cantilever, one may position the cargo on a cell and record forces by the latter exerted. This type of experimental setup may actually allow for a variety of different investigations, on cell-cargo interaction and cell motion under confinement, given the control over the cargo it provides.

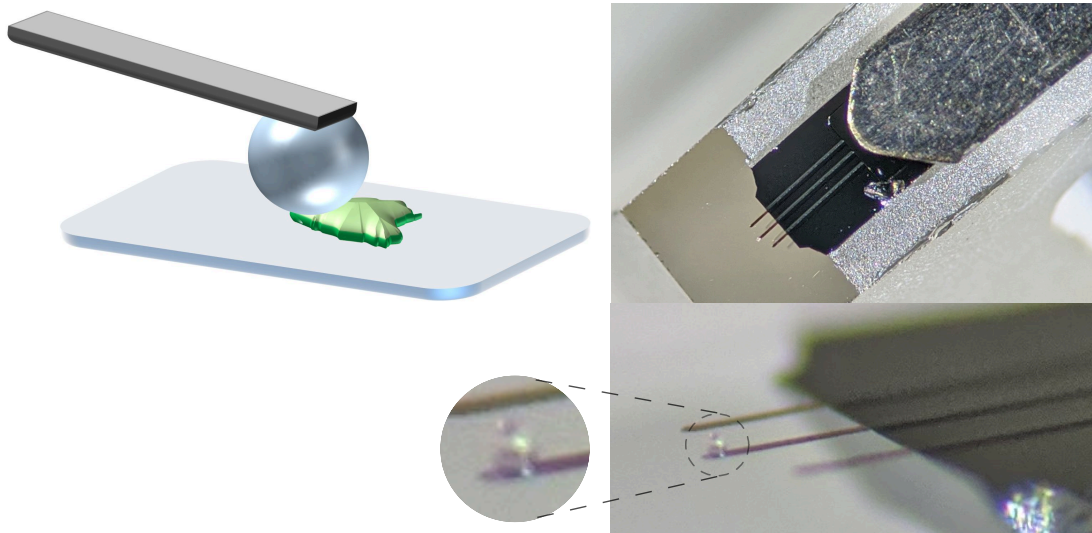


Figure 8.3: The illustration on the **left** depicts the spatial configuration of the proposed force measurement experiment, based on the use of an Atomic Force Microscope (AFM). The cell (in green) is put in contact with the particle, the latter fixed onto a cantilever controlled by an AFM: such instrument can work both as actuator (brings the cargo to the cell, and can impose forces/displacements) and as sensing device (can keep the cargo in a fix position by feedback loop control, while recording the reaction forces exerted). The panels on the **right** are pictures of an AFM cantilever functionalized with a $45\ \mu\text{m}$ diameter particle, that I realized as test of feasibility at Max Planck Institute of Colloids and Interfaces, hosted by the Mechano(bio)chemistry group (Dr. Kerstin Blank), upon suggestion of Prof. Dr. Reinhard Lipowsky. The cantilever has been imaged by reflected white light through a stereo microscope, while lying upside-down clamped to a support. Of the three visible cantilevers, the central is the only functionalized, being $350 \pm 5\ \mu\text{m}$ long and $35 \pm 3\ \mu\text{m}$ wide, $2 \pm 0.5\ \mu\text{m}$ thick. The lower panel is a higher magnified side view, with close-up on the particle.

Finally, including chemotactic cell behaviour in the model would close the gap towards the description of *in vivo* cargo transport, so to reproduce guided cellular transport.

Part IV

APPENDIX



MAXIMUM LIKELIHOOD-BASED ESTIMATION OF POISSONIAN RATES

For a Poisson process $n(t) \sim \text{Pois}(\lambda)$, the probability $P_n(T)$ of counting n events within a time frame T is equal to:

$$P_n(T) = \frac{(\lambda T)^n e^{-\lambda T}}{n!}$$

Thus, for a set of S independent measurements, each lasting for a time T_s , the likelihood \mathcal{L} of observing a sequence of counts n_s will be:

$$\mathcal{L} = \prod_{s=1}^S P_{n_s}(T_s) = \prod_{s=1}^S \frac{(\lambda T_s)^{n_s} e^{-\lambda T_s}}{n_s!}$$

If a Poisson process of unknown rate λ yields such sequence of counts n_s , the rate parameter can be estimated by adopting a paradigm of *maximum likelihood*, i. e. by finding the value for λ that maximizes the likelihood $\mathcal{L}(\lambda)$.

Since the logarithm is a monotonically increasing function of its argument, one may as well find the maximum for $\log \mathcal{L}$:

$$\log \mathcal{L} = \sum_{s=1}^S \log \left[\frac{(\lambda T_s)^{n_s} e^{-\lambda T_s}}{n_s!} \right] = \sum_{s=1}^S \left(n_s \log(\lambda T_s) - \lambda T_s - \log(n_s!) \right)$$

that is:

$$\begin{aligned} \frac{\partial \log \mathcal{L}}{\partial \lambda} &= \sum_{s=1}^S \left(n_s \frac{1}{\lambda} - T_s \right) = \frac{1}{\lambda} \sum_{s=1}^S n_s - \sum_{s=1}^S T_s \\ \frac{\partial \log \mathcal{L}}{\partial \lambda} = 0 &\implies \hat{\lambda} = \frac{\sum_s n_s}{\sum_s T_s} \end{aligned}$$

An estimate of standard deviation for the rate can be found by describing $\log \mathcal{L}$ near the maximum location $\hat{\lambda}$ with a second order expansion:

$$\begin{aligned} \frac{\partial^2 \log \mathcal{L}}{\partial \lambda^2} &= -\frac{1}{\lambda^2} \sum_{s=1}^S n_s \\ \implies \log \mathcal{L} &\simeq \text{const.} - \frac{1}{2} \frac{\sum_{s=1}^S n_s}{\hat{\lambda}^2} (\lambda - \hat{\lambda})^2 \implies \mathcal{L} \simeq e^{-\frac{1}{2} \frac{(\lambda - \hat{\lambda})^2}{\hat{\lambda}^2 / \sum_{s=1}^S n_s}} \\ \implies \sigma_{\hat{\lambda}} &= \frac{\hat{\lambda}}{\sqrt{\sum_s n_s}} \end{aligned}$$

In conclusion:

$$\boxed{\begin{aligned} \hat{\lambda} &= \frac{\sum_s n_s}{\sum_s T_s} \\ \sigma_{\hat{\lambda}} &= \frac{\hat{\lambda}}{\sqrt{\sum_s n_s}} \end{aligned}}$$

B

DERIVATION OF A FOKKER-PLANCK EQUATION FOR CELLULAR TRUCKS

The analytical derivation here presented has been obtained by my colleague Dr. Robert Grossmann, who I sincerely thank for this contribution to my research.

SIMPLIFIED TWO-STATE DESCRIPTION

A first theoretical estimation of the long-time dynamics of cellular trucks, based on the physical model described in Section 7.1, can be obtained by assuming the following simplifications: (i) in the isotropic state, the cell undergoes Brownian diffusion while the cargo is located at a fixed distance from the cell, performing random motion around it; (ii) in the polarized state, the cell performs a persistent random walk with a fixed speed v_{run} and a finite persistence length parametrized by the angular noise strength D_φ , carrying the cargo on its back; (iii) events of truck reorientation – where the cell tunnels underneath the cargo – are assumed to be fast processes compared to other relevant timescales and are therefore assumed to occur instantaneously. This corresponds, formally, to the limit $\alpha \rightarrow \infty$, implying that we neglect the timescale of the relative dynamics of cell and particle. A refined version of this derivation, taking the finite reorientation timescale $\tau_{\text{rev}} = \alpha^{-1}$ into account, is discussed afterwards.

The simplified version of the Langevin model is mathematically reflected by the following two coupled Master equations for the probability densities $P_{1,2}$ to find a particle in state 1 (isotropic state) and 2 (polarized state), respectively:

$$\partial_t P_1(\vec{r}, \theta, t) = D_i \Delta P_1 + D_\Delta \partial_\theta^2 P_1 - \lambda P_1 + \sigma P_2(\vec{r}, \theta - \pi, t), \quad (\text{B.1a})$$

$$\begin{aligned} \partial_t P_2(\vec{r}, \varphi, t) = & D_p \Delta P_2 + D_\varphi \partial_\varphi^2 P_2 - v_{\text{run}} \vec{p}[\varphi] \cdot \nabla P_2 - (\lambda + \sigma) P_2 \\ & + \lambda \int_{-\pi}^{\pi} d\theta g(\varphi - \theta) [P_1(\vec{r}, \theta, t) + P_2(\vec{r}, \theta - \pi, t)]. \end{aligned} \quad (\text{B.1b})$$

The vector \vec{r} indicates the position of the cell at time t . We note, however, that the long-time diffusion of cell and cargo is identical as they form a bound pair.

The observed dynamics of the cell-cargo truck at short timescales can be bridged with its long-time diffusion by integrating out irrelevant, fast processes. This is achieved by Fourier transform with respect to the angular variables via

$$f_1^{(n)}(\vec{r}, t) = \int_{-\pi}^{\pi} d\theta e^{in\theta} P_1(\vec{r}, \theta, t), \quad (\text{B.2a})$$

$$f_2^{(n)}(\vec{r}, t) = \int_{-\pi}^{\pi} d\varphi e^{in\varphi} P_2(\vec{r}, \varphi, t). \quad (\text{B.2b})$$

The temporal dynamics of these Fourier modes reads

$$\partial_t f_1^{(n)} = D_i \Delta f_1^{(n)} - n^2 D_\Delta f_1^{(n)} - \lambda f_1^{(n)} + (-1)^n \sigma f_2^{(n)} \quad (\text{B.3a})$$

$$\begin{aligned} \partial_t f_2^{(n)} = & D_p \Delta f_2^{(n)} - n^2 D_\varphi f_2^{(n)} - \frac{v_0}{2} [\tilde{\nabla} f_2^{(n-1)} + \tilde{\nabla}^* f_2^{(n+1)}] \\ & - (\lambda + \sigma) f_2^{(n)} + \lambda g_n [f_1^{(n)} + (-1)^n f_2^{(n)}] \end{aligned} \quad (\text{B.3b})$$

where we abbreviated the Wirtinger derivative $\tilde{\nabla} = \partial_x + i\partial_y$ and the Fourier modes

$$g_m = \int_{-\pi}^{\pi} d\eta e^{im\eta} g(\eta) = \int_{-\pi}^{\pi} d\eta \cos(m\eta) g(\eta) \quad (\text{B.4})$$

of the probability density function $g(\eta)$ for the repolarization angle η , cf. Fig. 7.1.

In Fourier domain, the Master equations are thus transformed into an infinite hierarchy of coupled partial differential equations. The advantage of this representation is twofold: Fourier modes possess a direct physical interpretation, e.g. the densities $\rho_s(\vec{r}, t) = f_s^{(0)}(\vec{r}, t)$ determine the local number of cell-cargo trucks in a certain motility state s and the fields $m_s(\vec{r}, t) = f_s^{(1)}(\vec{r}, t)$ quantify the local mass transport. Moreover, fast variables can be adiabatically eliminated, thereby allowing for a systematic reduction onto the slow modes. In this particular case, there is only one slow mode, namely the total particle density $\rho = \rho_1 + \rho_2$ which is a conserved quantity. Pathological cases may occur in singular limits, i.e. if certain model parameters become nonzero. As long as all parameter values are nonzero, the particle density is the only slow mode. Below, we aim at reducing the hierarchy [Eq. (B.3)] to the density only. At first, we consider the dynamics of the densities ρ_s :

$$\partial_t \rho_1 = D_i \Delta \rho_1 - \lambda \rho_1 + \sigma \rho_2, \quad (\text{B.5a})$$

$$\begin{aligned} \partial_t \rho_2 &= D_p \Delta \rho_2 - v_{\text{run}} \Re \left[\tilde{\nabla}^* m_2 \right] - (\lambda + \sigma) \rho_2 + \lambda (\rho_1 + \rho_2) \\ &= D_p \Delta \rho_2 - v_{\text{run}} \Re \left[\tilde{\nabla}^* m_2 \right] - \sigma \rho_2 + \lambda \rho_1. \end{aligned} \quad (\text{B.5b})$$

The sum of these equations yields the dynamics

$$\partial_t \rho = D_i \Delta \rho_1 + D_p \Delta \rho_2 - v_{\text{run}} \Re \left[\tilde{\nabla}^* m_2 \right] \quad (\text{B.6})$$

for the total particle density $\rho = \rho_1 + \rho_2$; the absence of local terms in this equation underlines that the density is indeed a slow mode.

The dynamics of the density is not closed but one has to find constitutive equations for ρ_1 , ρ_2 and m_2 as a function of the particle density. As we want to address the density dynamics on large spatial scales in the long-time limit, it is sufficient to take only the leading orders of spatial gradients into account. Formally, we apply the scaling ansatz

$$\rho \propto 1, \quad \tilde{\nabla} \propto \varepsilon, \quad \partial_t \propto \varepsilon^2, \quad f_i^{(n)} \propto \varepsilon^{|n|} \quad (\text{B.7})$$

keeping all terms up to quadratic order which is the lowest nontrivial order. Notably, this ansatz reflects diffusive scaling of length and time. Using this scaling ansatz, the stationary solution of Eqs. (B.5) yields

$$\rho_1 \simeq \frac{\sigma}{\lambda + \sigma} \cdot \rho, \quad (\text{B.8})$$

$$\rho_2 \simeq \frac{\lambda}{\lambda + \sigma} \cdot \rho \quad (\text{B.9})$$

to first order. These constitutive relations for ρ_i have a direct physical interpretation: the fraction of particles in state one or two is proportional to the relative fraction

of time spent in those states. Accordingly, we obtain the intermediate result for the density dynamics

$$\partial_t \rho \simeq \left[\frac{\sigma}{\lambda + \sigma} D_i + \frac{\lambda}{\lambda + \sigma} D_p \right] \Delta \rho - v_{\text{run}} \Re \left[\nabla \tilde{m}_2^{(*)} \right], \quad (\text{B.10})$$

with a weighted diffusion coefficient and a second term stemming from active particle transport in the polarized state.

Following the same strategy, we eventually find a closure relation for m_2 starting from the dynamics of the Fourier modes with $n = 1$

$$\partial_t m_1 \simeq -D_\Delta m_1 - \lambda m_1 - \sigma m_2, \quad (\text{B.11a})$$

$$\partial_t m_2 \simeq -D_\varphi m_2 - \frac{v_{\text{run}}}{2} \nabla \tilde{\rho}_2 - (\lambda + \sigma) m_2 + \lambda g_1 (m_1 - m_2) \quad (\text{B.11b})$$

which reads in matrix form as follows:

$$\partial_t \begin{pmatrix} m_1 \\ m_2 \end{pmatrix} = -\frac{v_{\text{run}}}{2} \begin{pmatrix} 0 \\ \nabla \tilde{\rho}_2 \end{pmatrix} - \begin{pmatrix} D_\Delta + \lambda & \sigma \\ -\lambda g_1 & D_\varphi + \lambda + \sigma + \lambda g_1 \end{pmatrix} \cdot \begin{pmatrix} m_1 \\ m_2 \end{pmatrix}. \quad (\text{B.12})$$

Using the scaling ansatz [Eq. (B.7)], the dynamics of the fields m_s decouples from higher order Fourier modes. Moreover, one can directly verify that both fields are fast variables therefore justifying the adiabatic elimination $\partial_t m_s \approx 0$. Solving for m_s , we eventually obtain

$$\begin{pmatrix} m_1 \\ m_2 \end{pmatrix} \simeq -\frac{v_{\text{run}}}{2} \begin{pmatrix} \nabla \tilde{\rho}_2 \end{pmatrix} \frac{1}{(D_\Delta + \lambda) \cdot (D_\varphi + \lambda + \sigma + \lambda g_1) + \sigma \lambda g_1} \cdot \begin{pmatrix} D_\varphi + \lambda + \sigma + \lambda g_1 & -\sigma \\ \lambda g_1 & D_\Delta + \lambda \end{pmatrix} \cdot \begin{pmatrix} 0 \\ 1 \end{pmatrix} \quad (\text{B.13})$$

and in particular the closure

$$m_2 \simeq -\frac{v_{\text{run}}}{2} \begin{pmatrix} \nabla \tilde{\rho}_2 \end{pmatrix} \frac{D_\Delta + \lambda}{(D_\Delta + \lambda) \cdot (D_\varphi + \lambda + \sigma + \lambda g_1) + \sigma \lambda g_1}. \quad (\text{B.14})$$

Inserting into Eq. (B.10) yields finally a diffusion equation to lowest order,

$$\partial_t \rho \simeq \mathcal{D} \Delta \rho, \quad (\text{B.15})$$

with the effective diffusion coefficient

$$\mathcal{D} = \left[\frac{\sigma}{\lambda + \sigma} D_i + \frac{\lambda}{\lambda + \sigma} D_p \right] + \frac{v_{\text{run}}^2}{2} \cdot \frac{\lambda}{\lambda + \sigma} \cdot \frac{D_\Delta + \lambda}{(D_\Delta + \lambda) \cdot (D_\varphi + \lambda + \sigma + \lambda g_1) + \sigma \lambda g_1}. \quad (\text{B.16})$$

The first term in brackets,

$$\mathcal{D}_w = \frac{\sigma}{\lambda + \sigma} D_i + \frac{\lambda}{\lambda + \sigma} D_p, \quad (\text{B.17})$$

is nothing but a weighted average of the diffusion coefficients in the isotropic and polarized state. The second term is an active contribution,

$$\mathcal{D}_a = \frac{v_{\text{run}}^2}{2} \cdot \frac{\lambda}{\lambda + \sigma} \cdot \frac{D_\Delta + \lambda}{(D_\Delta + \lambda) \cdot (D_\varphi + \lambda + \sigma + \lambda g_1) + \sigma \lambda g_1}, \quad (\text{B.18})$$

due to the persistent motion of the cell in the polarized state. Accordingly, it is proportional to the probability $\lambda/(\lambda + \sigma)$ to find a cell-cargo truck in the polarized state. Notably, \mathcal{D}_a depends in a non-monotonic way on the transition rate λ : it is directly proportional to λ for small values of λ whereas it decays with λ^{-1} in the limit $\lambda \rightarrow \infty$. Therefore, there is a finite repolarization rate λ which maximizes the diffusion of the cell-cargo truck.

At optimal parameter values, the trajectory of the cell-cargo truck consists of straight runs in the polarized state and reorientation phases while the cell is in the isotropic state, reminiscent of a run-and-tumble motility pattern emerging spontaneously from the cell-cargo interactions.

HEURISTIC THREE-STATE APPROACH

The calculation presented above is based on the assumption that reorientation events, i.e. phases during which the cell polarizes and moves underneath the particle, are faster compared to other relevant timescales and are therefore negligible. During these transition events, the center of mass of the cell-particle truck is approximately not displaced, only the relative positions of particle and cell are interchanged. Since these events are not contained in such simplified derivation, the corresponding calculation overestimates the diffusion coefficient. Below, it is presented a heuristic correction, based on the idea that a run of the cell can be subdivided into two phases: first, the polarized cell crawls underneath the particle to the other side (transition phase) and, second, it moves persistently with the particle on its back (persistent run phase), cf. Fig. 7.1. We furthermore consider the reorientation phase as an independent behavioral state during which no active transport occurs as argued above but cell and cargo change their relative positions. Accordingly, the rate σ must only account for the actual time τ_{run} spent in the persistent run phase of the truck: $\sigma = (\tau_{\text{run}} + \tau_{\text{rev}})^{-1} \rightarrow \tilde{\sigma} = \tau_{\text{run}}^{-1}$. The Master equation describing the dynamics of this three-state model is given by

$$\partial_t P_1(\vec{r}, \theta, t) = D_i \Delta P_1 + D_\Delta \partial_\theta^2 P_1 - \lambda P_1 + \tilde{\sigma} P_2(\vec{r}, \theta - \pi, t), \quad (\text{B.19a})$$

$$\partial_t P_{\text{rev}}(\vec{r}, \varphi, \theta, t) = D_{\text{rev}} \Delta P_{\text{rev}} + \lambda g(\varphi - \theta) \left[P_1(\vec{r}, \theta, t) + P_2(\vec{r}, \theta - \pi, t) \right] - \alpha P_{\text{rev}} \quad (\text{B.19b})$$

$$\begin{aligned} \partial_t P_2(\vec{r}, \varphi, t) = & D_p \Delta P_2 + D_\varphi \partial_\varphi^2 P_2 - v_{\text{run}} \vec{p}[\varphi] \cdot \nabla P_2 - (\lambda + \tilde{\sigma}) P_2 \\ & + \alpha \int_{-\pi}^{\pi} d\theta P_{\text{rev}}(\vec{r}, \varphi, \theta, t), \end{aligned} \quad (\text{B.19c})$$

where the index “rev” denotes the reorientation phase with the mean lifetime α^{-1} .

The long-time dynamics of the particle density $\rho(\vec{r}, t)$ of this refined model is still diffusive. The reduction of the Master equations (B.19) onto the diffusion equation follows the same logic as explained for the two-state case in the previous derivation. For the three state model, the density dynamics reads

$$\partial_t \rho_1 = D_i \Delta \rho_1 - \lambda \rho_1 + \tilde{\sigma} \rho_2, \quad (\text{B.20a})$$

$$\partial_t \rho_{\text{rev}} = D_{\text{rev}} \Delta \rho_{\text{rev}} - \alpha \rho_{\text{rev}} + \lambda(\rho_1 + \rho_2), \quad (\text{B.20b})$$

$$\partial_t \rho_2 = D_p \Delta \rho_2 - v_{\text{run}} \mathfrak{R} \left[\nabla^* m_2 \right] - (\lambda + \tilde{\sigma}) \rho_2 + \alpha \rho_{\text{rev}}. \quad (\text{B.20c})$$

yielding the intermediate density dynamics

$$\partial_t \rho = D_i \Delta \rho_1 + D_{\text{rev}} \Delta \rho_{\text{rev}} + D_p \Delta \rho_2 - v_{\text{run}} \mathfrak{A} \left[\tilde{\nabla}^* m_2 \right]. \quad (\text{B.21})$$

To lowest order in spatial gradients, we obtain the following stationary solution of Eqs. (B.20) as constitutive equations for the density dynamics:

$$\rho_1 \simeq \frac{\tilde{\sigma}}{\tilde{\sigma} + \lambda} \cdot \frac{\alpha}{\alpha + \lambda} \rho, \quad \rho_{\text{rev}} \simeq \frac{\lambda}{\alpha + \lambda} \rho, \quad \rho_2 \simeq \frac{\lambda}{\lambda + \tilde{\sigma}} \cdot \frac{\alpha}{\alpha + \lambda} \rho. \quad (\text{B.22})$$

In a second step, a closure relation for the field m_2 is found as outlined in the previous derivation. Interestingly, the calculation leads to the identical result,

$$m_2 \simeq -\frac{v_{\text{run}}}{2} \left(\tilde{\nabla} \rho_2 \right) \frac{D_{\Delta} + \lambda}{(D_{\Delta} + \lambda) \cdot (D_{\varphi} + \lambda + \tilde{\sigma} + \lambda g_1) + \tilde{\sigma} \lambda g_1}, \quad (\text{B.23})$$

cf. Eq. (B.14), however, the expression for ρ_2 has changed. Inserting the constitutive relations into Eq. (B.21) yields a diffusion equation with the diffusion coefficient $\mathcal{D} = \mathcal{D}_w + \mathcal{D}_a$ with the weighted sum

$$\mathcal{D}_w = \frac{\tilde{\sigma}}{\tilde{\sigma} + \lambda} \cdot \frac{\alpha}{\alpha + \lambda} D_i + \frac{\lambda}{\alpha + \lambda} D_{\text{rev}} + \frac{\lambda}{\lambda + \tilde{\sigma}} \cdot \frac{\alpha}{\alpha + \lambda} D_p \quad (\text{B.24})$$

of the diffusion coefficients in the individual motility states and the active contribution

$$\mathcal{D}_a = \frac{v_{\text{run}}^2}{2} \cdot \frac{\lambda}{\lambda + \tilde{\sigma}} \cdot \frac{\alpha}{\alpha + \lambda} \cdot \frac{D_{\Delta} + \lambda}{(D_{\Delta} + \lambda) \cdot (D_{\varphi} + \lambda + \tilde{\sigma} + \lambda g_1) + \tilde{\sigma} \lambda g_1} \quad (\text{B.25})$$

In the limit $\alpha \rightarrow \infty$, this expression reduces to the result of the previous derivation based on the two-state simplified model. The only difference is the correction factor $\alpha/(\alpha + \lambda)$ which is equal to the probability not to be in the reorientation state, i.e. the probability to be either in the isotropic or the polarized state.

Ultimately, if $D_i = D_{\text{rev}} = D_p = D$ as defined for the full-scale model of Chapter 7, one obtains:

$$\mathcal{D} = D + \frac{v_{\text{run}}^2}{2} \frac{\lambda}{\lambda + \tilde{\sigma}} \frac{\alpha}{\alpha + \lambda} \cdot \frac{D_{\Delta} + \lambda}{(D_{\Delta} + \lambda) \cdot (D_{\varphi} + \lambda + \tilde{\sigma} + \lambda g_1) + \tilde{\sigma} \lambda g_1}$$

It should be mentioned that, in order to apply this solution to the coarse-grained model discussed in Chapter 6, one must change the description of reorientations from $\varphi(t) \rightarrow \theta(t) + \eta$ to $\phi(t) \rightarrow \phi(t) + \delta\phi$, which translates into $D_{\Delta} = 0$ and $\eta \sim \pi - \delta\phi \implies g_1 = -\langle \cos \delta\phi \rangle$. Hence, by setting $D = D_{\text{int}}$ and $D_{\varphi} = 0$, one gets:

$$\mathcal{D} = D_{\text{int}} + \frac{v_{\text{run}}^2}{2} \frac{\lambda}{(\lambda + \tilde{\sigma})^2} \frac{\alpha}{\alpha + \lambda} \cdot \frac{1}{1 - \langle \cos \delta\phi \rangle}$$

BIBLIOGRAPHY

- [1] Loai KEA Abdelmohsen, Fei Peng, Yingfeng Tu, and Daniela A Wilson. "Micro- and nano-motors for biomedical applications." In: *Journal of Materials Chemistry B* 2.17 (2014), pp. 2395–2408.
- [2] Michael Abercrombie. "The Croonian Lecture, 1978-The crawling movement of metazoan cells." In: *Proceedings of the Royal Society of London. Series B. Biological Sciences* 207.1167 (1980), pp. 129–147.
- [3] Yunus Alapan, Oncay Yasa, Berk Yigit, I Ceren Yasa, Pelin Erkoç, and Metin Sitti. "Microrobotics and microorganisms: Biohybrid autonomous cellular robots." In: *Annual Review of Control, Robotics, and Autonomous Systems* 2 (2019), pp. 205–230.
- [4] Bruce Alberts. *Molecular biology of the cell*. Garland Science, Taylor and Francis Group, 2018.
- [5] Sergio Alonso, Maïke Stange, and Carsten Beta. "Modeling random crawling, membrane deformation and intracellular polarity of motile amoeboid cells." In: *PloS one* 13.8 (2018), e0201977.
- [6] Begoña Álvarez-González, Ruedi Meili, Effie Bastounis, Richard A Firtel, Juan C Lasheras, and Juan C del Álamo. "Three-dimensional balance of cortical tension and axial contractility enables fast amoeboid migration." In: *Biophysical journal* 108.4 (2015), pp. 821–832.
- [7] Aniruddha C Amrite and Uday B Kompella. "Size-dependent disposition of nanoparticles and microparticles following subconjunctival administration." In: *Journal of pharmacy and pharmacology* 57.12 (2005), pp. 1555–1563.
- [8] Gabriel Amselem, Matthias Theves, Albert Bae, Eberhard Bodenschatz, and Carsten Beta. "A stochastic description of Dictyostelium chemotaxis." In: *PloS one* 7.5 (2012).
- [9] Revathi Ananthakrishnan and Allen Ehrlicher. "The forces behind cell movement." In: *Int J Biol Sci* 3.5 (2007), pp. 303–317.
- [10] Natalie Andrew and Robert H Insall. "Chemotaxis in shallow gradients is mediated independently of PtdIns 3-kinase by biased choices between random protrusions." In: *Nature cell biology* 9.2 (2007), pp. 193–200.
- [11] Aaron C Anselmo, Jonathan B Gilbert, Sunny Kumar, Vivek Gupta, Robert E Cohen, Michael F Rubner, and Samir Mitragotri. "Monocyte-mediated delivery of polymeric backpacks to inflamed tissues: a generalized strategy to deliver drugs to treat inflammation." In: *Journal of Controlled Release* 199 (2015), pp. 29–36.
- [12] Igor S Aranson. *Physical Models of Cell Motility*. Springer, 2016.
- [13] Yulia Artemenko, Thomas J Lampert, and Peter N Devreotes. "Moving towards a paradigm: common mechanisms of chemotactic signaling in Dictyostelium and mammalian leukocytes." In: *Cellular and molecular life sciences* 71.19 (2014), pp. 3711–3747.

- [14] JM Ashworth and DJ Watts. "Metabolism of the cellular slime mould *Dictyostelium discoideum* grown in axenic culture." In: *Biochemical Journal* 119.2 (1970), pp. 175–182.
- [15] You Han Bae and Kinam Park. "Targeted drug delivery to tumors: myths, reality and possibility." In: *Journal of controlled release* 153.3 (2011), p. 198.
- [16] Dennis A Bazylynski and Richard B Frankel. "Magnetosome formation in prokaryotes." In: *Nature Reviews Microbiology* 2.3 (2004), pp. 217–230.
- [17] Jerome Berclaz, Francois Fleuret, Engin Turetken, and Pascal Fua. "Multiple object tracking using k-shortest paths optimization." In: *IEEE transactions on pattern analysis and machine intelligence* 33.9 (2011), pp. 1806–1819.
- [18] Alexander D Bershadsky and Michael M Kozlov. "Crawling cell locomotion revisited." In: *Proceedings of the National Academy of Sciences* 108.51 (2011), pp. 20275–20276.
- [19] Mayank D Bhavsar and Mansoor M Amiji. "Polymeric nano-and microparticle technologies for oral gene delivery." In: *Expert opinion on drug delivery* 4.3 (2007), pp. 197–213.
- [20] Christoph Blum. "Curvotaxis and pattern formation in the actin cortex of motile cells." PhD thesis. Georg-August Universität Göttingen, 2015.
- [21] Leo Boneschansker, Jun Yan, Elisabeth Wong, David M Briscoe, and Daniel Irimia. "Microfluidic platform for the quantitative analysis of leukocyte migration signatures." In: *Nature communications* 5.1 (2014), pp. 1–12.
- [22] Leonard Bosgraaf and Peter JM Van Haastert. "The ordered extension of pseudopodia by amoeboid cells in the absence of external cues." In: *PloS one* 4.4 (2009), e5253.
- [23] Till Bretschneider, Stefan Diez, Kurt Anderson, John Heuser, Margaret Clarke, Annette Müller-Taubenberger, Jana Köhler, and Günther Gerisch. "Dynamic actin patterns and Arp2/3 assembly at the substrate-attached surface of motile cells." In: *Current Biology* 14.1 (2004), pp. 1–10.
- [24] MARTIN L Brown and K ROBIN Yabroff. "12, Economic impact of cancer in the United States." In: *Cancer epidemiology and prevention* 202 (2006).
- [25] Michael George Bulmer. *Principles of statistics*. Dover Publications, 1979.
- [26] Eric J Campbell and Prosenjit Bagchi. "A computational model of amoeboid cell motility in the presence of obstacles." In: *Soft matter* 14.28 (2018), pp. 5741–5763.
- [27] Rika Wright Carlsen, Matthew R Edwards, Jiang Zhuang, Cecile Pacoret, and Metin Sitti. "Magnetic steering control of multi-cellular bio-hybrid microswimmers." In: *Lab on a Chip* 14.19 (2014), pp. 3850–3859.
- [28] Rika Wright Carlsen and Metin Sitti. "Bio-hybrid cell-based actuators for microsystems." In: *Small* 10.19 (2014), pp. 3831–3851.
- [29] Carlos Carmona-Fontaine, Helen K Matthews, Sei Kuriyama, Mauricio Moreno, Graham A Dunn, Maddy Parsons, Claudio D Stern, and Roberto Mayor. "Contact inhibition of locomotion in vivo controls neural crest directional migration." In: *Nature* 456.7224 (2008), pp. 957–961.

- [30] Hakan Ceylan, Immihan Ceren Yasa, Oncay Yasa, Ahmet Fatih Tabak, Joshua Giltinan, and Metin Sitti. "3D-printed biodegradable microswimmer for therapeutic cargo delivery and release." In: *ACS nano* 13.3 (2019), pp. 3353–3362.
- [31] Chuanrui Chen, Xiaocong Chang, Pavimol Angsantikul, Jinxing Li, Berta Esteban-Fernández de Ávila, Emil Karshalev, Wenjuan Liu, Fangzhi Mou, Sha He, Roxanne Castillo, et al. "Chemotactic guidance of synthetic organic/inorganic payloads functionalized sperm micromotors." In: *Advanced Biosystems* 2.1 (2018), p. 1700160.
- [32] Guanying Chen, Indrajit Roy, Chunhui Yang, and Paras N Prasad. "Nanotechnology and nanomedicine for nanoparticle-based diagnostics and therapy." In: *Chemical reviews* 116.5 (2016), pp. 2826–2885.
- [33] Andrey G Cherstvy, Oliver Nagel, Carsten Beta, and Ralf Metzler. "Non-Gaussianity, population heterogeneity, and transient superdiffusion in the spreading dynamics of amoeboid cells." In: *Physical Chemistry Chemical Physics* 20.35 (2018), pp. 23034–23054.
- [34] Mi-Ran Choi, Katie J Stanton-Maxey, Jennifer K Stanley, Carly S Levin, Rizia Bardhan, Demir Akin, Sunil Badve, Jennifer Sturgis, J Paul Robinson, Rashid Bashir, et al. "A cellular Trojan Horse for delivery of therapeutic nanoparticles into tumors." In: *Nano letters* 7.12 (2007), pp. 3759–3765.
- [35] Calina A Copos, Sam Walcott, Juan C del Álamo, Effie Bastounis, Alex Mogilner, and Robert D Guy. "Mechanosensitive adhesion explains stepping motility in amoeboid cells." In: *Biophysical Journal* 112.12 (2017), pp. 2672–2682.
- [36] Anna CH Coughlan and Michael A Bevan. "Effective colloidal interactions in rotating magnetic fields." In: *The Journal of chemical physics* 147.7 (2017), p. 074903.
- [37] Thomas M Cover and Joy A Thomas. *Elements of information theory*. John Wiley & Sons, 2012.
- [38] Jérémie Dalous, Emmanuel Burghardt, Annette Müller-Taubenberger, Franz Bruckert, Günther Gerisch, and Till Bretschneider. "Reversal of cell polarity and actin-myosin cytoskeleton reorganization under mechanical and chemical stimulation." In: *Biophysical journal* 94.3 (2008), pp. 1063–1074.
- [39] E Roy Davies. *Machine vision: theory, algorithms, practicalities*. Elsevier, 2004.
- [40] John R Davis, Andrei Luchici, Fuad Mosis, James Thackery, Jesus A Salazar, Yanlan Mao, Graham A Dunn, Timo Betz, Mark Miodownik, and Brian M Stramer. "Inter-cellular forces orchestrate contact inhibition of locomotion." In: *Cell* 161.2 (2015), pp. 361–373.
- [41] Peter N Devreotes and Sally H Zigmond. "Chemotaxis in eukaryotic cells: a focus on leukocytes and Dictyostelium." In: *Annual review of cell biology* 4.1 (1988), pp. 649–686.
- [42] Luc Devroye. "Nonuniform random variate generation." In: *Handbooks in operations research and management science* 13 (2006), pp. 83–121.

- [43] Nishit Doshi, Albert J Swiston, Jonathan B Gilbert, Maria L Alcaraz, Robert E Cohen, Michael F Rubner, and Samir Mitragotri. "Cell-based drug delivery devices using phagocytosis-resistant backpacks." In: *Advanced Materials* 23.12 (2011), H105–H109.
- [44] Andrew D Doyle, Francis W Wang, Kazue Matsumoto, and Kenneth M Yamada. "One-dimensional topography underlies three-dimensional fibrillar cell migration." In: *Journal of cell biology* 184.4 (2009), pp. 481–490.
- [45] David C Duffy, J Cooper McDonald, Olivier JA Schueller, and George M Whitesides. "Rapid prototyping of microfluidic systems in poly (dimethylsiloxane)." In: *Analytical chemistry* 70.23 (1998), pp. 4974–4984.
- [46] Richard Durrett. *Stochastic calculus: a practical introduction*. Vol. 6. CRC press, 1996.
- [47] JP Eckmann, S Oliffson Kamphorst, D Ruelle, et al. "Recurrence plots of dynamical systems." In: *World Scientific Series on Nonlinear Science Series A* 16 (1995), pp. 441–446.
- [48] Pelin Erkoc, Immihan C Yasa, Hakan Ceylan, Oncay Yasa, Yunus Alapan, and Metin Sitti. "Mobile microrobots for active therapeutic delivery." In: *Advanced Therapeutics* 2.1 (2019), p. 1800064.
- [49] Omid C Farokhzad and Robert Langer. "Impact of nanotechnology on drug delivery." In: *ACS nano* 3.1 (2009), pp. 16–20.
- [50] Ouajdi Felfoul, Mahmood Mohammadi, Samira Taherkhani, Dominic De Lanauze, Yong Zhong Xu, Dumitru Loghin, Sherief Essa, Sylwia Jancik, Daniel Houle, Michel Lafleur, et al. "Magneto-aerotactic bacteria deliver drug-containing nanoliposomes to tumour hypoxic regions." In: *Nature nanotechnology* 11.11 (2016), pp. 941–947.
- [51] Richard A Firtel and Chang Y Chung. "The molecular genetics of chemotaxis: sensing and responding to chemoattractant gradients." In: *Bioessays* 22.7 (2000), pp. 603–615.
- [52] Lies AL Fliervoet and Enrico Mastrobattista. "Drug delivery with living cells." In: *Advanced drug delivery reviews* 106 (2016), pp. 63–72.
- [53] Charles Fox. *An introduction to the calculus of variations*. Courier Corporation, 1987.
- [54] Peter Friedl, Stefan Borgmann, and Eva-B Bröcker. "Amoeboid leukocyte crawling through extracellular matrix: lessons from the Dictyostelium paradigm of cell movement." In: *Journal of leukocyte biology* 70.4 (2001), pp. 491–509.
- [55] Peter Friedl and Eva-B Bröcker. "TCR triggering on the move: diversity of T-cell interactions with antigen-presenting cells." In: *Immunological reviews* 186.1 (2002), pp. 83–89.
- [56] Peter Friedl and Bettina Weigelin. "Interstitial leukocyte migration and immune function." In: *Nature immunology* 9.9 (2008), p. 960.
- [57] Keinosuke Fukunaga. *Introduction to statistical pattern recognition*. Elsevier, 2013.
- [58] Paul A Gagniuc. *Markov chains: from theory to implementation and experimentation*. John Wiley & Sons, 2017.

- [59] Daniel T Gillespie. "A general method for numerically simulating the stochastic time evolution of coupled chemical reactions." In: *Journal of computational physics* 22.4 (1976), pp. 403–434.
- [60] Rafael C Gonzalez, Richard E Woods, and Steven L Eddins. "RUAN Qiuqi." In: *Digital Image Processing (Second edition)*, Beijing: Publishing House of Electronics Industry 8 (2007).
- [61] AN Gorban. "Detailed balance in micro-and macrokinetics and micro-distinguishability of macro-processes." In: *Results in Physics* 4 (2014), pp. 142–147.
- [62] Roman Gorelik and Alexis Gautreau. "Quantitative and unbiased analysis of directional persistence in cell migration." In: *Nature protocols* 9.8 (2014), p. 1931.
- [63] Bashar Hamza, Elisabeth Wong, Sachin Patel, Hansang Cho, Joseph Martel, and Daniel Irimia. "Retrotaxis of human neutrophils during mechanical confinement inside microfluidic channels." In: *Integrative Biology* 6.2 (2014), pp. 175–183.
- [64] Jiwon Han, Jin Zhen, Gwangjun Go, Youngjin Choi, Seong Young Ko, Jong-Oh Park, Sukho Park, et al. "Hybrid-actuating macrophage-based microrobots for active cancer therapy." In: *Scientific reports* 6 (2016), p. 28717.
- [65] Peter Haupt. *Continuum mechanics and theory of materials*. Springer Science & Business Media, 2013.
- [66] J Zachary Hilt and Nicholas A Peppas. "Microfabricated drug delivery devices." In: *International Journal of Pharmaceutics* 306.1-2 (2005), pp. 15–23.
- [67] Allan S Hoffman. "The origins and evolution of "controlled" drug delivery systems." In: *Journal of controlled release* 132.3 (2008), pp. 153–163.
- [68] Tim Hohmann and Faramarz Dehghani. "The cytoskeleton—a complex interacting meshwork." In: *Cells* 8.4 (2019), p. 362.
- [69] Zeinab Hosseinidou, Babak Mostaghaci, Oncay Yasa, Byung-Wook Park, Ajay Vikram Singh, and Metin Sitti. "Bioengineered and biohybrid bacteria-based systems for drug delivery." In: *Advanced drug delivery reviews* 106 (2016), pp. 27–44.
- [70] Shaobin Hou, Randy W Larsen, Dmitri Boudko, Charles W Riley, Ece Karatan, Mike Zimmer, George W Ordal, and Maqsudul Alam. "Myoglobin-like aerotaxis transducers in Archaea and Bacteria." In: *Nature* 403.6769 (2000), pp. 540–544.
- [71] Gilgueng Hwang, Rémy Braive, Laurent Couraud, Antonella Cavanna, Ouerghi Abdelkarim, Isabelle Robert-Philip, Alexios Beveratos, Isabelle Sagnes, Sinan Haliyo, and Stéphane Régnier. "Electro-osmotic propulsion of helical nanobelt swimmers." In: *The International Journal of Robotics Research* 30.7 (2011), pp. 806–819.
- [72] Khuloud Jaqaman, Dinah Loerke, Marcel Mettlen, Hirotaka Kuwata, Sergio Grinstein, Sandra L Schmid, and Gaudenz Danuser. "Robust single-particle tracking in live-cell time-lapse sequences." In: *Nature methods* 5.8 (2008), p. 695.
- [73] Wen-Xiong Kang, Qing-Qiang Yang, and Run-Peng Liang. "The comparative research on image segmentation algorithms." In: *2009 First International Workshop on Education Technology and Computer Science*. Vol. 2. IEEE. 2009, pp. 703–707.

- [74] Michael Kass, Andrew Witkin, and Demetri Terzopoulos. "Snakes: Active contour models." In: *International journal of computer vision* 1.4 (1988), pp. 321–331.
- [75] Irina Kaverina, Olga Krylyshkina, and J Victor Small. "Regulation of substrate adhesion dynamics during cell motility." In: *The international journal of biochemistry & cell biology* 34.7 (2002), pp. 746–761.
- [76] Michael J Kennedy. "Role of motility, chemotaxis, and adhesion in microbial ecology." In: *Annals of the New York Academy of Sciences* 506 (1987), p. 260.
- [77] Dmitri B Kirpotin, Daryl C Drummond, Yi Shao, M Refaat Shalaby, Keelung Hong, Ulrik B Nielsen, James D Marks, Christopher C Benz, and John W Park. "Antibody targeting of long-circulating lipidic nanoparticles does not increase tumor localization but does increase internalization in animal models." In: *Cancer research* 66.13 (2006), pp. 6732–6740.
- [78] Katarzyna Klimaszewska and Jan J Żebrowski. "Detection of the type of intermittency using characteristic patterns in recurrence plots." In: *Physical review E* 80.2 (2009), p. 026214.
- [79] Daniel Kohane, Daniel Anderson, Robert Langer, William Haining, and Lee Nadler. *pH-triggered microparticles*. US Patent App. 10/948,981. 2005.
- [80] Volodymyr B Koman, Pingwei Liu, Daichi Kozawa, Albert Tianxiang Liu, Anton L Cottrill, Youngwoo Son, Jose A Lebron, and Michael S Strano. "Colloidal nanoelectronic state machines based on 2D materials for aerosolizable electronics." In: *Nature nanotechnology* 13.9 (2018), pp. 819–827.
- [81] Katarzyna Krukiewicz and Jerzy K Zak. "Biomaterial-based regional chemotherapy: Local anticancer drug delivery to enhance chemotherapy and minimize its side-effects." In: *Materials Science and Engineering: C* 62 (2016), pp. 927–942.
- [82] Michael P Kummer, Jake J Abbott, Bradley E Kratochvil, Ruedi Borer, Ali Sengul, and Bradley J Nelson. "OctoMag: An electromagnetic system for 5-DOF wireless micromanipulation." In: *IEEE Transactions on Robotics* 26.6 (2010), pp. 1006–1017.
- [83] Pierre L'Ecuyer. "Uniform random number generation." In: *Annals of Operations Research* 53.1 (1994), pp. 77–120.
- [84] Lev Davidovich Landau and Evgenii Mikhailovich Lifshitz. *Course of theoretical physics*. Elsevier, 2013.
- [85] Robert Langer. "Drug delivery and targeting." In: *Nature* 392.6679 Suppl (1998), pp. 5–10.
- [86] Robert Langer and Nicholas A Peppas. "Advances in biomaterials, drug delivery, and bionanotechnology." In: *AIChE Journal* 49.12 (2003), pp. 2990–3006.
- [87] Chung-Nim Lee, Timothy Poston, and Azriel Rosenfeld. "Holes and genus of 2D and 3D digital images." In: *CVGIP: Graphical models and image processing* 55.1 (1993), pp. 20–47.
- [88] Sang Uk Lee, Seok Yoon Chung, and Rae Hong Park. "A comparative performance study of several global thresholding techniques for segmentation." In: *Computer Vision, Graphics, and Image Processing* 52.2 (1990), pp. 171–190.

- [89] Steffi Lehmann, Veronika Te Boekhorst, Julia Odenthal, Roberta Bianchi, Sjoerd van Helvert, Kristian Ikenberg, Olga Ilina, Szymon Stoma, Jael Xandry, Liying Jiang, et al. "Hypoxia induces a HIF-1-dependent transition from collective-to-amoeboid dissemination in epithelial cancer cells." In: *Current Biology* 27.3 (2017), pp. 392–400.
- [90] Liang Li, Edward C Cox, and Henrik Flyvbjerg. "'Dicty dynamics': Dictyostelium motility as persistent random motion." In: *Physical biology* 8.4 (2011), p. 046006.
- [91] B Lindner and EM Nicola. "Diffusion in different models of active Brownian motion." In: *The European Physical Journal Special Topics* 157.1 (2008), pp. 43–52.
- [92] William F Loomis, Danny Fuller, Edgar Gutierrez, Alex Groisman, and Wouter-Jan Rappel. "Innate non-specific cell substratum adhesion." In: *PloS one* 7.8 (2012), e42033.
- [93] Augustus Edward Hough Love. *A treatise on the mathematical theory of elasticity*. Cambridge university press, 2013.
- [94] Lynette M March and Clarissa JM Bachmeier. "10 Economics of osteoarthritis: a global perspective." In: *Bailliere's clinical rheumatology* 11.4 (1997), pp. 817–834.
- [95] Norbert Marwan, M Carmen Romano, Marco Thiel, and Jürgen Kurths. "Recurrence plots for the analysis of complex systems." In: *Physics reports* 438.5-6 (2007), pp. 237–329.
- [96] Edith Mathiowitz, Yong S Jong, Gerardo Carino, and Jules S Jacob. *Method for gene therapy using nucleic acid loaded polymeric microparticles*. US Patent 6,248,720. 2001.
- [97] D Meirow and D Nugent. "The effects of radiotherapy and chemotherapy on female reproduction." In: *Human reproduction update* 7.6 (2001), pp. 535–543.
- [98] Ralf Metzler, Jae-Hyung Jeon, Andrey G Cherstvy, and Eli Barkai. "Anomalous diffusion models and their properties: non-stationarity, non-ergodicity, and ageing at the centenary of single particle tracking." In: *Physical Chemistry Chemical Physics* 16.44 (2014), pp. 24128–24164.
- [99] Ralf Metzler and Joseph Klafter. "The random walk's guide to anomalous diffusion: a fractional dynamics approach." In: *Physics reports* 339.1 (2000), pp. 1–77.
- [100] Andrew S Mikhail and Christine Allen. "Block copolymer micelles for delivery of cancer therapy: transport at the whole body, tissue and cellular levels." In: *Journal of Controlled Release* 138.3 (2009), pp. 214–223.
- [101] Jean-Jacques Monsuez, Jean-Christophe Charniot, Noëlle Vignat, and Jean-Yves Artigou. "Cardiac side-effects of cancer chemotherapy." In: *International journal of cardiology* 144.1 (2010), pp. 3–15.
- [102] Eduardo Moreno, Sven Flemming, Francesc Font, Matthias Holschneider, Carsten Beta, and Sergio Alonso. "Modeling cell crawling strategies with a bistable model: From amoeboid to fan-shaped cell motion." In: *Physica D: Nonlinear Phenomena* (2020), p. 132591.
- [103] Philip M Morse and Herman Feshbach. "Methods of theoretical physics." In: *American Journal of Physics* 22.6 (1954), pp. 410–413.

- [104] Mark J. Mulligan et al. "Phase 1/2 Study to Describe the Safety and Immunogenicity of a COVID-19 RNA Vaccine Candidate (BNT162b1) in Adults 18 to 55 Years of Age: Interim Report." In: *medRxiv* (2020). DOI: [10.1101/2020.06.30.20142570](https://doi.org/10.1101/2020.06.30.20142570).
- [105] Craig Murdoch, Athina Giannoudis, and Claire E Lewis. "Mechanisms regulating the recruitment of macrophages into hypoxic areas of tumors and other ischemic tissues." In: *Blood* 104.8 (2004), pp. 2224–2234.
- [106] Douglas B Murphy. *Fundamentals of light microscopy and electronic imaging*. John Wiley & Sons, 2002.
- [107] Oliver Nagel. "Amoeboid Cells as a Transport System for Micro-Objects." PhD thesis. Universität Potsdam, 2019.
- [108] Oliver Nagel, Manuel Frey, Matthias Gerhardt, and Carsten Beta. "Harnessing Motile Amoeboid Cells as Trucks for Microtransport and-Assembly." In: *Advanced Science* 6.3 (2019), p. 1801242.
- [109] Oliver Nagel, Can Guven, Matthias Theves, Meghan Driscoll, Wolfgang Losert, and Carsten Beta. "Geometry-driven polarity in motile amoeboid cells." In: *PloS one* 9.12 (2014), e113382.
- [110] David D Nolte. "The tangled tale of phase space." In: *Physics today* 63.4 (2010), pp. 33–38.
- [111] Nobuyuki Otsu. "A threshold selection method from gray-level histograms." In: *IEEE transactions on systems, man, and cybernetics* 9.1 (1979), pp. 62–66.
- [112] Anthony Otto, Henry Collins-Hooper, Anand Patel, Philip R Dash, and Ketan Patel. "Adult skeletal muscle stem cell migration is mediated by a blebbing/amoeboid mechanism." In: *Rejuvenation research* 14.3 (2011), pp. 249–260.
- [113] Stefano Palagi and Peer Fischer. "Bioinspired microrobots." In: *Nature Reviews Materials* 3.6 (2018), p. 113.
- [114] Athanasios Papoulis and S Unnikrishna Pillai. *Probability, random variables, and stochastic processes*. Tata McGraw-Hill Education, 2002.
- [115] Norbert Pardi, Steven Tuyishime, Hiromi Muramatsu, Katalin Kariko, Barbara L Mui, Ying K Tam, Thomas D Madden, Michael J Hope, and Drew Weissman. "Expression kinetics of nucleoside-modified mRNA delivered in lipid nanoparticles to mice by various routes." In: *Journal of Controlled Release* 217 (2015), pp. 345–351.
- [116] Byung-Wook Park, Jiang Zhuang, Oncay Yasa, and Metin Sitti. "Multifunctional bacteria-driven microswimmers for targeted active drug delivery." In: *ACS nano* 11.9 (2017), pp. 8910–8923.
- [117] Chul Soon Park, Hyeonseok Yoon, and Oh Seok Kwon. "Graphene-based nanoelectronic biosensors." In: *Journal of Industrial and Engineering Chemistry* 38 (2016), pp. 13–22.
- [118] NA Peppas, P Bures, WS Leobandung, and H Ichikawa. "Hydrogels in pharmaceutical formulations." In: *European journal of pharmaceutics and biopharmaceutics* 50.1 (2000), pp. 27–46.

- [119] Ryan J Petrie, Andrew D Doyle, and Kenneth M Yamada. "Random versus directionally persistent cell migration." In: *Nature reviews Molecular cell biology* 10.8 (2009), pp. 538–549.
- [120] Kathrin E Peyer, Li Zhang, and Bradley J Nelson. "Bio-inspired magnetic swimming microrobots for biomedical applications." In: *Nanoscale* 5.4 (2013), pp. 1259–1272.
- [121] Roberto Piazza. *Statistical Physics: A Prelude and Fugue for Engineers*. Springer, 2016.
- [122] Laurent Pieuchot, Julie Marteau, Alain Guignandon, Thomas Dos Santos, Isabelle Brigaud, Pierre-François Chauvy, Thomas Cloatre, Arnaud Ponche, Tatiana Petithory, Pablo Rougerie, et al. "Curvotaxis directs cell migration through cell-scale curvature landscapes." In: *Nature communications* 9.1 (2018), pp. 1–13.
- [123] Kathleen F Pirollo and Esther H Chang. "Does a targeting ligand influence nanoparticle tumor localization or uptake?" In: *Trends in biotechnology* 26.10 (2008), pp. 552–558.
- [124] Thomas D Pollard and John A Cooper. "Actin, a central player in cell shape and movement." In: *Science* 326.5957 (2009), pp. 1208–1212.
- [125] Harrison V Prentice-Mott, Yasmine Meroz, Andreas Carlson, Michael A Levine, Michael W Davidson, Daniel Irimia, Guillaume T Charras, L Mahadevan, and Jagesh V Shah. "Directional memory arises from long-lived cytoskeletal asymmetries in polarized chemotactic cells." In: *Proceedings of the National Academy of Sciences* 113.5 (2016), pp. 1267–1272.
- [126] Jerry L Prince and Chenyang Xu. "A new external force model for snakes." In: *Proc. 1996 Image and Multidimensional Signal Processing Workshop*. Vol. 3. 31. 1996, p. 1.
- [127] Yong Qiu and Kinam Park. "Environment-sensitive hydrogels for drug delivery." In: *Advanced drug delivery reviews* 64 (2012), pp. 49–60.
- [128] Alfio Quarteroni, Riccardo Sacco, and Fausto Saleri. *Numerical mathematics*. Vol. 37. Springer Science & Business Media, 2010.
- [129] Wouter-Jan Rappel and Leah Edelstein-Keshet. "Mechanisms of cell polarization." In: *Current opinion in systems biology* 3 (2017), pp. 43–53.
- [130] Leonardo Ricotti, Barry Trimmer, Adam W Feinberg, Ritu Raman, Kevin K Parker, Rashid Bashir, Metin Sitti, Sylvain Martel, Paolo Dario, and Arianna Menciassi. "Biohybrid actuators for robotics: A review of devices actuated by living cells." In: *Science Robotics* 2.12 (2017).
- [131] Anne J Ridley, Martin A Schwartz, Keith Burridge, Richard A Firtel, Mark H Ginsberg, Gary Borisy, J Thomas Parsons, and Alan Rick Horwitz. "Cell migration: integrating signals from front to back." In: *Science* 302.5651 (2003), pp. 1704–1709.
- [132] Julia Riedl, Alvaro H Crevenna, Kai Kessenbrock, Jerry Haochen Yu, Dorothee Neukirchen, Michal Bista, Frank Bradke, Dieter Jenne, Tad A Holak, Zena Werb, et al. "Lifeact: a versatile marker to visualize F-actin." In: *Nature methods* 5.7 (2008), pp. 605–607.

- [133] Hannes Risken. *The Fokker-Planck Equation*. Springer, 1996.
- [134] P Romanczuk, M Bär, W Ebeling, B Lindner, and L Schimansky-Geier. "Active Brownian Particles-From Individual to Collective Stochastic Dynamics p." In: *The European Physical Journal Special Topics* 202 (2012).
- [135] Howard Rosen and Thierry Abrisat. "The rise and rise of drug delivery." In: *Nature Reviews Drug Discovery* 4.5 (2005), pp. 381–385.
- [136] Evanthia T Roussos, John S Condeelis, and Antonia Patsialou. "Chemotaxis in cancer." In: *Nature Reviews Cancer* 11.8 (2011), pp. 573–587.
- [137] Oliver Sangha and Gerold Stucki. "Economic impact of rheumatologic disorders." In: *Current opinion in rheumatology* 9.2 (1997), pp. 102–105.
- [138] Dirk Schmaljohann. "Thermo-and pH-responsive polymers in drug delivery." In: *Advanced drug delivery reviews* 58.15 (2006), pp. 1655–1670.
- [139] Ulrich S Schwarz and Samuel A Safran. "Physics of adherent cells." In: *Reviews of Modern Physics* 85.3 (2013), p. 1327.
- [140] Dávid Selmeczi, Liwen Li, Lykke II Pedersen, SF Nrelykke, Peter H Hagedorn, Stephan Mosler, Niels B Larsen, Edward C Cox, and Henrik Flyvbjerg. "Cell motility as random motion: A review." In: *The European Physical Journal Special Topics* 157.1 (2008), pp. 1–15.
- [141] Denis Semwogerere and Eric R Weeks. "Confocal microscopy." In: *Encyclopedia of biomaterials and biomedical engineering* 23 (2005), pp. 1–10.
- [142] Claude Elwood Shannon. "Communication in the presence of noise." In: *Proceedings of the IRE* 37.1 (1949), pp. 10–21.
- [143] Jingxin Shao, Mingjun Xuan, Hongyue Zhang, Xiankun Lin, Zhiguang Wu, and Qiang He. "Chemotaxis-guided hybrid neutrophil micromotors for targeted drug transport." In: *Angewandte Chemie* 129.42 (2017), pp. 13115–13119.
- [144] Peter Siegle, Igor Goychuk, and Peter Hänggi. "Origin of hyperdiffusion in generalized Brownian motion." In: *Physical review letters* 105.10 (2010), p. 100602.
- [145] Priyanka Singh, Santosh Pandit, VRSS Mokkapati, Abhroop Garg, Vaishnavi Ravikumar, and Ivan Mijakovic. "Gold nanoparticles in diagnostics and therapeutics for human cancer." In: *International journal of molecular sciences* 19.7 (2018), p. 1979.
- [146] Metin Sitti. "Voyage of the microrobots." In: *Nature* 458.7242 (2009), pp. 1121–1122.
- [147] Metin Sitti. *Mobile Microrobotics*. MIT Press, 2017.
- [148] Metin Sitti, Hakan Ceylan, Wenqi Hu, Joshua Giltinan, Mehmet Turan, Sehyuk Yim, and Eric Diller. "Biomedical applications of untethered mobile milli/microrobots." In: *Proceedings of the IEEE* 103.2 (2015), pp. 205–224.
- [149] Stanislaw Slomkowski and Teresa Basinska. "Polymer Nano-and Microparticle Based Systems for Medical Diagnostics." In: *Macromolecular symposia*. Vol. 295. 1. Wiley Online Library. 2010, pp. 13–22.
- [150] Pierre Soille. *Morphological image analysis: principles and applications*. Springer Science & Business Media, 2013.

- [151] Alexander A Solovev, Yongfeng Mei, Esteban Bermúdez Ureña, Gaoshan Huang, and Oliver G Schmidt. "Catalytic microtubular jet engines self-propelled by accumulated gas bubbles." In: *Small* 5.14 (2009), pp. 1688–1692.
- [152] Morgan M Stanton, Byung-Wook Park, Diana Vilela, Klaas Bente, Damien Faivre, Metin Sitti, and Samuel Sánchez. "Magnetotactic bacteria powered biohybrids target E. coli biofilms." In: *ACS nano* 11.10 (2017), pp. 9968–9978.
- [153] Steven H Strogatz. *Nonlinear dynamics and chaos with student solutions manual: With applications to physics, biology, chemistry, and engineering*. Westview Press, Boulder, 2015.
- [154] Xiaoqi Sun, Chao Wang, Min Gao, Aiyan Hu, and Zhuang Liu. "Remotely Controlled Red Blood Cell Carriers for Cancer Targeting and Near-Infrared Light-Triggered Drug Release in Combined Photothermal-Chemotherapy." In: *Advanced Functional Materials* 25.16 (2015), pp. 2386–2394.
- [155] Richard R Tamesis, Alejandro Rodriguez, William G Christen, Yonca A Akova, Elizabeth Messmer, and C Stephen Foster. "Systemic drug toxicity trends in immunosuppressive therapy of immune and inflammatory ocular disease." In: *Ophthalmology* 103.5 (1996), pp. 768–775.
- [156] Songsong Tang, Fangyu Zhang, Hua Gong, Fanan Wei, Jia Zhuang, Emil Karshalev, Berta Esteban-Fernández de Ávila, Chuying Huang, Zhidong Zhou, Zhengxing Li, et al. "Enzyme-powered Janus platelet cell robots for active and targeted drug delivery." In: *Science Robotics* 5.43 (2020).
- [157] Margaret A Titus and Holly V Goodson. "An evolutionary perspective on cell migration: Digging for the roots of amoeboid motility." In: *The Journal of Cell Biology* 216.6 (2017), p. 1509.
- [158] Gaurav Tiwari, Ruchi Tiwari, Birendra Sriwastawa, L Bhati, S Pandey, P Pandey, and Saurabh K Bannerjee. "Drug delivery systems: An updated review." In: *International journal of pharmaceutical investigation* 2.1 (2012), p. 2.
- [159] Stephanie Tran, Peter-Joseph DeGiovanni, Brandon Piel, and Prakash Rai. "Cancer nanomedicine: a review of recent success in drug delivery." In: *Clinical and translational medicine* 6.1 (2017), p. 44.
- [160] Roger Y Tsien and Alan Waggoner. "Fluorophores for confocal microscopy." In: *Handbook of biological confocal microscopy*. Springer, 1995, pp. 267–279.
- [161] Kazuhiko SK Uchida and Shigehiko Yumura. "Dynamics of novel feet of Dictyostelium cells during migration." In: *Journal of cell science* 117.8 (2004), pp. 1443–1455.
- [162] Miguel Vicente-Manzanares and Alan Rick Horwitz. "Cell migration: an overview." In: *Cell migration*. Springer, 2011, pp. 1–24.
- [163] Hua Wang. "Magnetic sensors for diagnostic medicine: CMOS-based magnetic particle detectors for medical diagnosis applications." In: *IEEE Microwave Magazine* 14.5 (2013), pp. 110–130.
- [164] Wei Wang, Wentao Duan, Suzanne Ahmed, Thomas E Mallouk, and Ayusman Sen. "Small power: Autonomous nano-and micromotors propelled by self-generated gradients." In: *Nano Today* 8.5 (2013), pp. 531–554.

- [165] Douglas B Weibel, Willow R DiLuzio, and George M Whitesides. "Microfabrication meets microbiology." In: *Nature Reviews Microbiology* 5.3 (2007), p. 209.
- [166] Douglas B Weibel, Piotr Garstecki, Declan Ryan, Willow R DiLuzio, Michael Mayer, Jennifer E Seto, and George M Whitesides. "Microoxen: Microorganisms to move microscale loads." In: *Proceedings of the National Academy of Sciences* 102.34 (2005), pp. 11963–11967.
- [167] Cornelis J Weijer. "Dictyostelium morphogenesis." In: *Current opinion in genetics & development* 14.4 (2004), pp. 392–398.
- [168] Katarina Wolf, Regina Müller, Stefan Borgmann, Eva Bröcker, Peter Friedl, et al. "Amoeboid shape change and contact guidance: T-lymphocyte crawling through fibrillar collagen is independent of matrix remodeling by MMPs and other proteases." In: *Blood* 102.9 (2003), pp. 3262–3269.
- [169] Worldometers. *World Population*. 2020. URL: <http://www.worldometers.info/world-population/>.
- [170] Chenyang Xu, Jerry L Prince, et al. "Snakes, shapes, and gradient vector flow." In: *IEEE Transactions on image processing* 7.3 (1998), pp. 359–369.
- [171] Haifeng Xu, Mariana Medina-Sánchez, Veronika Magdanz, Lukas Schwarz, Franziska Hebenstreit, and Oliver G Schmidt. "Sperm-hybrid micromotor for targeted drug delivery." In: *ACS nano* 12.1 (2018), pp. 327–337.
- [172] Jingwei Xue, Zekai Zhao, Lei Zhang, Lingjing Xue, Shiyang Shen, Yajing Wen, Zhuoyuan Wei, Lu Wang, Lingyi Kong, Hongbin Sun, et al. "Neutrophil-mediated anticancer drug delivery for suppression of postoperative malignant glioma recurrence." In: *Nature nanotechnology* 12.7 (2017), p. 692.
- [173] Immihan Ceren Yasa, Hakan Ceylan, Ugur Bozuyuk, Anna-Maria Wild, and Metin Sitti. "Elucidating the interaction dynamics between microswimmer body and immune system for medical microrobots." In: *Science Robotics* 5.43 (2020).
- [174] Simon Young, Mark Wong, Yasuhiko Tabata, and Antonios G Mikos. "Gelatin as a delivery vehicle for the controlled release of bioactive molecules." In: *Journal of controlled release* 109.1-3 (2005), pp. 256–274.
- [175] Walia Zahra, Sachchida Nand Rai, Hareram Birla, Saumitra Sen Singh, Hagera Dilnashin, Aaina Singh Rathore, and Surya Pratap Singh. "The global economic impact of neurodegenerative diseases: Opportunities and challenges." In: *Bioeconomy for Sustainable Development*. Springer, 2020, pp. 333–345.
- [176] Joseph Xu Zhou, MDS Aliyu, Erik Aurell, and Sui Huang. "Quasi-potential landscape in complex multi-stable systems." In: *Journal of the Royal Society Interface* 9.77 (2012), pp. 3539–3553.
- [177] Jiang Zhuang and Metin Sitti. "Chemotaxis of bio-hybrid multiple bacteria-driven microswimmers." In: *Scientific reports* 6 (2016), p. 32135.
- [178] Joseph d'Alessandro, Alexandre P Solon, Yoshinori Hayakawa, Christophe Anjard, François Detcheverry, Jean-Paul Rieu, and Charlotte Rivière. "Contact enhancement of locomotion in spreading cell colonies." In: *Nature Physics* 13.10 (2017), pp. 999–1005.

DECLARATION

I hereby declare that I have carried out this work and written this thesis by myself only with the help of the indicated means.

Potsdam, Germany, October 2016 - August 2020

Valentino Lepro